

DISSERTATION

Mechanical simulation of slit sensors of arachnids

ausgeführt zum Zwecke der Erlangung des akademischen Grades eines
Doktors der technischen Wissenschaften unter der Leitung von

ao.Univ.Prof. Dipl.-Ing. Dr.techn. Helmut J. Böhm, MSc.

E317

Institut für Leichtbau und Struktur-Biomechanik

TU-Wien

und

o.Univ.Prof. Dr.rer.nat. Friedrich G. Barth

Department für Neurobiologie und Kognitionsforschung

Universität-Wien

eingereicht an der Technischen Universität Wien

Fakultät für Maschinenwesen und Betriebswissenschaften

von

Dipl.-Ing. Bernhard Hößl

Matrikelnummer: 9526210

Blätterstraße 14/4/6

A-2721 Bad Fischau-Brunn

Wien, am 13.04.2007

Bernhard Hößl

Kurzfassung

Kern der hier vorliegenden Dissertation ist die Untersuchung des Deformationsverhaltens dehnungsempfindlicher Spaltsinnesorgane von Arachniden. Die einzelnen Spalte sind isoliert, in losen Gruppen oder in sogenannten lyraförmigen Organen angeordnet, wobei in letzteren die Spalte typischerweise sehr eng beieinander liegen. Das Ziel dieser Arbeit ist es, das komplexe Deformationsverhalten der einzelnen Spalte innerhalb lyraförmiger Organe zu verstehen, das durch die Interaktionseffekte zwischen den Spalten, wie Abschirmung und Verstärkung, bestimmt wird. Ausserdem werden die Einflüsse der Spaltmorphologie und der Form der Cuticula im Bereich der Einbettung der Organe auf die Spaltdeformationen untersucht. Zwei Modellierungsstrategien werden verfolgt, ein analytisches Verfahren aus dem Bereich der Bruchmechanik, die Methode von Kachanov, und die Methode der Finiten Elemente (FE). Die Ergebnisse der Simulationen sind Spaltdeformationen, die entweder an einer bestimmten Stelle oder entlang der Spaltufer ausgewertet werden, ebenso wie Spannungs- und Verzerrungsfelder im Nahfeld der Spalte.

Die Genauigkeit des analytischen Verfahrens von Kachanov wird mit Hilfe von Ergebnissen aus der FE Analyse untersucht. Die Grenzen der Einsetzbarkeit der analytischen Abschätzungen sind erreicht, wenn der Abstand zwischen den Spalten die halbe Spaltlänge unterschreitet, d.h. diese Methode ist zur Untersuchung von Einzelspalten oder losen Gruppen, aber nicht von lyraförmigen Organen, geeignet.

Zur Untersuchung von Spaltanordnungen, in denen die Spalte sehr eng beieinander liegen, wird im weiteren die FE Methode verwendet. Die FE Methode zeichnet sich dadurch aus, dass die Qualität der Ergebnisse nicht durch den kleinsten Abstand der Spalte limitiert wird, eine Vielzahl von unterschiedlichen Spaltgeometrien untersucht werden kann und eine einfache Erweiterung auf dreidimensionale Konfigurationen möglich ist. Im ersten

II

Schritt werden die charakteristischen geometrischen Parameter der Spalte, wie Streckung, Spaltform, Geometrie der Mittellinie der Spalte und Spaltorientierung, hinsichtlich deren Einfluss auf die Spaltdeformation untersucht. In Arachniden findet man unter anderem Spalte mit C- oder S-förmiger Mittellinie, jedoch sind die meisten Spalte gerade. Bei Insekten treten bevorzugt Öffnungen mit ellipsenähnlicher Form in den dehnungsempfindlichen Campaniformen Sensillen auf. Weiters wird die Richtungsempfindlichkeit generischer ebener Anordnungen von fünf gleichen Spalten, wie sie auch schon mit Hilfe der Methode nach Kachanov untersucht wurden, d.h. Stapel, versetzter Balken und Dreieck, analysiert, nun jedoch auf Basis von Spaltabständen wie sie auch bei lyraförmigen Organen auftreten.

Lyraförmige Organe sind hochentwickelte Spaltanordnungen mit Variationen hinsichtlich der Form der Spaltmittellinie, der Spaltbreite, der Orientierung und der Länge der einzelnen Spalte. Der Einfluss dieser Variationen auf die Richtungsempfindlichkeit der Anordnungsmuster wird mit ebenen Spaltformationen basierend auf realen lyraförmigen Organen der Spinnen *Cupiennius salei* und der Vogelspinne *Aphonopelma* untersucht. Für den speziellen Fall des lyraförmigen Organs HS8, das sich auf der Tibia von *C. salei* befindet, werden die mit einem ebenem FE-Modell bestimmten Spaltdeformationen mit Resultaten von Messungen mit Hilfe von Weißlichtinterferometrie Messungen bestimmt.

Schließlich erweitern wir die FE-Modelle in die dritte Dimension und verwenden Schalenmodelle, um die unterschiedlichen Formen der Cuticula an der Stelle der Organe, im speziellen globale und lokale Krümmungseffekte, zu untersuchen. Eine Reihe numerischer Simulationen verwenden ebene und zylindrische Bereiche, in denen Einzelspalte modelliert werden, die auf lokalen Erhebungen in der Form von Kuppen und Leisten liegen. Ausserdem werden dreidimensionale Strukturmodelle entwickelt und verwendet, um den Einfluss der Querschnitte und der Steifigkeit der Membranen sowie der Materialeigenschaften der Rezeptorlymphe innerhalb der Spalte auf die Spaltdeformation zu untersuchen.

Ein Kapitel der Dissertation ist schließlich der Frage gewidmet, wie entsprechende biomimetische Sensoren aufgebaut sein könnten.

Abstract

In the present thesis the intriguing mechanics of strain sensitive arachnid slit sensilla are studied. Individual slits occur singly, in loose groups, and in so called lyriform organs, where they are arranged in close neighborhood. The emphasis of this work is put on the complex deformation patterns of lyriform organs under mechanical far field loading, i.e., on the role of interaction effects, namely shielding and amplification, between the slits, and on the effects of details of the slits' morphology and the three dimensional shape of the cuticle at the site of the organs on the slits' deformation. Two modeling approaches are employed, an analytical method developed within the framework of fracture mechanics, Kachanov's method, and the Finite Element (FE) method. The results of these simulations are slit face displacements evaluated along the individual slits and at discrete points along the slits' faces as well as stress and strain fields in the vicinity of the slits.

The accuracy of Kachanov's analytical approximations for planar arrangements of slits is assessed by comparisons with results obtained by Finite Element analysis. The limits of the applicability of Kachanov's approximation to slit sensilla are found to be reached when the lateral spacing between interacting slits is less than half their length, i.e., the method is suitable for studying single slits and loose groups but not lyriform organs.

For studying more closely spaced slits the FE method is used. This method is not subject to intrinsic limitations in the closest neighboring distance between the slits, allows a wide variety of slit shapes to be studied, and can be easily extended to three dimensional configurations.

In a first step the influence of the geometrical parameters describing single isolated slits, such as aspect ratio, slit shape, geometry of the slits' centerlines, and slit orientation, on

IV

the slit deformation is analyzed. In arachnids slits can have a C- or S-shaped centerline but are usually straight. Insects show ellipse-like openings of low aspect ratio for their strain sensitive campaniform sensilla rather than slits with parallel faces and rounded ends. In a next step the directional response of generic planar arrangements of five slits similar to those studied with Kachanov's method, i.e. non-staggered, oblique bar, and triangular arrangements, is investigated for lateral distances as found in lyriform organs.

Lyriform organs are generally highly developed slit arrangements with variations in slit width, shape of the slits' centerline, orientation and length of the individual slits. The influence of these variations on the directional responses of the arrangements is investigated via planar slit formations based on actual lyriform organs of the spiders *Cupiennius salei* and the bird spider *Aphonopelma*. For the case of the organ HS8 located on the tibia of *C. salei* the accuracy of the predictions of the slit deformation of the planar FE model is assessed by comparison with measurements obtained by white light interferometry.

Finally we extend the FE models to the third dimension and use structural models to study the influence of the cross section and the stiffness of the membranes as well as the material parameters of the slits' filling on the slit deformation. In addition three dimensional shells explore different three dimensional shapes of the regions of cuticle in which the slits are situated, especially global and local curvature effects. Series of numerical experiments use flat and cylindrical regions some of which contain local features in the form of dimples and ridges onto which single slits and generic arrangements of slits were placed.

A section of this thesis is devoted on how slits might be arranged in bio-inspired micro strain sensors.

Acknowledgments

This work was carried out in the course of my stay at the Institute of Lightweight Design and Structural Biomechanics (ILSB) at Vienna University of Technology and the Department for Neurobiology and Cognition Research at Vienna University. The funding of the Austrian Science Found (FWF), grant 16348, is gratefully acknowledged. I am deeply indebted to my thesis advisor, Ao.Univ.Prof. Dr.techn. H.J. Böhm, head of the above Institute, for his intense assistance in preparing this work, his ideas and advice in many discussions. Especially, I want to express my sincere gratitude to my co-advisor and FWF project manager, o.Univ.Prof. Dr. F.G. Barth, for his invaluable assistance in preparing this work and his extensive support.

Many thanks go to o.Univ.Prof. Dr.techn. F.G. Rammerstorfer for having an eye on the current state of my research and his guidance. Additionally, I would like to express my special thanks to my colleagues and friends at the ILSB for their friendly and supportive working atmosphere. Special thanks go to Robert Bitsche, Sergio Nogales (muchos quesos), and Ivica Smojver for being such great room mates and to G. Schneider, the system administrator of the ILSB, for his support in many computer relevant difficulties and questions.

Last but not least I want to thank Ewald Gingl, Jorge Molina, Rainer Müllan, Clemens Schaber, as well as all members of the Department for Neurobiology and Cognition Research for many fruitful discussions, new ideas, and their patience in explaining biological details to me, an engineer who is still overwhelmed by the richness of details of the creatures living on mother earth.

Für meine Mutter
Frau Marianne Hößl

Contents

List of Symbols	XII
1 Introduction	1
2 Biological background	5
2.1 Slit sensilla	5
2.2 Cuticle - a natural composite shell	10
2.2.1 Microstructure of cuticle	12
2.2.2 Effective mechanical properties of cuticle	13
2.2.2.1 Constituent properties of cuticle	15
2.2.2.2 Effective Young's modulus of cuticle	16
2.2.2.3 Effective tensile strength and strain at failure of cuticle . .	17
2.2.2.4 Effective Poisson's ratio of cuticle	19
2.2.2.5 Micromechanical assessment of the stiffness of cuticle . . .	19
2.2.2.6 Material behavior of cuticle	22

3	Methods	24
3.1	Analytical approach	24
3.1.1	On the problem of crack interaction	24
3.1.2	Stress fields generated by cracks	25
3.1.3	Kachanov's method	27
3.1.4	Enhancements of Kachanov's method	31
3.1.4.1	Improving the evaluation of the interaction terms	31
3.1.4.2	Using more accurate approximations for the face deformations	31
3.2	Finite Element method	31
3.2.1	Planar FE models	32
3.2.1.1	Planar FE models for assessing Kachanov's method	34
3.2.1.2	Planar FE models for studying slit sensilla	37
3.2.2	3D FE models	41
3.2.2.1	3D FE structural models	41
3.2.2.2	3D FE shell models	47
4	Planar models	53
4.1	Results	53
4.1.1	Analytical models using Kachanov's method	53
4.1.1.1	Comparisons between analytical and FE models	53
4.1.1.2	Results of the analytical models	55

4.1.2	Planar FE models of generic slit arrays	58
4.1.2.1	Deformation of a single slit subjected to a normal uni-axial load	58
4.1.2.2	Deformation of arrays of five parallel slits under a uni-axial normal load	62
4.1.2.3	Dependence of the deformation of a single slit on the direc- tion of uni-axial loads	67
4.1.2.4	Dependence of the deformation of fan-type arrangements of five slits on the direction of uni-axial loads	68
4.1.2.5	Dependence of the deformation of arrays of five parallel slits on the direction of uni-axial loads	70
4.1.3	Planar FE models of slit arrays imitating lyriform organs	72
4.1.3.1	A special case: The measured and simulated deformation of organ HS8	72
4.1.3.2	Directional dependence of the deformation of natural slit patterns other than that of lyriform organ HS8	78
4.1.3.3	Interactions between a lyriform organ and a closely posi- tioned group of slits	86
4.2	Discussion	89
4.2.1	Analytical models using Kachanov's method	89
4.2.1.1	Lateral crack spacing	89
4.2.1.2	Oblique bar arrangements	89
4.2.1.3	Triangular and "bell shaped" arrangements	90
4.2.2	Planar FE models of generic slit arrays	92

4.2.2.1	Dendrite positions in arachnid lyriform organs	92
4.2.2.2	Single slits	93
4.2.2.3	Arrangements of five slits	94
4.2.3	Planar FE models of slit arrays imitating lyriform organs	96
4.2.3.1	Comparing models with properties of original lyriform organ HS8	96
4.2.3.2	Simple, generalized and more realistic slit patterns	97
4.2.3.3	Mechanical interaction between lyriform organs and nearby slit arrays	101
4.2.3.4	Dendrite positions	103
4.2.3.5	Stress concentrations associated with slit arrangements	103
4.2.4	On determining the direction of a uni-directional load	106
5	3D models	109
5.1	Results	109
5.1.1	Effect of shape of the membranes of a single slit without filling subjected to normal uni-axial loads	109
5.1.2	Fluid filled single slit subjected to normal uni-axial loads	112
5.1.3	Effect of membrane stiffness in a stack of five slits subjected to normal uni-axial loads	114
5.1.4	Embedding of slits in disks and cylinders three-dimensionally curved at the site of the slit	115
5.1.5	Slit interaction under bending loads	119

<i>CONTENTS</i>	XI
5.2 Discussion	120
5.2.1 Details of slits and stimulus transformation	120
5.2.2 Embedding of the organs and slit deformation	122
6 Designing strain sensors	124
7 Conclusions	128
A The stress field generated by a crack	131
B Example for adapting the normalized results	133
Bibliography	135

List of Symbols

Symbols – scalars

a_n, b_n, c_n	coefficients of the quadratic polynomial for estimating the crack face displacements D_n
a_τ, b_τ, c_τ	coefficients of the quadratic polynomial for estimating the crack face displacements D_τ
A_{ell}	area of ellipse
A_{slit}	area of slit (capped rectangle)
B	shape parameter in C- and S-shaped slits
D	crack/slit face displacement
$D_{\text{slit}}^*(x)$	calculated face displacement of a slit
$D_{\text{crack}}^*(\xi)$	calculated face displacement of a crack
D_c	face displacement at center of crack/slit
D_{cc}	face displacement at center of single isolated crack
$D_{\text{c,qp}}$	face displacement at center of crack in models incorporating quarter point elements at the crack tips
$D_{\text{c,ref}}$	face displacement at center of a slit in models incorporating quarter point elements at the crack tips
$D_{\text{c,ell}}$	slit face displacement of an elliptical slit
$D_{\text{c,FE}}$	face displacement at center of crack by using the FE method
$D_{\text{c,K}}$	face displacement at center of crack by using Kachanov's method
$D_{\text{c,slit}}$	slit face displacement at center of slit

D_d	slit face displacement at position of the dendrite in a slit
$D_l(x)$	slit face deformation along the slits in longitudinal direction (shear deformation)
D_n	crack face opening displacement for crack opening mode I
D_{sc}	face displacement at center of single isolated slit
D_τ	crack face opening displacement for crack opening mode II
E	Young's modulus
E_A	out-of-plane (axial) Young's modulus
E_c	Young's modulus of the cuticle
E_m	Young's modulus of the membranes covering the slits
E_r	reference in-plane Young's modulus
E_T	in-plane (transversal) Young's modulus
G_A	out-of-plane (axial) shear modulus
I_1 to I_6	coefficients for evaluating the stress field generated by a crack
K_I	stress intensity factor for crack opening mode I
K_{II}	stress intensity factor for crack opening mode II
l	length of crack/slit
ℓ_{edge}	element edge length in FE models
l_i	length of crack i
l_0	length of largest crack/slit in array
l_0/w_0	aspect ratio (length/width) of slit
l_p	projected length of C- and S-shaped slit
M_y	bending moment about the y -axis
N	number of cracks in array
$p_i(\xi_i)$, p	normal component of the traction vector
$\langle p \rangle$	average normal component of the traction vector at the crack faces
r	radius of a point close to a crack tip in cylindrical coordinates
R	radius of circular arrangement of inner tips of slits in fan-like arrays
S	lateral spacing between neighboring slits
t_r	thickness of the disk in the reference configuration

t	thickness of the disk
u_z	displacements in z -direction of points on the membranes
$u(\xi)$	displacement of one crack face
w_0	width of slit in the undeformed state
w	distance between two points in the deformed state
\tilde{w}	normal distance between two points in the deformed state
x, y	in-plane coordinate pair
z	out-of-plane direction
α	angle subtended by fan-like arrangements
ε_a	applied in-plane far-field strain
$\varepsilon_{a,r}$	reference applied in-plane far-field strain
δ	factor for evaluating the stress field generated by a crack
ΔA	difference between the area of slit and ellipse
ΔD_c	difference in slit face displacement between slit and elliptical opening
Δl	difference in length of neighboring slits
η	factor for evaluating the stress field generated by a crack
κ	factor for evaluating the stress field generated by a crack
Λ_{ji}^{mn}	interaction coefficient ($i, j = 1, 2, \dots, N; j \neq i; m, n = p, \tau$)
Λ	longitudinal shift between slits
ν	Poisson's ratio
ν_A	out-of-plane (axial) Poisson's ratio
ν_T	in-plane (transversal) Poisson's ratio
Φ	in-plane angle of unidirectional load (with respect to slit)
ϱ	factor for evaluating the stress field generated by a crack
σ_a	applied in-plane far-field stress
$\sigma_{a,r}$	reference applied in-plane far-field stress
$\sigma_{ji}^{mn}(\xi_i)$	component of the stress tensor ($i, j = 1, 2, \dots, N; j \neq i; m, n = p, \tau$)
$\tau_i(\xi_i), \tau$	shear component of the traction vector
$\langle \tau \rangle$	average shear traction at the crack faces

- ω inclination of the cracks
 ξ coordinate along the cracks

Symbols – vectors, matrices, tensors

- $\mathbf{H}(\omega_i)$ tensor for rotation of the coordinate system into alignment with the crack
 $\mathbf{t}_i(\xi_i)$ vector of tractions acting on the crack faces of crack i
 $\langle \mathbf{t}_i \rangle$ vector of average tractions acting on crack i
 \mathbf{T}^∞ vector of far field traction components
 \mathbf{t}_i^∞ vector of far field tractions in the coordinate system of the crack i
- $\mathbf{\Lambda}_{ji}$ matrix of the interaction coefficients
 $\boldsymbol{\sigma}_{ji}(\xi_i)$ stress tensor for the normalized stress field at the faces of crack i that is generated when crack j is subjected to a uniform unit traction
 $\Delta \mathbf{t}_{ji}(\xi_i)$ vector of tractions induced at crack i by the other j cracks loaded by $\mathbf{t}_i(\xi_i)$

Abbreviations

- C. salei* Central American hunting spider *Cupiennius salei* (Keyserling)
DOF degree of freedom
FE finite element
FEM finite element method
LEFM linear elastic fracture mechanics
HS3 lyriform organ number three on the back side (“**H**inter**S**eite”) of each leg of *C. salei*
SCF stress concentration factor
SEM Scanning electron microscope
SIF Stress intensity factor
TEM Transmission electron microscopy
VS5 lyriform organ number five on the front side (“**V**order**S**eite”) of each leg of *C. salei*

Chapter 1

Introduction

In arthropods the exoskeleton not only provides structural support to the animal's body and holds all vital organs. It also functions as the interface of the organism to the environment. In principle arthropods have two ways of receiving mechanical stimuli from their environment. The first is to use sensory hairs on the outside of the exoskeleton, such as trichobothria, which are extremely sensitive airflow sensors (Humphrey et al., 2003), and tactile hairs (Dechant et al., 2001). The second way is to employ sensors within the exoskeleton which provide information on the local strains, the main representatives being the campaniform sensilla of insects and the slit sensilla of arachnids. The latter represent a highly developed system of sensors for monitoring the effects of various mechanical loads that act on the exoskeleton, such as hemolymph pressure, vibrations of the substrate, and muscle activity; for reviews see Barth (2002a) and French et al. (2002).

Our study is based on the arachnid *Cupiennius salei* (Ctenidae; Lachmuth et al. (1985)) which is a large Central American nocturnal hunting spider (Fig. 1.1). This spider was chosen because it is rich in slit sense organs (15 so called lyriform organs on each of the eight walking legs), has large size (leg span about the size of a palm), and is easy to handle and breed under laboratory conditions.

Arthropod strain sensitive sensors have been studied by a number of authors. The majority of them concentrated on the ultra structure and intra- or extracellular measurements of the organs' response to loads, but only a few of them evaluated strains at the locations of



FIGURE 1.1: Adult female central American hunting spider *Cupiennius salei* in resting position.

the sensilla or their deformation under stimulus relevant loads. In such a work Cocatre-Zilgen and Delcomyn (1999) developed an analytical model for predicting the physiological response of campaniform sensilla on the tibia of the cockroach *Periplaneta americana* based on analytically calculated strains in a tube representing the tibia. Detailed planar FE models of the trochanter of *Periplaneta americana* were used by Flannigan (1998), Kaliyamoorthy et al. (2001), and Kaliyamoorthy et al. (2005). There the strains at the positions of some sensilla were evaluated for loads pertinent to walking and climbing. Skordos et al. (2002) studied aspects of the deformation behavior of campaniform sensilla of insects by the FE method. They used models in 2D and 3D employing circular openings representing the campaniform sensilla.

Aside from theoretical investigations measurements on composites with holes that approximate the fiber architecture of insect cuticle in the vicinity of pore canals were conducted by Chen et al. (2002) and Chen and Fan (2004). One attempt of fabricating biomimetic strain-sensing microstructures inspired by campaniform sensilla is found in literature. There Wicaksono et al. (2005) conducted optical measurements on the deformation of a Si membrane-in-recess structure.

To the knowledge of the authors no FE or analytical models of arachnid slit sensilla have been reported in the literature. The present study may be seen as the continuation of a line of work initiated by Barth and Wadeuhl (1975) and Barth et al. (1984) with photoelastic experimental investigations of polymer disks into which arrangements of slits were cut. A different type of experiments were carried out by Blickhan and Barth (1985) and Brüssel (1987), who used strain gauges for measuring strains in the exoskeleton of *C. salei* and the bird spider *Aphonopelma* at the positions of lyriform organs on the walking legs during walking and jumping.

Individual sensory slits in arachnids are narrow, with aspect ratios (slit length l /slit width w) of up to 100 (Barth, 1981). Their shape suggests that methods developed for evaluating crack opening distances in fracture mechanics may be used to analyze the displacements of the slits' faces under load. In part of the present study the analytical approximations developed by Kachanov and co-workers (Kachanov, 1994; Gorbatiikh and Kachanov, 2000) are applied, which provide solutions for the displacements of the faces of two or more interacting cracks. Kachanov's approach is assessed by comparing the results obtained for arrays of five non-staggered, equally spaced, parallel cracks of equal length to Finite Element (FE) solutions. It is found that the analytical model is limited to the description of arrangements of slits separated laterally by at least one half of their length (Höbl et al., 2005, 2006). Finite Element modeling, while posing higher computational requirements, is not subject to such limitations and, accordingly, suitable for studying the compressive slit face displacements (D) of closely spaced arrangements of slits which are typical of arachnid lyriform organs. In addition, FE analysis allows a wide variety of slit shapes to be considered. The present work utilizes this flexibility of the FE method for studying the directional response of single slits and planar arrangements of slits subjected to uniform far-field loads (Höbl et al., 2007a,b). Details of individual slits are investigated with structural models in 3D representing their morphology. To study the effect of various stiffening

elements on the slit face deformation of single slits and on the interaction effects in slit arrangements ridges and spherical caps (“dimples”) are employed in planar and cylindrical shells, where the latter may be viewed as highly idealized models of spider tibia (Höbl et al., 2007c).

Simultaneously, electrophysiological measurements at the organ HS10 (Gingl et al., 2006) located on the metatarsus and on organ HS8 on the tibia under stimulus relevant loads were performed within the same project as the present work. Stains were introduced into the somata by glass electrodes previously used for the measurements and the dendrites were traced back to the slits. Also within the same research project experimental studies of spider slit sensilla were carried out, in which the deformations of the slit faces were measured under stimulus relevant loads by using white light interferometry (Höbl et al., 2007b; Schaber and Barth, in prep.). In addition serial sectioning of some organs provided insight into the 3D morphology of the different slits in the organs (Müllan, 2005) (see Chapter 2.1).

Although the main focus of the present study is on biomechanical aspects and aims towards a deeper understanding of the intriguing mechanics of close parallel arrays of slit sensilla, it should be mentioned that quantitative predictions on the complex deformation patterns of such arrangements form a valuable basis for the design of “biologically inspired” or biomimetic strain sensors for engineering applications.

Chapter 2

Biological background

2.1 Slit sensilla

Slit sensilla occur in most orders of arachnids (Barth and Libera, 1970; Barth and Stagl, 1976; Barth and Wadeuhl, 1975). *Cupiennius salei* has some 3300 sensory slits in its exoskeleton (Barth and Libera, 1970). About 86 % of these slits are found on the extremities, i.e. the legs and pedipalps, where they are embedded in stiff, sclerotized exocuticle. The 96 slits found on the opisthosoma (excluding petiolus) are exceptional in being surrounded by soft cuticle.

Some examples of arachnid slit sensilla are shown in Fig. 2.1. Depending on the lateral spacing of the individual slits, S , slit sensilla can be subdivided into three types (Barth and Libera 1970): isolated slits (distance to the closest neighboring slit $S \gtrapprox 1.5l$), loose groups ($S \gtrapprox 0.25l$), and compound or lyriform organs (side-by-side arrangements of up to 30 closely spaced slits with nearest neighbor distances of $S \lesssim 10\mu\text{m}$).

Figure 2.2 presents SEM images of representatives of the three types of slit sensilla found in *C. salei*. Approximately half of the slits present in this spider are either single slits or belong to loose groups. The other half form a total of 144 lyriform organs, which are situated only on the appendages (134 on the legs and pedipalps, 10 on the spinnerets and chelicerae). Lyriform organs are typically found on the lateral aspects of the extremities,

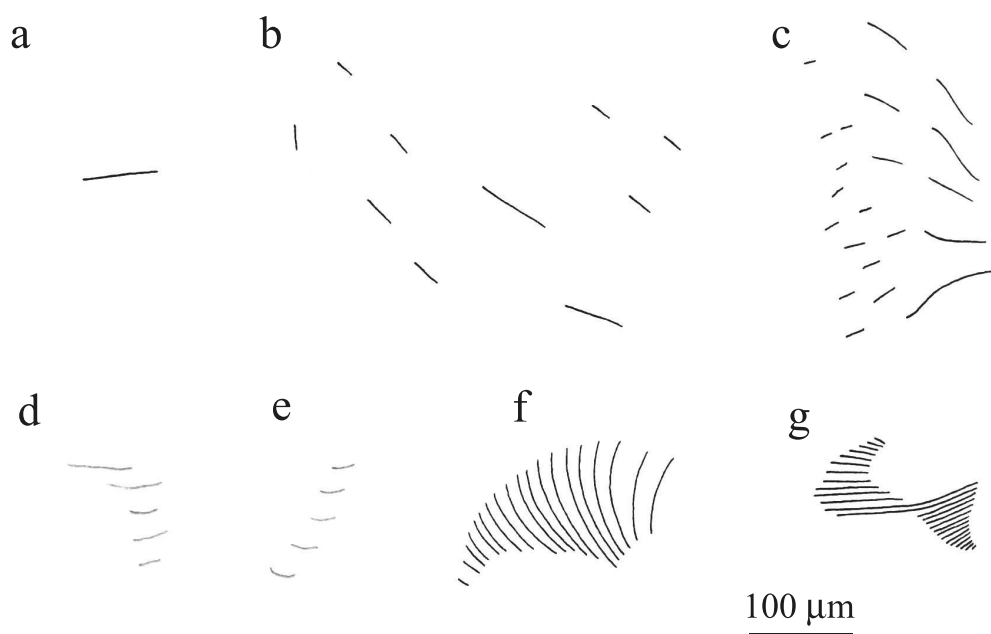


FIGURE 2.1: Different slit arrangements found in the spider *Cupiennius salei*, the scorpion *Androctonus australis*, the whip spider *Admetus pumilio*, and the harvestman *Amilenus aurantiacus*. **a** single slit, **b** group of single slits (scorpion trochanter), **c** group of single slits (whip spider trochanter), **d** group of single slits (harvestman coxa), **e** group of single slits (harvestman femur), **f** lyriform organ (whip spider trochanter), and **g** lyriform organ (spider trochanter). From Barth and Stagl (1976).

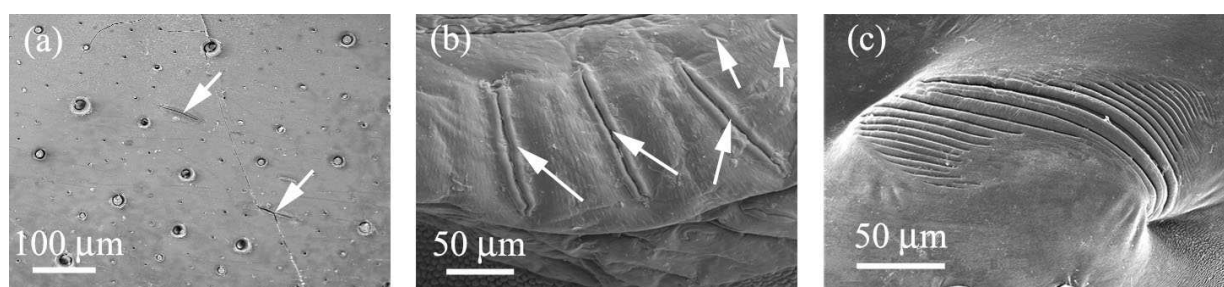


FIGURE 2.2: SEM images of slit sense organs of *C. salei*. **a** Single slits on the sternum, **b** loose grouping on the petiolus, and **c** lyriform organ HS2 on the trochanter. From Müllan (2005).

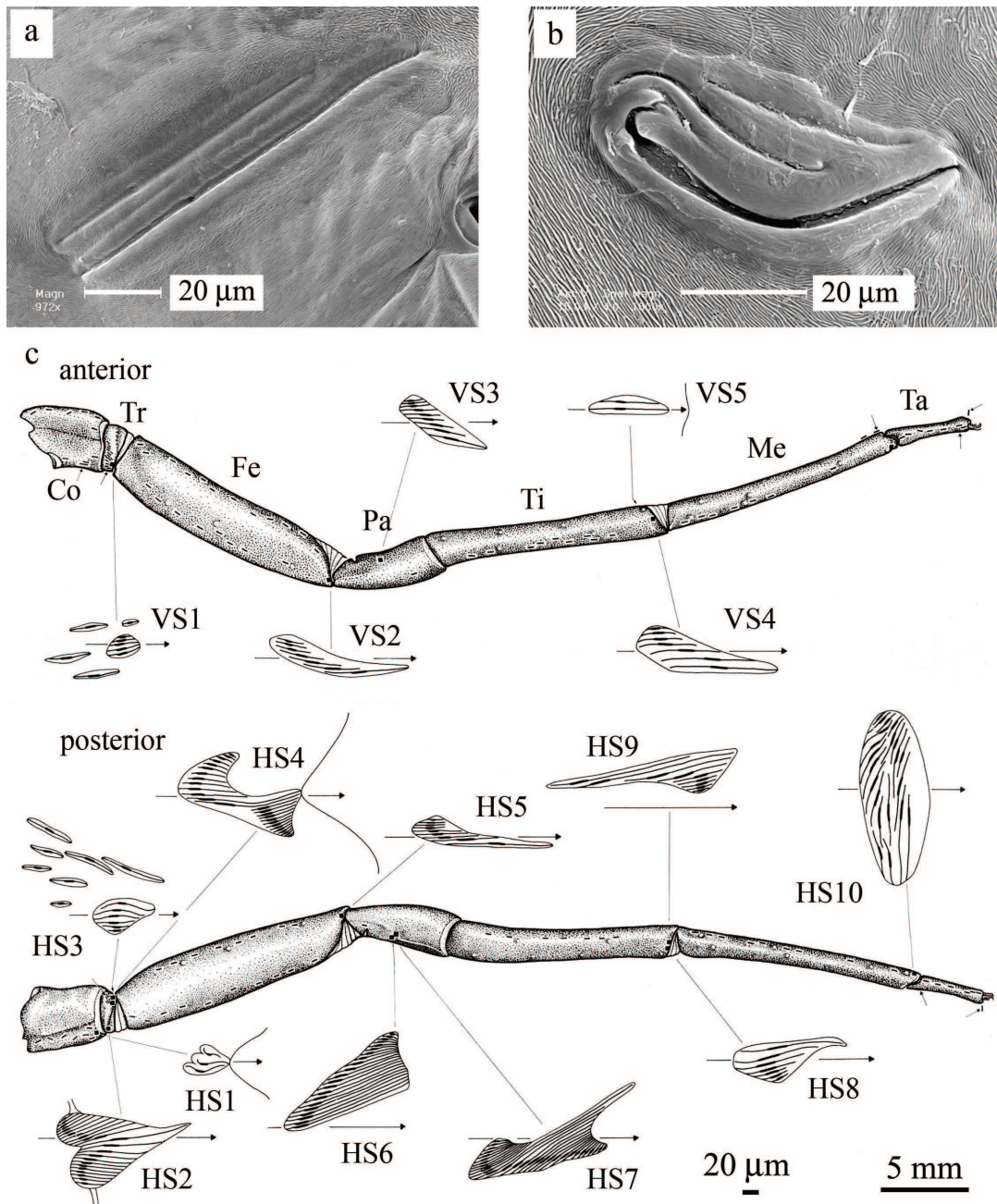


FIGURE 2.3: Slit sense organs of *Cupiennius salei*. **a** lyriform organ VS5 on the tibia, and **b** lyriform organ HS1 on the coxa (Müllan, 2005), **c** anterior (VS series of organs) and posterior sides (HS series of organs) of each leg of *C. salei* showing the different arrays and positions of the lyriform organs; scale bars pertain to leg and enlarged lyriform organs of the VS and HS series, respectively (Barth and Libera, 1970).

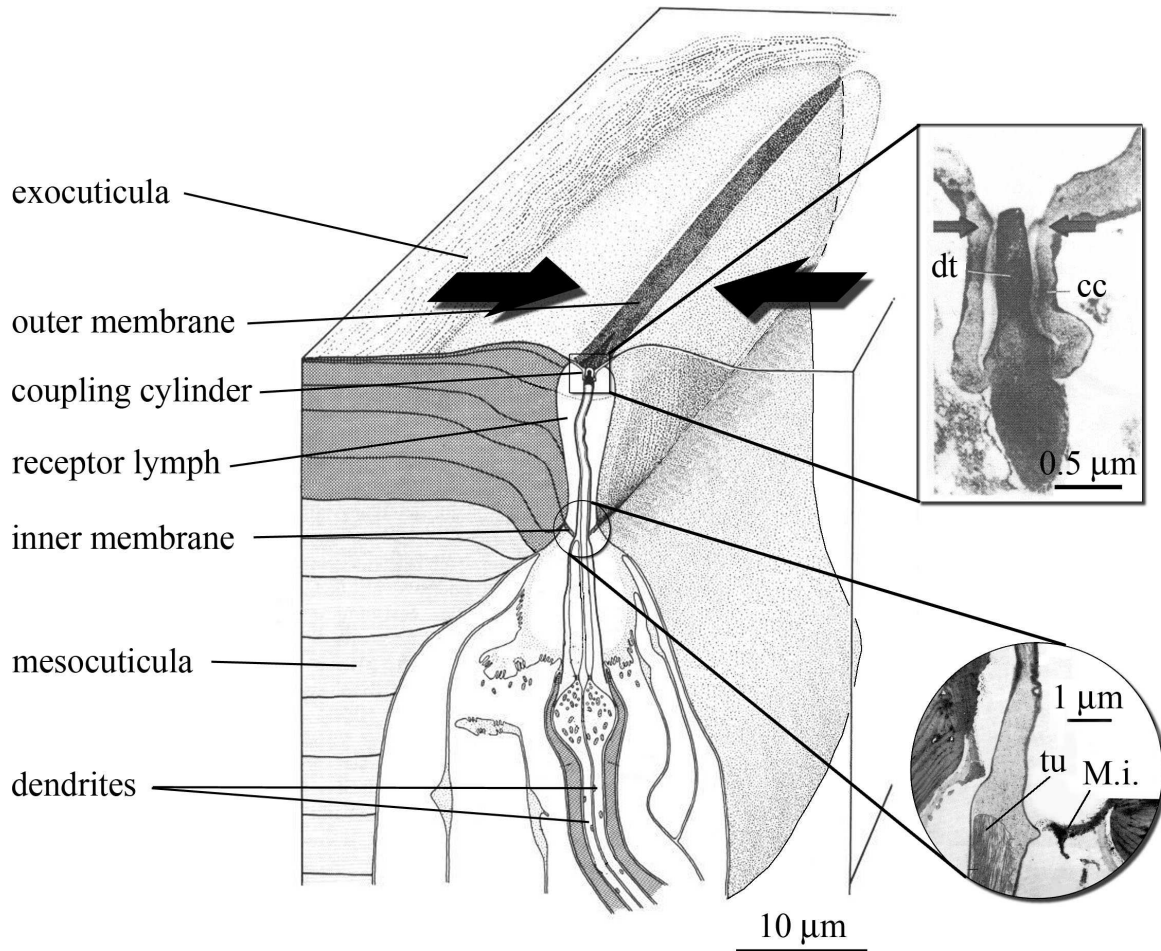


FIGURE 2.4: Schematic drawing of the mid section of a single slit cut in transverse direction. The orientations of the lamellae are indicated as lines in the exo- and mesocuticula. Only one of the two dendritic tips (dt) ends in the coupling cylinder (cc) of the outer membrane (see details). Inside the slit there is receptor lymph. tu tubular body of the dendrite ending at the inner membrane; M.i. inner membrane (modified from Barth (2002a)).

are oriented roughly parallel to the latter's long axes, and, with a few exceptions, lie on the proximal side of joints (see Fig. 2.3c). Individual slits within lyriform organs usually are more or less straight but can also be C-shaped or S-shaped (Fig. 2.3a and b).

The slits have lengths l of up to 150 μm and widths w_0 of 1 to 2 μm; their aspect ratios l/w_0 reach values of up to 100. They are covered on the outside by an inwards bulged, trough-shaped membrane that is approximately 0.25 μm thick (see Fig. 2.4). The dendrite

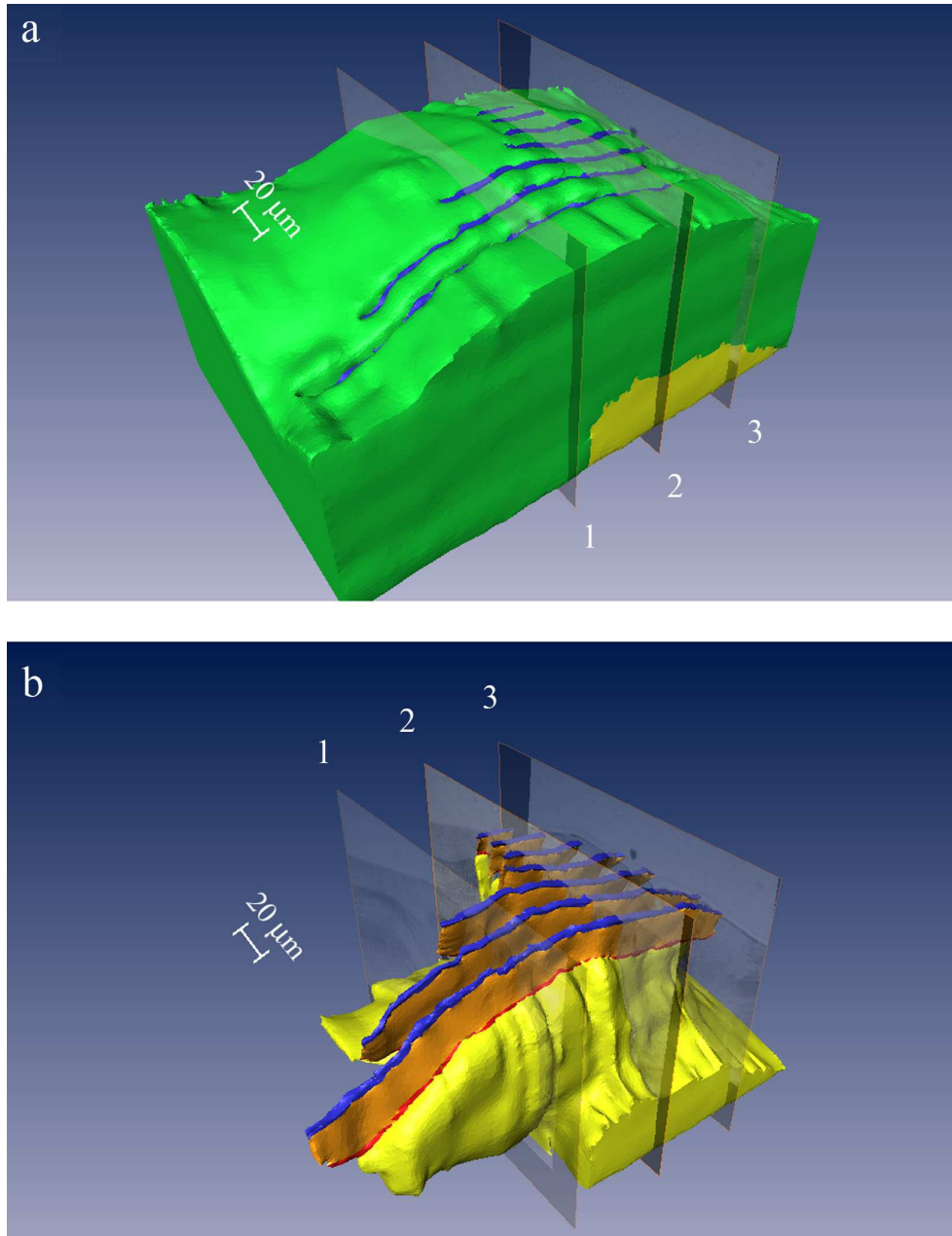


FIGURE 2.5: 3D reconstruction of the lyriform organ HS8 of *C. salei*. **a** with and **b** without cuticula. 1, 2, and 3 indicate cross sections. Color code: green cuticula; yellow extracellular cavity; blue outer membrane; red inner membrane; orange slit (Müllan, 2005).

tip of a bipolar sensory cell is attached to this covering membrane by a special structure, the coupling cylinder (see detail Fig. 2.4), and ends in its interior. Only compressive defor-

mations of the cuticle, which may result from different kinds of loadings, elicit a response of the dendrite (Barth, 1972a,b). There is also an inner membrane which, in contrast to the morphologically homogeneous (probably resilin-like) outer membrane, consists of fibrous material. Inside the slits there is receptor lymph rich in sodium ions (Rick et al., 1976; French et al., 2002). A special feature of slit sensilla is the presence of a second dendrite that ends close to the inner membrane, but is not directly coupled to it mechanically (see detail in Fig. 2.4). The role of this dendrite is still in doubt (Barth, 1971; French et al., 2002). More proximally the extracellular cavity opens including the soma of the dendrites. Details of the shapes of individual slits can be obtained by serial sectioning which provides the basis for three-dimensional visualization with software tools such as Amira (TGS Inc., San Diego, CA). In such a study Müllan (2005) recently demonstrated that in lyriform organs the slits fully penetrate the cuticle within a few micrometers of their tips and, as a consequence, can be well represented by openings cut into disks or shells (see Fig. 2.5).

2.2 Cuticle - a natural composite shell

Exoskeletons are typical of arthropods and a number of studies have been performed on their material parameters (Neville, 1975; Hepburn, 1976; Chapman, 1999; Vincent and Wegst, 2004). In flying insects or fast moving arthropods weight is an important factor. Using chitin, a polysaccharide closely related to cellulose, as the fibrous component embedded in a protein matrix a light and stiff composite shell is obtained. In insect cuticle a hundred or more different proteins are present (Chapman, 1999). The stiffness of the cuticle is controlled by cross-linking the protein molecules, referred to as tanning or sclerotization, so that they form a stiff matrix, and by interaction of the proteins with chitin (Vincent, 2002a). Wigglesworth (1988) proposed that lipids, together with the sclerotized proteins, play a significant role in cuticle hardening. In the mandibles and other especially hard parts of insect cuticle heavy metals, e.g. zinc, manganese or occasionally iron, are present in relatively large amounts of up to 1% of the dry weight of the cuticle (Chapman, 1999). In aquatic arthropods, e.g. crustacea, for which weight plays a lesser role, calcium carbonates (calcite, vaterite, hydroxyapatite) are added to the composite and dominate the mechanical parameters. In the cuticle of *Cancer pagurus* the mineral crystals are arranged in rows parallel to the pore canals (Stevenson, 1985).

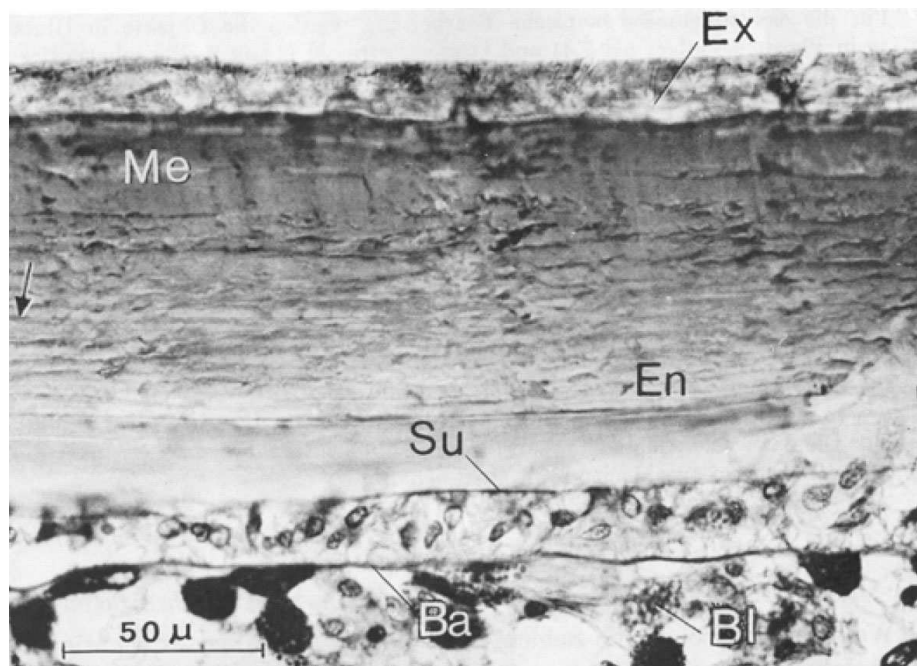


FIGURE 2.6: Light microscope image of a cross section of the cuticle of the tarsus of *C. salei* (staining according to Gomori-Halmi). Ex exocuticle; Me mesocuticle; En endocuticle; Su subcuticle; Ba basal membrane; Bl blood cells (Barth, 1969).

Measurements of the material parameters of mineralized organic cuticles are rare, but it has been shown that cuticles containing calcium carbonate or calcium phosphate can have outstanding mechanical properties (Currey et al., 1982).

The exoskeleton of arachnids is composed of different zones: epi-, exo-, meso-, endo-, and subcuticle (order distal to proximal) (Barth, 1969). They are defined by staining according to Mallory (Romeis, 1968) or Gomori-Halmi (Aldehydfuchsin according to Gomori (Romeis, 1968) and counterstaining according to Halmi (Adam and Czihak, 1964)) (Fig. 2.6). In *C. salei* the epicuticle is about $0.5\ \mu\text{m}$ thick with corrugations of about 3 nm. It is composed of an outer dense layer, two lipid layers and a cement layer (Barth, 1969). The exocuticle dominates the stiffness of the integument where the stimulus uptake is found. The meso- and endocuticle cannot be distinguished clearly but are approximately ten times thicker than epi- and exocuticula. The subcuticle, which is the grainy innermost zone, is the latest secreted part on the cuticle. The thickness and the presence of the individual zones

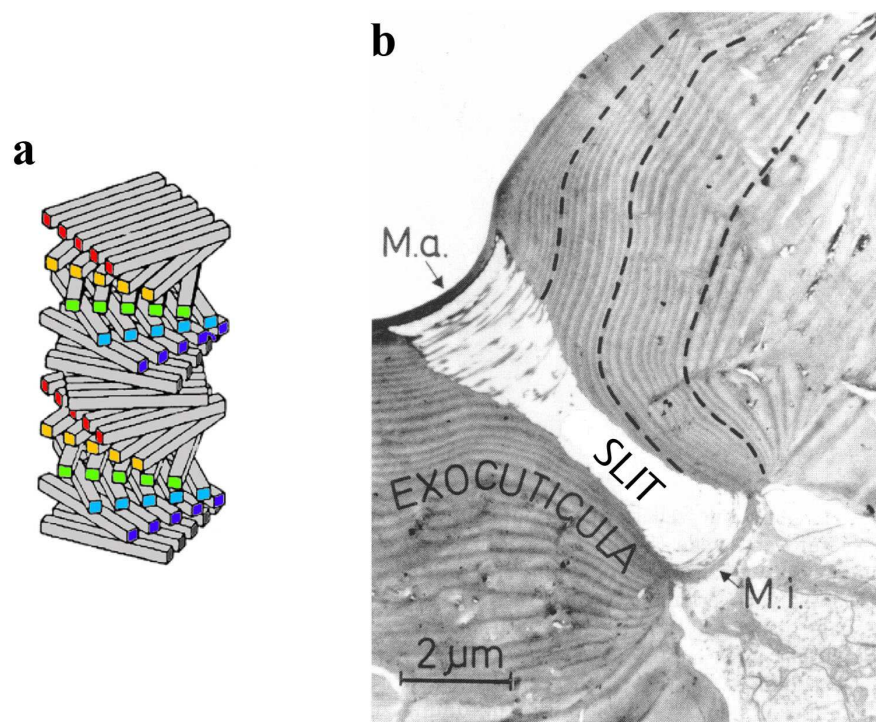


FIGURE 2.7: Microstructure of the cuticle. **a** monodomain helicoidal crystalline structure in the spider legs (Barth, 1973; Vincent, 2002b). **b** SEM image of a cross section of the big single slit on the tarsus of *C. salei*. The different lamellae are visible as sequences of dark and light bands. M.a. outer membrane; M.i. inner membrane (Barth, 1972a).

depend on the position on the exoskeleton. For example, articular membranes and the opisthosoma lack an exocuticle, and different thicknesses of the zones are found in different leg segments in the walking legs of *C. salei* (Barth, 1973). During moulting all the proteins not sclerotized in the cuticle are digested and re-used for building the new cuticle. Only the exuviae, which correspond to the stiff and highly tanned exocuticle, are left after ecdysis.

2.2.1 Microstructure of cuticle

Neville et al. (1976) studied the fiber diameter of chitin in 8 orders of insects, one crustacean, and one arachnid and found that the extreme values for the diameter of the micro fibers are 2.3 and 3.5 nm. These authors conclude that the above variations are due to the

inherent errors of the measurements and that the diameter of the crystallites is constant and has a value close to 2.8 nm. The length of the micro fibers is reported to range from approximately 24 to 730 nm (Neville, 1998). Vincent (2002b) claims that they are up to 1000 nm long depending on their degree of polymerization. In Vincent and Wegst (2004) a micro fiber length of 300 nm is reported. According to Filshie (1982) and Ker (1977) most micro fibers are about 360 nm long. For the opisthosoma of *C. salei* Barth (1973) reports a minimum micro fiber diameter of 3.5 nm, a fiber length of up to 1500 nm, and a minimum aspect ratio (length/diameter) of the fibers of 100.

Sheets reinforced by uni-directional micro fibers lie parallel to the surface in flat cuticle (Barth, 1970). The in-plane fiber orientations in the exocuticle change continuously through the thickness and, accordingly, match after a number of layers (Fig. 2.7a) (Barth, 1973, 2002a). The stiffness relevant part of the cuticle, the exocuticle, is about 10 μm thick in the walking legs of *C. salei* and consists of approximately 2000 layers of aligned micro fibers (Fig. 2.7b). From the engineering point of view the exocuticle forms a laminate consisting of many sublaminae, which are referred to as lamellae. In Fig. 2.7b the thickness of a single lamella corresponds to the distance between two neighboring darker regions. The lamellar thickness increases continuously and regularly from the outside to the inside in all exocuticles found in *C. salei* (Barth, 1973). Close to slit sense organs the laminae are no longer parallel to the cuticle's surface. In the transition zone between the exocuticle and the outer membrane of the slit the orientation of the most distal layer is tangential to the inwards bulged membrane. The angle between the planes of the fiber layers and the surface of the cuticle increases with the depth of the slit (see Fig. 2.7b and Fig. 2.8a and b). The lamellae that are connected to the fibrous inner membrane are aligned with the direction of the tangent at the edge of the inner membrane. This avoids stress concentrations in the transition zone between the membranes and the lamellae. The majority of the lamellae are not connected to one of the two membranes and end at the inner surface of the slit or at the surface of the extracellular cavity (Fig. 2.7b).

2.2.2 Effective mechanical properties of cuticle

Fiber reinforced composites, a group of materials that includes arthropod cuticle, consist of stiff fibers that give the material stiffness and strength and a typically more compli-

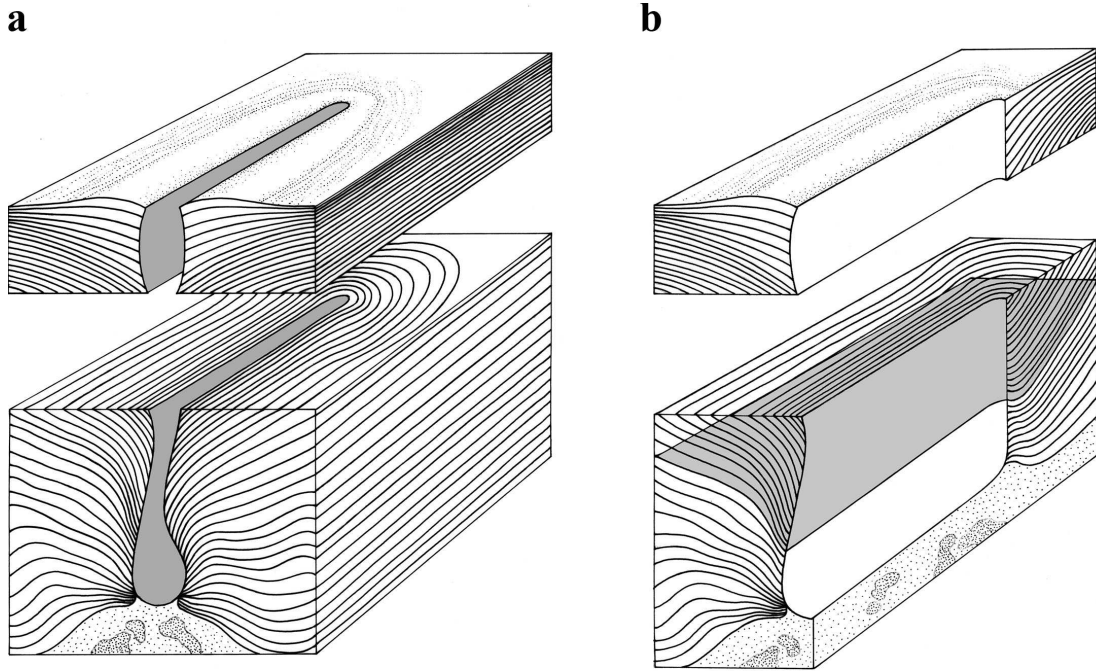


FIGURE 2.8: Alignment of the lamellae in the exocuticle close to a slit of *C. salei*. The upper third of the slit is distally shifted and the outer membrane is removed for a better understanding. **a** lateral and **b** longitudinal cross section of the slit. The tangent of the membranes and the lamellae is the same at their transition to avoid stress concentrations (Müllan, 2005).

ant matrix that transfers loads between the fibers and prevents buckling of the fibers in deformation. Depending on the fiber orientations and arrangements fiber reinforced composites in most cases show anisotropic overall stiffness and strength. This also holds true for laminated composites which are built up from a number of layers or laminae. In such materials the in-plane stiffnesses and strengths typically are markedly higher than the corresponding out-of-plane properties. In contrast to many man-made composites the variability of the mechanical properties of arthropod cuticle is enormous, because natural composites are subjected to fewer “producibility constraints” and, accordingly, can make full use of their inherent tailorability. The mechanical behavior of such inhomogeneous materials is described in terms of effective moduli, i.e., material parameters that pertain to an energetically equivalent homogeneous medium at a sufficient large length scale.

As stated by lamination theory (see e.g. Jones (1999)) a minimum of 3 layers of appropriate

orientation are necessary for a layered material to be quasi-isotropic under in-plane loading. Because there are at least 7 layers for the thinnest lamellae in the exocuticle of *C. salei*, the latter can be treated as macroscopically isotropic for in-plane loading (Barth, 1973).

2.2.2.1 Constituent properties of cuticle

In the literature a wide range of stiffness values for the chitin nanofibers can be found, but, to the authors' knowledge, the stiffness has never been actually measured. Vincent and Wegst (2004) estimated a value of at least 150 GPa, based on observations of cellulose in the cell walls of plants, which has a stiffness of about 130 GPa. The difference is explained by extra bonding in the chitin crystallites that tends to stiffen chitin further. Ker (1977) suggests a Young's modulus of at least 100 GPa and Currey (1970) of about 44 GPa. The influence of hydration on the mechanical properties of the micro fibers is marked. For the mesosternum of the coleopteran *Pachynoda sinuata* Hepburn and Ball (1973) report a difference in Young's modulus of a factor of approximately 4.6 between dry and wet micro fibers. Hepburn and Levy (1975) claim that the Young's modulus of the micro fibers in the meropodite of the crustacean *Scylla serrata* is 1095 MPa for dry and 330 MPa for wet micro fibers. For the protein matrix the stiffness values are reported to range from approximately 1 kPa to some 1 GPa, depending on the degree of sclerotization (Vincent, 1998).

According to the water content of the integument and the volume fractions of chitin and protein different Young's moduli of the cuticle can be obtained. Equal weight fractions (dry) of the constituents and a water content of about 40-75% are present in soft cuticle whereas hard cuticle contains 15-30% by weight fraction of chitin and only 12% of water (Vincent and Wegst, 2004). In contrast Neville et al. (1976) claim that the fiber volume fraction is approximately 21% for dry rubberlike cuticle of the prealar arm (arm for attaching the wings) of the locust *Schistocerca gregaria*. Barth (1973), Hillerton (1980), and Neville (1975) report micro fiber volume fractions ranging from 10 to 50%.

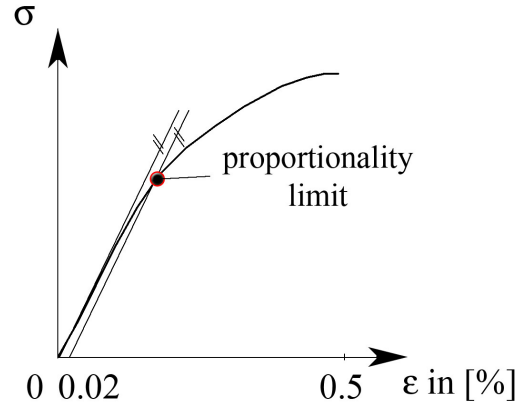


FIGURE 2.9: Determination of the proportionality limit in $\sigma - \varepsilon$ diagrams of biomaterials by a line parallel to the linear portion of the measured curve drawn at an offset of 0.02% of ε .

2.2.2.2 Effective Young's modulus of cuticle

In analogy to the definition of the yield stress σ_{02} for metals in biomaterials the elastic deformation does not exhibit a clearly defined limit. Therefore the offset method is used to determine the stress at the proportionality limit. A line parallel to the straight portion of the stress-strain ($\sigma - \varepsilon$) curve is drawn at the offset position of 0.02% on the strain axis (Fig. 2.9) and the intersection point is defined as the stress of the proportionality limit. The slope of the initial straight portion of the stress-strain curve is taken to be the Young's modulus. Alternatively, nanoindentation testing can be used to determine the Young's modulus. Song et al. (2004) reported stiffness values measured by both methods for the forewings of *Cicada*, that are in good agreement, even though the indentation was performed in the usually more compliant out-of-plane direction.

In some insects the Young's modulus of the cuticle can be actively controlled. The blood-sucking bug *Rhodnius* drops the pH value of the cuticle from 7 to below 6 and thereby increases the charge density in the cuticular protein. As a consequence, the cuticular water content increases from about 26 to 31%, which is claimed to reduce the stiffness of the cuticle from 250 to 10 MPa and increases its extensibility from 10% to more than 100% (Reynolds, 1975)¹⁾. In contrast, the measurements of Smith et al. (2000) show

¹⁾ From the point of view of material mechanics the reported stiffness change by a factor of 25 is remarkable.

that the stiffness of the wings of the desert locust is not very strongly affected by the relative humidity of the surrounding air. The Young's modulus increases from 13.5 GPa to 16.5 GPa when the relative humidity changes from 75% to 40%. In addition to the comments on the measurements performed by Song et al. (2004) in the above paragraph this behavior may be another indication that the micro fiber volume fraction in the wings is relatively low. On the other hand this may also indicate that the stiffness of the matrix must be higher than 1 GPa. A similar behavior is reported by Barbakadze et al. (2006) where the influence of desiccation on the Young's modulus of the cuticle of the head-to-neck articulation of the beetle *Pachnoda marginata* was investigated. When the water content decreases by ≈ 15 to 20% of the cuticle mass the Young's modulus increases from 1.5 to 7.5 GPa. Another change in the material parameters happens in the locust extensible intersegmental membrane, where the fiber volume fraction is low and the stiffness is controlled by hormones (Tychsen and Vincent, 1976).

In Table 2.1 examples of effective Young's moduli for different biomaterials are given.

2.2.2.3 Effective tensile strength and strain at failure of cuticle

Strength values for chitin found in the literature range from 2.2 MPa (Joffe et al., 1975) to 569 MPa (Herzog, 1926) and 570 MPa (Currey, 1970), respectively. No strength data is available in the literature for the matrix because the proteins are difficult to isolate (Wainwright et al., 1982).

The tensile strength of hydrated locust cuticle is given as 60-200 MPa, which is about 1-5 % of the stiffness (2-6 GPa), by Vincent and Wegst (2004). Jensen and Weis-Fogh (1962) report a tensile strength of 95 MPa for the tibia of the desert locust *Schistocerca*. Hepburn and Ball (1973) claim that the tensile strength in the elytron of the Coleopteran *Pachnoda* is 69 MPa. In the membranes of the forewing of *Cicada* (Homoptera, Cicadidae) the measured tensile strength is 29 MPa (Young's modulus 3.7 GPa) and in the veins along the venation of the wings 52 MPa (Young's modulus 1.9 GPa), respectively (Song et al., 2004). Hillerton (1979) reports an ultimate tensile strength of 22 MPa for the extensible cuticle of *Rhodnius*. In hydrated locust cuticle the strain at failure is up to 5% (Vincent and Wegst, 2004).

TABLE 2.1: Examples of effective Young's moduli reported for some biomaterials; the lower part gives values for different types of cuticle.

Material	Young's modulus	Reference
Locust intersegmental membrane	1 kPa	Vincent and Wegst (2004)
Pregnant locust intersegmental membrane	200 kPa	Vogel (2003)
Protein polymer resilin	1 MPa	Vincent and Wegst (2004)
Protein polymer resilin	1,2 MPa	Gosline (1980)
Dragonfly tendon, mainly resilin	1,8 MPa	Vogel (2003)
Dragonfly ligament, mainly resilin	2,2 MPa	Weis-Fogh (1961); Vincent (1980)
Protein polymer abductin	4 MPa	Alexander (1966)
<i>Calliphora vomitoria</i> well tanned puparium	250 MPa	Vincent and Hillerton (1979)
Dragonfly wing membrane	1,5 GPa	Kreuz et al. (1998)
Cicada wing veins	1,9 GPa	Song et al. (2004)
Dragonfly dry wing veins	2,9 GPa	Kreuz et al. (1998)
Cicada wing membranes	3,7 GPa	Song et al. (2004)
Spruce wood (secondary cell wall)	16,1 GPa	Gindl and Gupta (2002)
Bone (compacta, large mammal)	18 GPa	Vogel (2003)
Locust tibial flexor apodeme	20 GPa	Ker (1977)
Bone (dried compacta, cow)	20.3–27.6 GPa	Hengsberger et al. (2003)
<i>Trochus niloticus</i> inner nacreous layer	92 GPa	Bruet et al. (2005)
<i>Drosophila melanogaster</i> cuticle (puparium, adult <i>in vivo</i>)	4,37 MPa	Kohane et al. (2002)
<i>Rhodnius</i> abdominal cuticle	60 MPa	Reynolds (1975)
Desert locust cuticle (hind femur)	1.205 GPa	Hepburn (1975)
Desert locust cuticle (tibia)	1.8 GPa	Ker (1977)
Desert locust cuticle (hind tibia)	4.6 GPa	Katz and Gosline (1994)
Dragonfly dry cuticle (abdominal tergite)	4.7 GPa	Kreuz et al. (1998)
Desert locust cuticle (hind tibia)	9.5 GPa	Jensen and Weis-Fogh (1962)
Locust cuticle (apodeme; mainly chitin)	11 GPa	Ker (1977)
<i>Cupiennius salei</i> cuticle (tibia)	18 GPa	Blickhan and Barth (1985)
<i>Cassida viridis</i> cuticle (elytron)	23 GPa	Krzelj (1969)

2.2.2.4 Effective Poisson's ratio of cuticle

Values for the Poisson's ratio of arthropod cuticle are rare in the literature and no major studies appear to have examined this parameter. In Combes and Daniel (2003) a Finite Element analysis of the flexural stiffness in hawkmoth and dragonfly wings is performed using a Poisson's ratio of 0.49, and it is reported that the influence of a Poisson's ratio of 0.3 on the results is negligible. Kesel et al. (1998) used a Poisson's ratio of 0.25 for Finite Element analysis of a dragonfly's forewing without commenting their choice. Flannigan (1998) compared the cuticle of insects to a more frequently studied fibrous material, wood, and estimated a Poisson's ratio of 0.3, which was used in his planar Finite Element models of a cockroach tibia. Cocatre-Zilgen and Delcomyn (1999) followed a similar approach for estimating the Poisson's ratio of 0.3 used in their analytical models of a cockroach tibia. These estimates are, however, doubtful because the microstructures of wood and cuticle are different. In Finite Element models of strain sensitive campaniform sensilla present in insect cuticle Skordos et al. (2002) used an in-plane Poisson's ratio of 0.077 and an out-of-plane Poisson's ratio of 0.31 in accordance to measurements of a composite with eight layers of uni-directional oriented glass fibers of fiber volume fraction of 69%. The cuticle, which is rather stiff, may also be compared to bone (compacta) with a Poisson's ratio ranging between 0.13 and 0.3 (Vincent, 1982).

As Fig. 2.10 shows, using Poisson's ratios close to 0.5 is unrealistic for layered fibrous materials such as cuticle, and the anisotropy of this laminate must be accounted for in non-planar analyses. High Poisson's ratios may, however, well be appropriate for soft tissues or for the proteinaceous matrix of cuticle.

2.2.2.5 Micromechanical assessment of the stiffness of cuticle

The exact mechanical properties of the transversely isotropic spider cuticle including Young's and shear moduli and the Poisson numbers in the in- and out-of-plane direction are necessary for the Finite Element (FE) models of the slits. They have to be estimated because to the knowledge of the authors they have never been actually measured with the exception of the in-plane Young's modulus. In continuum micromechanics (Böhm, 2004) the effective properties of inhomogeneous materials are estimated from the constituent

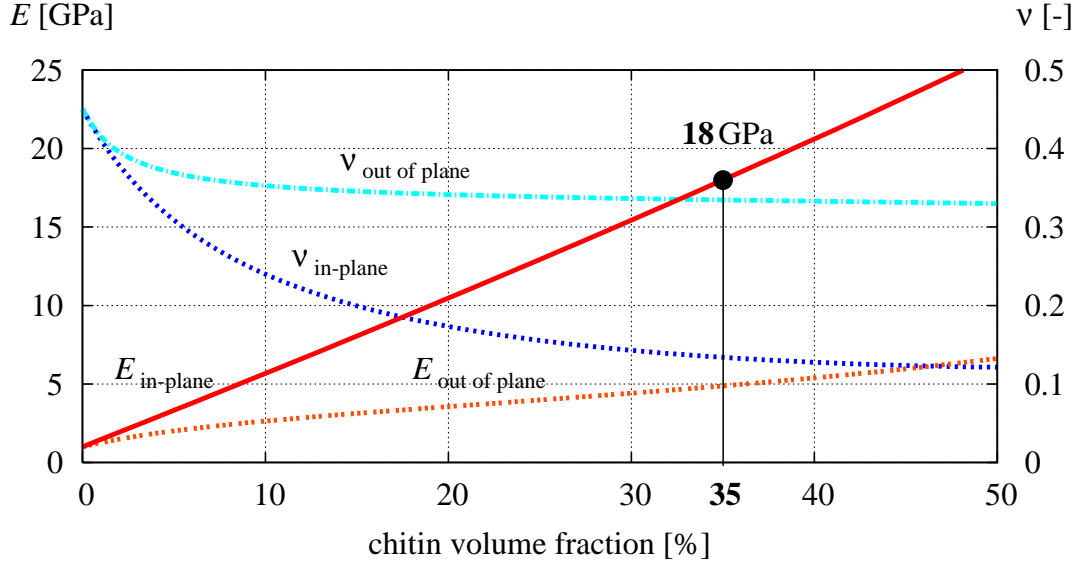


FIGURE 2.10: Estimates of the effective material parameters Young's modulus (E) and the Poisson's ratio (ν) depending on the chitin volume fraction of a composite with planar random fibers assuming perfect interface between the matrix and the fibers. The constituent data are listed in Table 2.2.

properties using continuum mechanics. Huang (2001) proposed a laminate analogy model for composites with planar random reinforcements that uses a Mori-Tanaka approach (Mori and Tanaka, 1973) to account for fiber length effects, which is valid for perfect interfaces between the fibers and the matrix. This model can be used to assess the dependence of the effective elastic behavior of cuticle on parameters such as chitin volume fraction. Exploratory analysis can give an idea on how the effective Young's modulus and the effective

TABLE 2.2: Material parameters of the constituents for rough estimates of the effective material parameters of a protein-chitin composite with planar random fiber orientation and perfect interface.

property	matrix	reinforcement
aspect ratio	-	120
Young's modulus	1 GPa	150 GPa
Poisson's ratio	0.45	0.3

Poisson's ratio change as functions of the chitin volume fraction (Fig. 2.10) and of the material properties of chitin and the proteinaceous matrix. The material parameters of the constituents used for estimating the effective material parameters are listed in Table 2.2; the Young's moduli of the constituents given there are well within the range of values reported in the literature (Currey, 1970; Ker, 1977; Vincent, 1998; Vincent and Wegst, 2004). The differences between the in-plane and out-of-plane effective material parameters increase with increasing chitin volume fraction, which is typical for composites with high elastic contrast. The out-of-plane and especially the in-plane Poisson's ratios decrease markedly with increasing fiber volume fraction.

From the point of view of continuum micromechanics of composites the following changes tend to make cuticle more compliant:

- decrease of the stiffness of the micro fibers by increasing their water content (Hepburn, 1976),
- decrease of the stiffness of the matrix by changing the amount of sclerotization,
- decrease of the aspect ratio of the micro fibers, and
- decrease of the chitin volume fraction.

In addition, from a meso- or macromechanical point of view an increase of the out-of-plane component of the fiber orientations tends to reduce the in-plane stiffness and to increase the out-of-plane stiffness, e.g. waviness of the lamellae in the opisthosoma of *C. salei* (Barth, 1973).

For an in-plane Young's modulus of 18 GPa, which is in line with Blickhan & Barth's (1985) estimate the stiffness of the cuticle of the tibia of *C. salei*, a fiber volume fraction of approximately 35% is required with the constituent properties listed in Table 2.2. This chitin volume fraction is well within the range of 10-50% which is reported by Barth (1973), Hillerton (1980), and Neville (1975). The corresponding in-plane Poisson's ratio is approximately 0.13.

Due to the limited information available on the mechanical properties of the chitinous fibers and protein matrix micromechanical methods can only provide estimates on the effective

mechanical properties of the cuticle. Accordingly, assumptions are required in selecting material data sets for modeling. Table 2.3 lists the effective material parameters used for cuticle in the present work, with E_A and E_T standing for the out-of-plane (axial) and in-plane (transversal) Young's moduli, G_A for the out-of-plane shear modulus and ν_A and ν_T for the out-of-plane and in-plane Poisson numbers, respectively. Simulations showed that the value of the in-plane Poisson number does not appreciably influence the numerical predictions for the deformation patterns of plane stress models of slits for which out-of-plane deformations do not have an influence on the slit face deformations. This allowed a value of $\nu_T = 0.3$, which is in line with previous studies in the literature, to be used for the plane stress analyses reported in Chapters 4 and 4.2. For three-dimensional shell and continuum models the use of transversely isotropic material properties typical for spider cuticle, of course, is necessary.

TABLE 2.3: Effective material properties used in the FE models. Values for transversely isotropic material behavior according to estimates (Huang, 2001) and for the isotropic behavior in agreement with Blickhan and Barth (1985) (E_T) and Vincent (1982) and Flannigan (1998) (ν_T). E_A out-of-plane (axial) Young's modulus; E_T in-plane (transversal) Young's modulus; G_A the out-of-plane shear modulus; ν_A out-of-plane Poisson number; ν_T in-plane Poisson number.

model type	E_A	E_T	G_A	ν_A	ν_T
planar	-	18 GPa	-	-	0.3
3D	4.9 GPa	18 GPa	690 MPa	0.33	0.13

2.2.2.6 Material behavior of cuticle

All stress-strain curves for chitinous composite materials found in the literature (Hepburn, 1975, 1976; Hepburn and Ball, 1973; Hepburn and Roberts, 1975; Hillerton and Purslow, 1981; Joffe et al., 1975; Ker, 1977; Neville, 1975; Smith et al., 2000; Song et al., 2004; Vincent, 1980; Vincent and Hillerton, 1979; Weis-Fogh, 1961) are non-linear, but for small strains of less than 0.02% the material behaves linearly elastic. Joffe and Hepburn (1973) reported linear elastic behavior under small loads and small rates of strain, but indicated that the viscous properties must be accounted for when evaluating tensile tests. Jensen and Weis-Fogh (1962) showed that the cuticle of the locust tibia performs similarly in

tension and deformation for small loads. In modeling work presented in the literature Vincent (1998) assumed a linear elastic material model and Hillerton et al. (1982) used a linear elastic ideally plastic material model for the fibrous cuticle without commenting their choice.

Chapter 3

Methods

3.1 Analytical approach

3.1.1 On the problem of crack interaction

One of the motivations for obtaining analytical solutions for calculating the stress intensity factors (SIFs) of closely spaced cracks is to estimate the effective elastic properties of elastic solids containing many cracks or fields of microcracks (Kachanov, 1987, 1994). Another benefit of this solution is that the crack face displacements of interacting cracks can be estimated (Gorbatikh and Kachanov, 2000).

In Chapter 3.1.3 Kachanov's method (Kachanov, 1987, 1994) for approximating the crack face displacements of interacting cracks is presented. Li et al. (2003) and Benveniste et al. (1989) expanded on this idea and improved the results in terms of application to problems of more closely spaced slits (see Chapter 3.1.4).

Gross (1982), Horii and Nemat-Nasser (2000), and Nishioka et al. (1997) presented alternative analytical descriptions for the problem of interacting cracks.

3.1.2 Stress fields generated by cracks

In linear elastic fracture mechanics the stress fields generated by a loaded crack can be represented as superposition of the fields produced by the tensile (mode I), shear (mode II) and antiplane (mode III) contributions to the load. For an isolated crack in an infinite medium these modes are decoupled, which means that a given mode of loading produces a crack opening displacement D of the same mode only. The normalized, i.e. dimensionless,

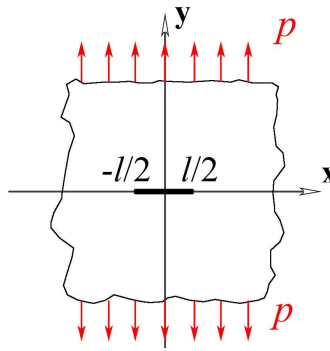


FIGURE 3.1: Single isolated crack under unit tensile (mode I) loading p in y -direction.

stress field of a crack, occupying the interval $[-l/2, l/2]$ of the x -axis (Fig. 3.1), under mode I loading is depicted in Fig. 3.2 where the stress singularities are obvious. The formulae used to evaluate the normalized stress field can be found in Appendix A. Note that in the vicinity of the crack the region of negative (compressive) stress σ_{yy} is bigger than the region of positive (tensile) stress σ_{yy} . An isolated single crack under mode I loading generates an extended “shadow” and a relatively small “amplification” zone. This becomes important in crack interaction and explains that shielding in a stack of parallel cracks has a longer range than the amplification in collinear cracks. Accordingly, a stack of parallel cracks is the most sensitive array in terms of crack interaction. Therefore it was chosen for assessing the accuracy of Kachanov’s method.

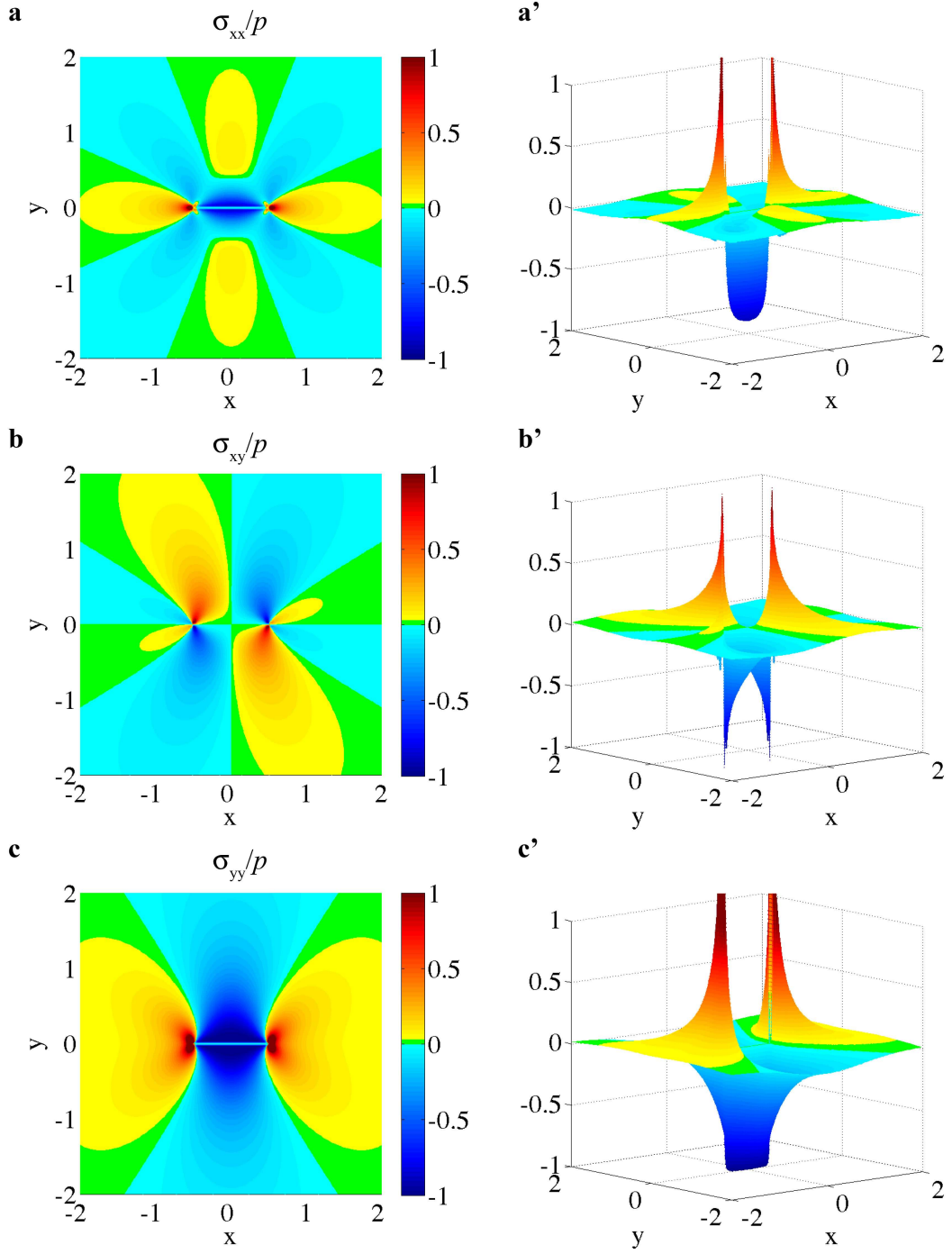


FIGURE 3.2: Mode I normalized standard stress field generated by a single isolated crack under unit loading p in y -direction. **a** and **a'** stress component in x -direction σ_{xx}/p , **b** and **b'** stress field of the shear component σ_{xy}/p , **c** and **c'** stress component in y -direction σ_{yy}/p . Note that in the vicinity of the crack the area of negative σ_{yy}/p (shielding) is larger than the area of positive σ_{yy}/p (amplification). Therefore interactions effects are more pronounced in stacks of cracks compared to collinear arrangements.

3.1.3 Kachanov's method

A method proposed by Kachanov (Kachanov, 1994; Gorbatiikh and Kachanov, 2000) allows to obtain approximate solutions for the crack face displacements (D) of an arbitrary number of traction-free interacting cracks in an infinitely extended linear elastic solid that is loaded by known far field tractions \mathbf{T}^∞ .

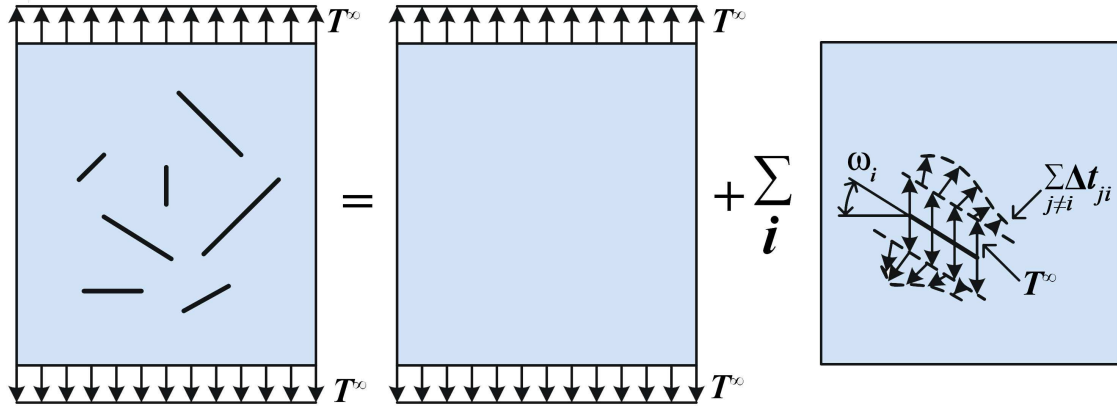


FIGURE 3.3: Basic idea of stress superposition (Kachanov, 1994): problem of a disk containing N cracks that is loaded by tractions \mathbf{T}^∞ is transformed into a crack-free disk loaded by \mathbf{T}^∞ plus N subproblems involving one crack each which is loaded by unknown tractions $\mathbf{t}_i(\xi_i)$ on its faces.

In this approach arrangements of N cracks in an infinite disk under load are described by a superposition technique. The latter combines a crack-free solid subjected to far field tractions \mathbf{T}^∞ with N subproblems, each of which involves one crack that is loaded by unknown traction distributions $\mathbf{t}_i(\xi_i)$ acting on the crack faces (Fig. 3.3). For calculating the stress intensity factors (SIFs) at the crack tips describing the stress amplification and, on their basis, the displacements of the crack faces, the tractions $\mathbf{t}_i(\xi_i)$ along each crack are required. Each of these tractions $\mathbf{t}_i(\xi_i)$ can be decomposed into contributions due to the applied far field traction \mathbf{T}^∞ and to the traction distribution $\Delta \mathbf{t}_{ji}(\xi_i)$ induced at crack

a

$$p_1(\xi) = p^\infty + \Delta p_{21}(\xi)$$

$$p_2(\xi) = p^\infty + \Delta p_{12}(\xi)$$

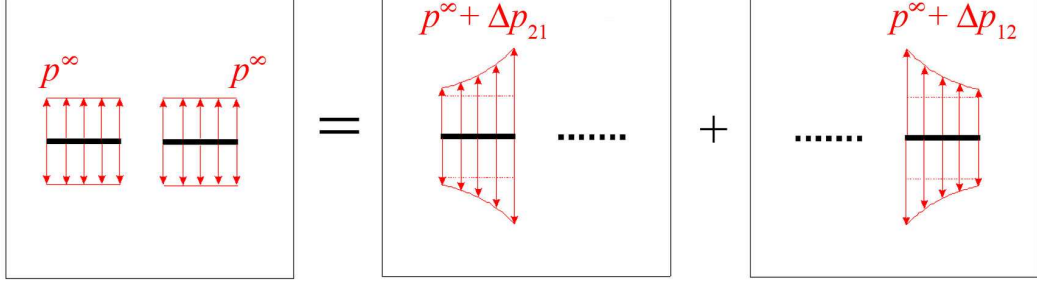
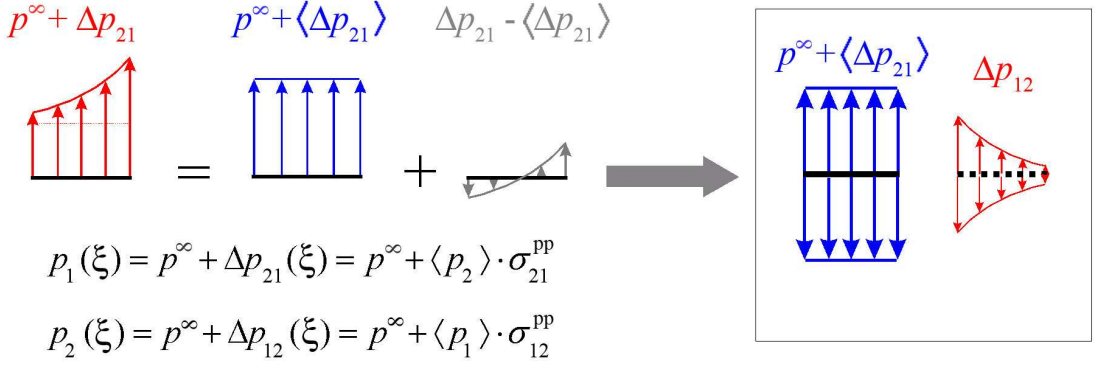
**b**

FIGURE 3.4: Example of two interacting collinear cracks. **a** The tractions along the crack faces can be decomposed into the far field traction p_0 and tractions due to interaction Δp_{21} and Δp_{12} . **b** For determining the interaction terms of the tractions only the average tractions $p_0 + \langle \Delta p_{21} \rangle$ and $p_0 + \langle \Delta p_{12} \rangle$ are used. Note that the shear tractions induced at the faces of one crack when the other crack is loaded by normal tractions were not taken into account.

i by each of the other cracks j loaded by $\mathbf{t}_j(\xi_j)$,

$$\mathbf{t}_i(\xi_i) = \begin{Bmatrix} p_i(\xi_i) \\ \tau_i(\xi_i) \end{Bmatrix} = \mathbf{H}(\omega_i) \mathbf{T}^\infty + \sum_{j \neq i} \Delta \mathbf{t}_{ji}(\xi_i), \quad (3.1)$$

where $p_i(\xi_i)$ and $\tau_i(\xi_i)$ are the normal and shear components of the traction vector $\mathbf{t}_i(\xi_i)$. The tensor $\mathbf{H}(\omega_i)$ rotates the coordinate system into alignment with the crack and ξ_i is the position along crack i .

The key approximation in Kachanov's method is to evaluate the interaction terms $\Delta \mathbf{t}_{ji}(\xi_i)$ from the average traction acting on crack j , $\langle \mathbf{t}_j \rangle$, instead of the actual nonuniform traction $\mathbf{t}_j(\xi_j)$ (Fig. 3.4). This allows Eq. (3.1) to be written as

$$\mathbf{t}_i(\xi_i) = \mathbf{H}(\omega_i) \mathbf{T}^\infty + \sum_{j \neq i} \langle \mathbf{t}_j \rangle \boldsymbol{\sigma}_{ji}(\xi_i) , \quad (3.2)$$

where $\boldsymbol{\sigma}_{ji}(\xi_i)$ stands for the normalized, i.e dimensionless, stress field at the faces of crack i that is generated when crack j is subjected to a uniform unit traction (compare Appendix A). By evaluating averages of the $\mathbf{t}_i(\xi_i)$ from Eq. (3.2) a system of linear equations is obtained for the average tractions acting on the cracks,

$$\langle \mathbf{t}_i \rangle = \mathbf{t}_i^\infty + \sum_{j \neq i} \langle \mathbf{t}_j \rangle \boldsymbol{\Lambda}_{ji} , \quad (3.3)$$

or, rewritten,

$$\begin{Bmatrix} \langle p_i \rangle \\ \langle \tau_i \rangle \end{Bmatrix} = \begin{Bmatrix} p_i^\infty \\ \tau_i^\infty \end{Bmatrix} + \sum_{j \neq i} \begin{Bmatrix} \langle p_j \rangle \\ \langle \tau_j \rangle \end{Bmatrix} \begin{bmatrix} \Lambda_{ji}^{pp} & \Lambda_{ji}^{p\tau} \\ \Lambda_{ji}^{\tau p} & \Lambda_{ji}^{\tau\tau} \end{bmatrix} , \quad (3.4)$$

with

$$\Lambda_{ji}^{mn} = \frac{1}{l_i} \int_{-l_i/2}^{l_i/2} \sigma_{ji}^{mn}(\xi_i) d\xi_i . \quad (3.5)$$

The scalars Λ_{ji}^{mn} ($i, j = 1, 2, \dots, N; j \neq i; m, n = p, \tau$) are the interaction coefficients due to unit intensity tractions. They describe the attenuation of the average normal and tangential tractions between interacting cracks. For example Λ_{ji}^{pp} is the attenuation of the normal component p of the stress and $\Lambda_{ji}^{p\tau}$ is the attenuation of the shear component τ of the stress at the site of crack j due to the normal load p of crack i . Furthermore $\Lambda_{ji}^{\tau p}$ is the attenuation of the normal component p of the stress and $\Lambda_{ji}^{\tau\tau}$ is the attenuation of the shear component τ of the stress at the site of crack j due to the shear load τ of crack i . The formulae for calculating $\sigma_{ji}^{mn}(\xi_i)$ are given in Appendix A. Solving the system of linear equations (Eq. 3.4) results in the average tractions $\langle \mathbf{t}_i \rangle$ for all N cracks.

The stress intensity factors at the crack tips can be evaluated from standard expressions,

$$\left. \begin{array}{l} K_I(\pm l/2) \\ K_{II}(\pm l/2) \end{array} \right\} = \frac{1}{\sqrt{\pi l_i/2}} \int_{-l_i/2}^{l_i/2} \sqrt{\frac{l_i/2 \pm \xi}{l_i/2 \mp \xi}} \left\{ \begin{array}{l} p_i(\xi) \\ \tau_i(\xi) \end{array} \right\} d\xi, \quad (3.6)$$

where $l_i/2$ is the half length of crack i .

Finally, the solutions for the average tractions, Eq. (3.4), and the SIFs, Eq. (3.6), can be used to generate approximate expressions for the displacements of the crack faces. For this purpose the actual crack opening deformation along the length of the crack, $D(\xi) = u^+(\xi) - u^-(\xi)$, is approximated by an ellipse that is enriched by quadratic functions,

$$D_n(\xi) = \frac{2l}{E} \left(a_n + b_n \frac{\xi}{l} + c_n \frac{\xi^2}{l^2} \right) \sqrt{1 - 4 \frac{\xi^2}{l^2}} \quad (3.7)$$

and

$$D_\tau(\xi) = \frac{2l}{E} \left(a_\tau + b_\tau \frac{\xi}{l} + c_\tau \frac{\xi^2}{l^2} \right) \sqrt{1 - 4 \frac{\xi^2}{l^2}}. \quad (3.8)$$

The above expressions for the crack face opening displacements, $D_n(\xi)$ and $D_\tau(\xi)$, pertain to crack opening modes I and II, respectively, and to plane stress conditions. E stands for the Young's modulus of the disk's material. The coefficients a_n , b_n and c_n of the quadratic polynomial are chosen to match the mode I stress intensity factor and the average tractions on the crack faces and result as

$$a_n = 2\langle p \rangle - \frac{K_I(l/2) + K_I(-l/2)}{2\sqrt{\pi l/2}} \quad (3.9)$$

$$b_n = \frac{K_I(l/2) - K_I(-l/2)}{\sqrt{\pi l/2}} \quad (3.10)$$

$$c_n = 4 \frac{K_I(l/2) + K_I(-l/2)}{\sqrt{\pi l/2}} - 8\langle p \rangle, \quad (3.11)$$

where $\langle p \rangle$ is the normal component of the average traction. Analogous expressions hold for a_τ , b_τ and c_τ , where $\langle p \rangle$ is replaced by the shear component of the average traction, $\langle \tau \rangle$.

3.1.4 Enhancements of Kachanov's method

Two approaches to extending the range of applicability of Kachanov's approximations to more closely spaced cracks appear feasible, improving the evaluation of the interaction terms in Eq. (3.1) and using more accurate approximations for the face deformations. Note that Kachanov's method is limited to the description of the interaction effects between straight cracks, so that interactions between C- and S-shaped cracks cannot be investigated.

3.1.4.1 Improving the evaluation of the interaction terms

Li et al. (2003) improved the accuracy of the interaction terms in Kachanov's method by decomposing the tractions acting on the cracks into linear and non-linear components. For evaluating the induced stresses at the crack faces of the other cracks they use the traction average and the first (linear) component of the decomposition. Benveniste et al. (1989) proposed the use of Legendre polynomials for describing the distribution of the crack face tractions to better approximate the effects of the crack tip singularities.

3.1.4.2 Using more accurate approximations for the face deformations

Kachanov describes the crack face displacement as an ellipse that is enriched by quadratic functions. In order to improve the accuracy of these approximations for the face deformations D the elliptical shape for the opened crack may be enriched by functions other than quadratic polynomials.

3.2 Finite Element method

The Finite Element method¹⁾ (FEM) originated from the need to solve complex boundary value problems on domains of complex shape involving partial differential equations. One of the essential characteristics of the FE method is the discretization ("meshing") of

¹⁾ For detailed mathematical description see e.g. Rammerstorfer (2003).

a continuous domain into a set of discrete irregularly shaped sub-domains called Finite Elements for which simple local approximations (“shape functions”) of the unknown solution are used. The response of the elements is expressed in terms of the nodal degrees of freedom (DOF) which are coefficients for the shape functions and must be determined to obtain an approximation solution. Each DOF corresponds to a value of an unknown function or functions, describing e.g. the mechanical, the acoustic, the electrostatic, the electromagnetic, the fluid mechanical, or the thermal behavior of the domain, at a set of nodal points that typically are vertices of the Finite Elements. In the case of mechanical continuum elements the DOF of the elements are the displacement components at the nodes. The response of the continuous domain is then considered to be approximated by that of the discrete model obtained by connecting or assembling the collection of all sub-domains or Finite Elements, giving rise to a system of algebraic equations. In this manner approximations for displacements, strains, and stresses of mechanical problems, for which no exact analytical solution are available, can be derived. Compared to other numerical engineering approaches, such as Finite Difference, Finite Volume, and Fourier Transform methods, the main advantage of the FEM is its flexibility with respect to both the problem geometry and the incorporation of different material models.

In general, the FE solutions converge to the exact solution of the problem when the mesh density is increased. The practical limits of accuracy of the FE method are typically posed by computational requirements, which limit the number of degrees of freedom (DOF) and thus the fineness of the mesh.

In the present work the Finite Element program ABAQUS (ABAQUS Inc., Pawtucket, RI) was used to study the face displacements of slit sensilla.

3.2.1 Planar FE models

For the planar FE models of slit sensilla plane stress kinematics were used. As discussed in Chapter 2.2, the cuticle was modeled as an (in-plane) isotropic, linear elastic material with a Poisson number $\nu = 0.3$ and a Young’s modulus of $E_r = 18$ GPa, compare Table 2.3. The length of the largest crack/slit in each of the studied arrays is l_0 . Unless stated otherwise the Finite Element models used for studying cracks/slits were square regions of

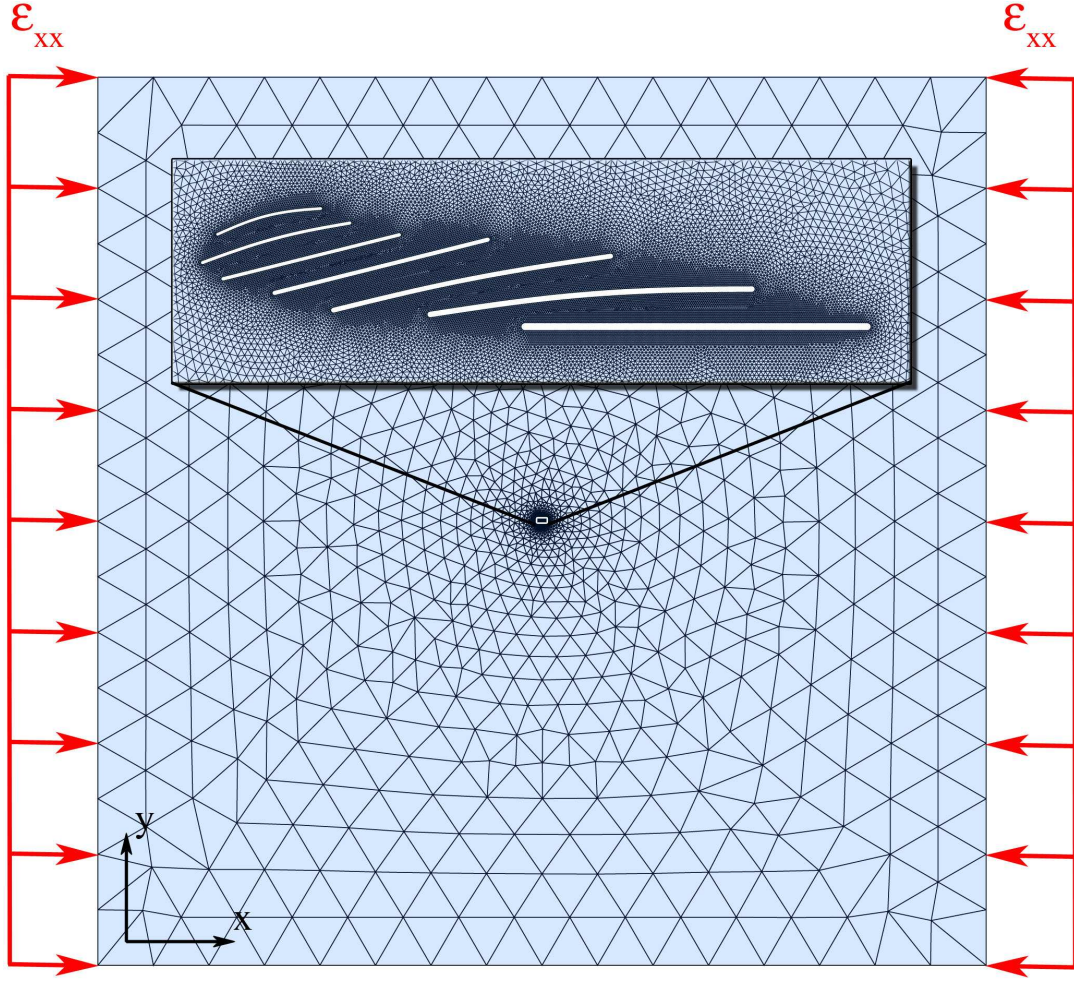


FIGURE 3.5: Boundary conditions used for planar 2D models of slit sensilla. The disks of size $400 l_0 \times 400 l_0$ were loaded by uniform far-field strains in the x -direction and the edges at $y=\text{const}$ were left free to deform, resulting in a uni-axial stress state and a biaxial strain state.

size $400 l_0 \times 400 l_0$ and thickness $t_r = 0.1 l_0$. At the centers of the models the cracks/slits were located, which accordingly closely approximate cracks or slits in infinite disks. Note that a homogeneous isotropic in-plane material behavior is an approximation. In the strict sense both a varying thickness of the cuticle and the change in orientation of the laminae not parallel to the surface close to the slits would have to be modeled.

Loading was applied in the form of prescribed uniform far-field uni-axial compressive (or, for the investigation of cracks tensile) in-plane strains acting in the x -direction. In the

y -direction the disks were left free to deform (see Fig. 3.5), resulting in an uni-axial overall stress state and, due to the Poisson effect, in a biaxial overall strain state. Note that the thickness of such models does not influence the results when the applied strains or stresses are given. Applied forces, however, must be scaled by a factor t/t_r , where t is the actual thickness of the disk.

For studying slit arrangements by planar FE models the membranes and the fluid contained in arachnid sensory slits were assumed to have negligible influence on their quasi-static deformation behavior¹⁾. Simulations were limited to the small strain regime, with maximum local strains of 1.2×10^{-4} ($= 120 \mu\epsilon$), so that all analyses are linear. Accordingly, the superposition principle can be used to evaluate the responses to multi-axial loads from uni-axial load cases. The models do not have an intrinsic absolute length scale, which means that the results can be scaled to any slit size, including that actually found in nature.

Unless stated otherwise the relative face displacements are evaluated as the change in distance (D) between two opposite points at the faces of a slit in the undeformed state, $D = w_0 - w$ (Fig. 3.6). For the configurations studied here, the differences between D and the change of the width of the slit, $\tilde{D} = w_0 - \tilde{w}$ (as defined in Fig. 3.6), evaluated at the center of the slits (D_c) or at the positions of the dendrites (D_d), remain small at $(D - \tilde{D})/\tilde{D} \lesssim 8.2 \times 10^{-3}$. This is due to the fact that the slits were mostly compressed rather than sheared under the in-plane loads considered. Accordingly there is no noticeable difference between plotting our diagrams in terms of \tilde{D} or D .

3.2.1.1 Planar FE models for assessing Kachanov's method

When the FE method is used for modeling problems from linear elastic fracture mechanics (LEFM) a difficulty arises. The polynomial interpolation functions used for standard Finite Elements cannot represent the singular crack tip stress and the strain fields predicted by LEFM. Many researchers investigated this problem and developed special finite element formulations that incorporate singular interpolation functions (e.g. Byskov (1970); Tracey (1971); Tong et al. (1973); Atluri et al. (1974); Benzley (1974); Papaioannou et al. (1974)). Such elements are, however, not accessible in most commercial FE programs. In the mid

¹⁾ The associated effects were studied in detail, however, with three-dimensional models, see Chapter 5.1.

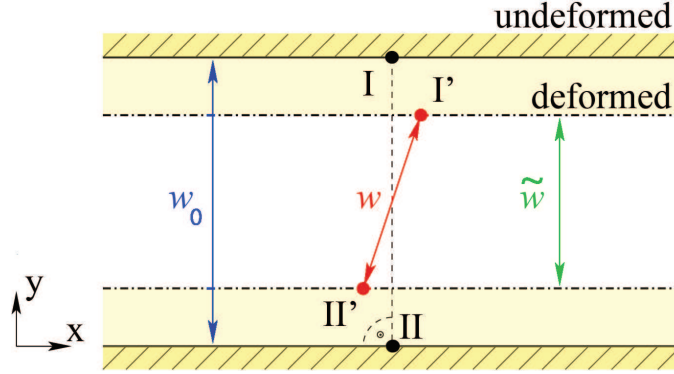


FIGURE 3.6: Evaluation of slit face displacements. Either the change in distance between two opposite points I and II, $D = w_0 - w$, or the change in slit width $\tilde{D} = w_0 - \tilde{w}$ can be evaluated. Undeformed states I and II; deformed states I' and II'.

seventies Henshell and Shaw (1975) and Barsoum (1977) independently developed the so called quarter point elements. They showed that the proper crack tip opening displacement, stress, and strain field around a crack tip can be obtained from standard quadratic isoparametric quadrilateral Finite Elements. When one element edge is collapsed and the midside nodes on the neighboring edges are moved to the quarter points (Fig. 3.7) a $1/\sqrt{r}$ singularity is introduced into the mapping between the element's parametric coordinate space and Cartesian space.

In the FE models for assessing Kachanov's method tensile reference strains $\varepsilon_{a,r} = -5.56 \times 10^{-5}$ ($= -55.6 \mu\varepsilon$) were applied at the models' boundaries in the x -direction that correspond to an applied tensile reference far field stress of $\sigma_{a,r} = 1$ MPa. The results obtained

TABLE 3.1: Difference in mid-crack face opening displacement ($\Delta D_c = (D_{c,qp} - D_c)/D_{c,qp}$ in percent) in a stack of five cracks ($S/l_0 = 0.125$) between a model with a two way biased mesh seed along the crack faces (D_c ; 40 nodes with a bias ratio of 8) and a similar model but incorporating quarterpoint elements at the crack tips ($D_{c,qp}$).

	crack1 and 5	2 and 4	3
D_c/D_{cc}	0.5875	0.4536	0.0911
$D_{c,qp}/D_{cc}$	0.5871	0.4366	0.0925
ΔD_c	-0.07 %	-3.9 %	1.5 %

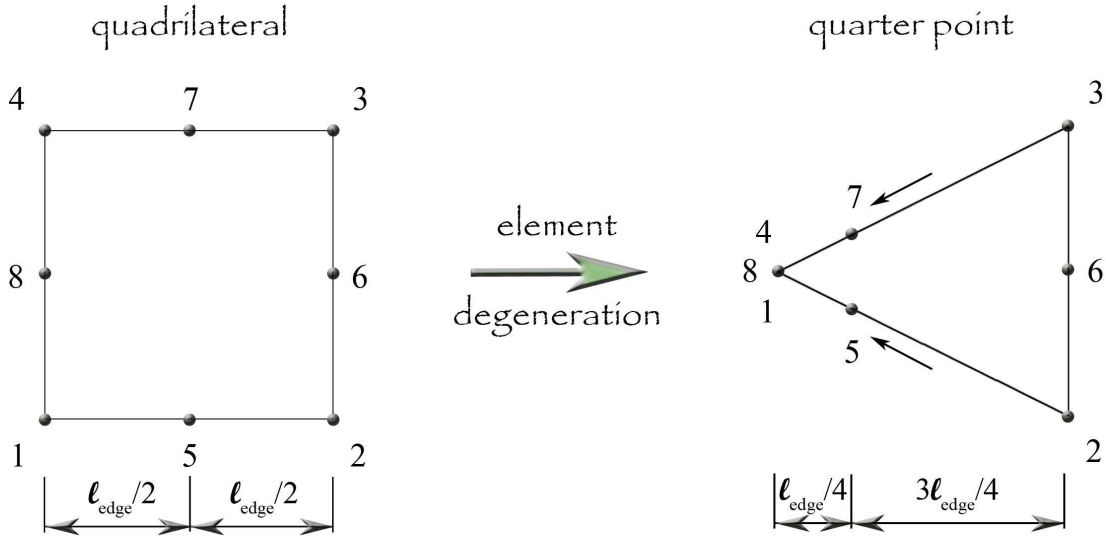


FIGURE 3.7: A triangular quarter point element is generated by collapsing an eight node quadrilateral element after Barsoum (1977).

for a single crack can be compared to the exact analytical solution of the mid-crack face opening displacement of a single isolated crack D_{cc} (Hahn, 1976).

The models were meshed with 6-noded triangular plane stress elements. In a convergence study, performed at lateral spacings of $S/l_0 = 0.125$ and $S/l_0 = 0.5$ (Fig. 3.8), we increased the number of nodes along the crack faces in a two way biased mesh (bias ratio 8) and added quarter point elements at the crack tips. In Figure 3.9 the results obtained for a stack of five cracks at lateral spacings of $S/l_0 = 0.125$, which is more sensitive to a change in element size and element number, are shown. When increasing the number of elements along the crack faces from 40 to 120 only a small difference in mid-crack opening displacement, D_c , is noticeable, i.e., even the coarsest of the meshes employed is fully satisfactory. The influence of the quarter point elements on the mid-crack face deformations also remains small (Table 3.1).

It may be noted that, although according to electro-physiological investigations deformation of the slits normal to their long axes represents the adequate stimulus (Barth, 1972a,b), within linear theory the results obtained for crack opening can be directly transformed to describe compressive loading of the slits.

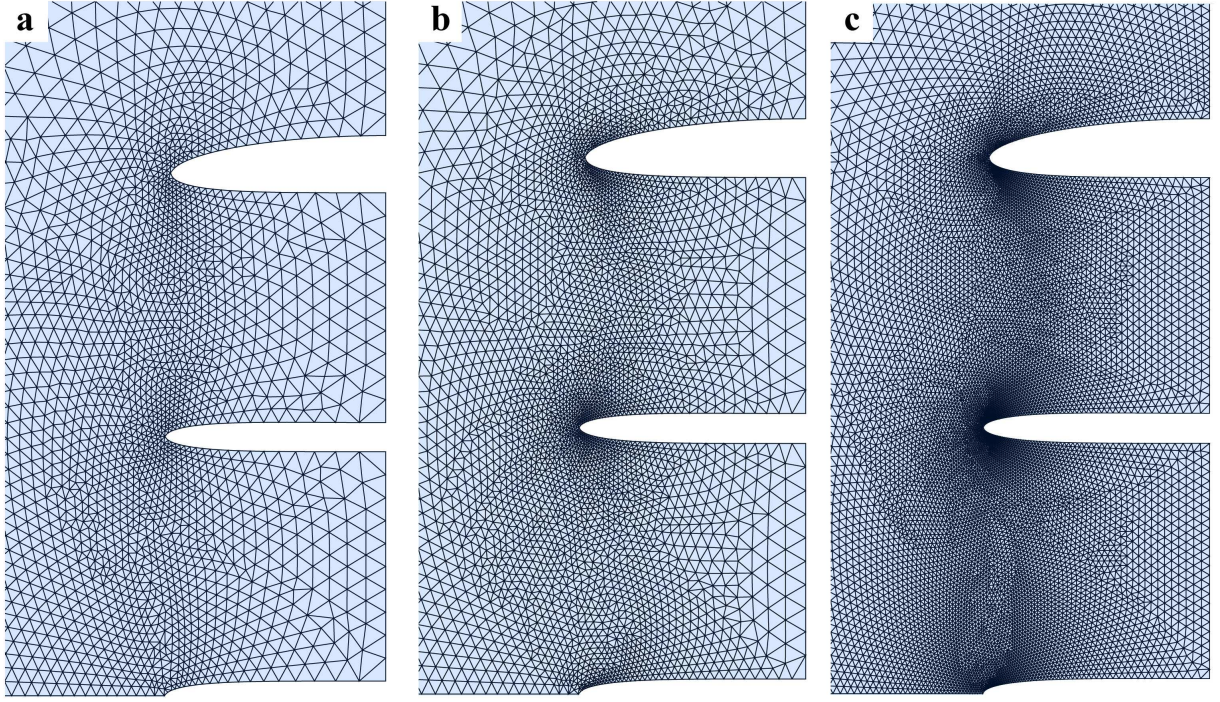


FIGURE 3.8: Deformed FE quarter models (two symmetry axes) of five non-staggered cracks spaced at a half of their length ($S = 0.5l_0$). **a** A two-way biased mesh with 40 nodes, **b** with 60 nodes, and **c** with 80 nodes and a bias ratio of 8 along the crack faces with plane stress elements. Quarter-point elements were employed in the mesh depicted in **b** to account for the stress singularities at the crack tips. The deformations are scaled up by a factor of 2.1×10^3 .

3.2.1.2 Planar FE models for studying slit sensilla

Unless stated otherwise slits are of “capped rectangular” shape, i.e., a rectangular central region is closed off by semicircular caps with diameters that equal the width of the slit. All models were meshed with 6-noded triangular plane stress elements. Note that the constant thickness of the elements is a good assumption for the far-field of the models but not necessarily for the vicinity of the slits, where the cuticle tends to have a different thickness. The meshes were strongly refined in the vicinity of the slits (Fig. 3.5) and a convergence study was carried out in a stack of five similar slits at a lateral distance $S/l_0 = 0.02$ to ensure a sufficiently fine discretization. In this study the results for stacks of five slits are insensitive to a change in element length that was held constant along the

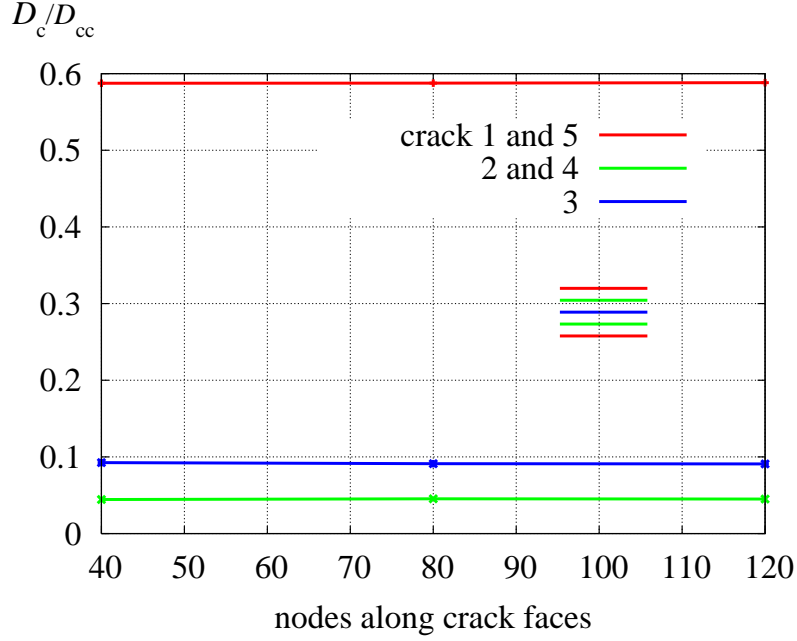


FIGURE 3.9: Results of a convergence study on a stack of five cracks at lateral spacings of $S/l_0 = 0.125$ in terms of relative mid-crack face opening distance D_c/D_{cc} . The number of nodes along the crack faces was increased and the bias ratio of the two way biased mesh was held constant at 8.

slits faces between $\ell_{\text{edge}}/l_0 = 0.008$ and 0.001 (Fig. 3.10). Accordingly, coarse meshes with edge lengths of the elements along the slits faces of $\ell_{\text{edge}}/l_0 = 0.004$ were chosen to achieve less CPU intense results.

In view of the models' scaling properties the results on slit face displacements are normalized with respect to a reference configuration. This takes the form of a single slit of aspect ratio $l_0/w_0 = 100$ situated at the center of a square disk subjected to a uni-axial compressive far-field strain $\varepsilon_{a,r} = 2.5 \times 10^{-5}$ ($= 25 \mu\varepsilon$) which acts normal to the slit faces. The corresponding compressive far-field stress is $\sigma_{a,r} = 4.5 \times 10^5$ Pa. The above far-field strain is well within the range of physiological values (Blickhan and Barth, 1985; Brüssel, 1987). For this configuration the slit face displacements at the slits' center assume a value of $D_{sc} = 5.034 \times 10^{-5} l_0$ under the above conditions. Therefore, an actual slit of length $l_0 = 100 \mu m$ is compressed by 5.034 nm. Taking the shielding effects of the slits in lyriform

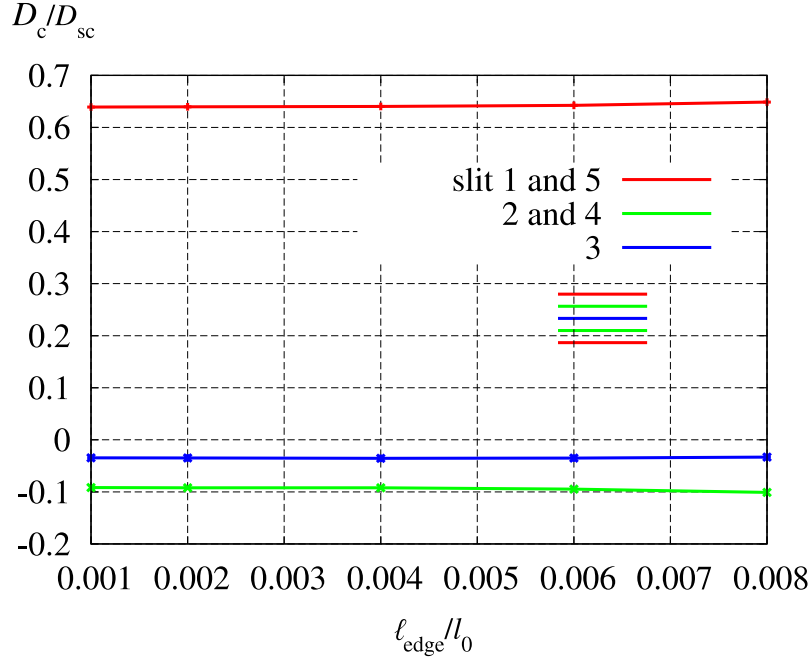


FIGURE 3.10: Results of a convergence study of the model of a stack of five slits at a lateral spacing of $S/l_0 = 0.02$ in terms of slit face displacements (D). The edge lengths of the elements along the slits faces ℓ_{edge}/l_0 were decreased from 0.008 to 0.001.

organs into account this is in good agreement with the measured slit deformation of about 3 nm for the largest slit in lyriform organ HS8 on the tibia of the bird spider *Aphonopelma* (Blickhan, 1983). For convenience, the above parameters describing the reference slit under uni-axial deformation in normal direction are also listed in Table B.1 in Appendix B. In the models for studying the directional responses of the organs the boundary conditions (see Fig. 3.5) were held constant and the slit arrays were rotated accordingly.

Additional models for studying boundary effects took the form of circular disks with diameter $8.66l_0$, thickness $0.2l_0$, aspect ratio $l_0/w_0 = 15$, and lateral spacing between the slits $S/l_0 = 0.33$ (Fig. 3.11a). They correspond to the conditions used in the experimental study of Barth et al. (1984). Among others, loads oriented parallel to the slits were introduced into the disks over an angle of approximately 70° (Fig. 3.11b). Since we used square models within our study we loaded a square disk with an edge length similar to the diameter of the circular disks by distributed loads acting on subregions of the straight

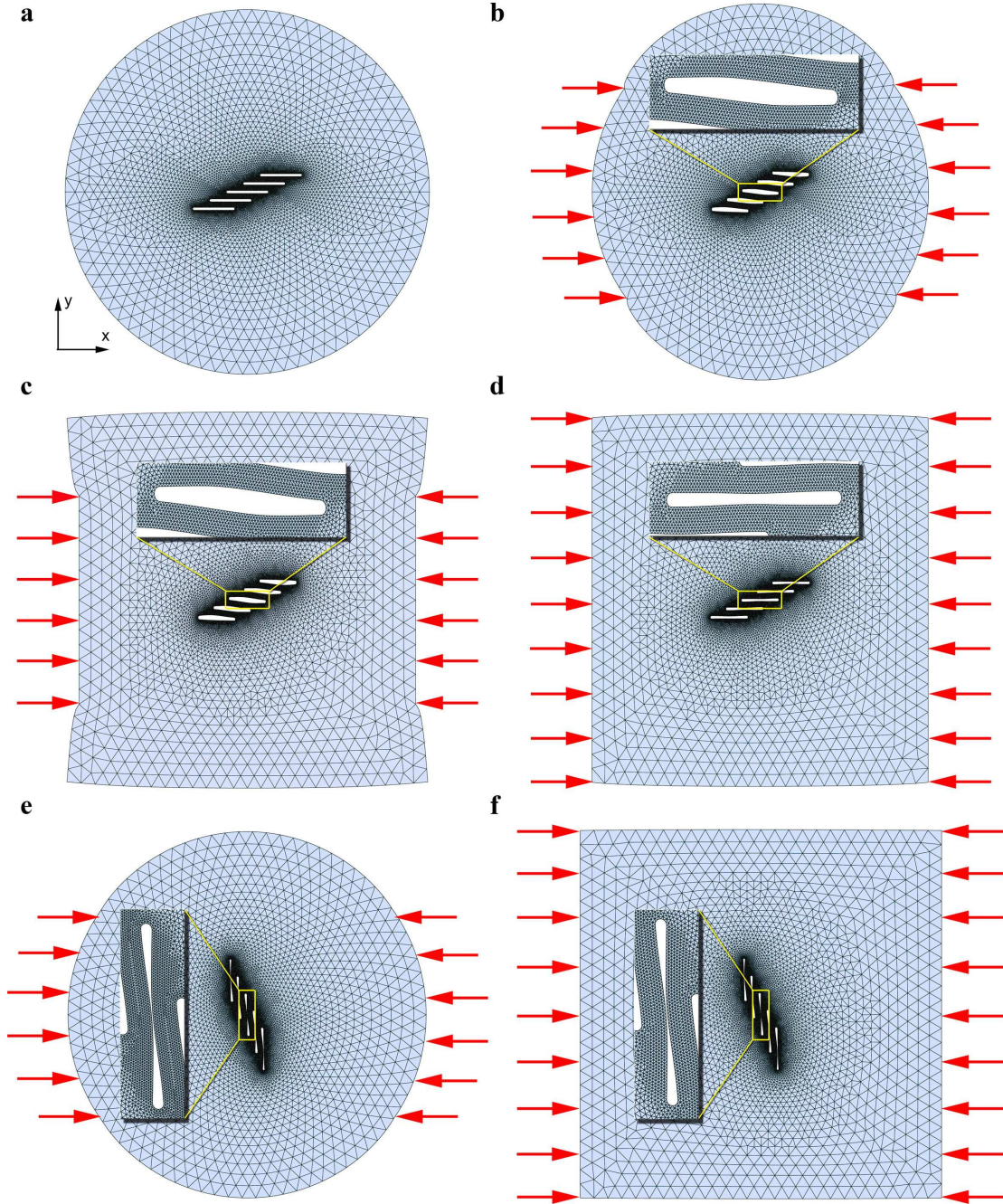


FIGURE 3.11: Study of the boundary effects on the deformation of the slits in an oblique bar formation with $l_0/w_0 = 15$, $S/l_0 = 0.05$, and $\lambda/l_0 = 0.4$. **a** Undeformed and **b** deformed FE models of a circular disk with geometry and loading closely approaching the ones used in the experimental study of (Barth et al., 1984). **c** Slits in a square disk of similar size (diameters in a, b, e equal side lengths in c, d, f) to the circular disk in a, open up under loading conditions analogous to the one used in b. **d** Square disk loaded by homogeneous strains at the edges shows deformation of the slits. **e** Deformed circular and **f** square disks subjected to loading normal to the slits show similar slit deformations. The displacements are scaled up by factors of 2×10^3 (b to d) and 2×10^2 (e and f), respectively.

edges that correspond to the 70° angle range in the circular disks (Fig. 3.11c). Under these loading conditions both the experiments of Barth et al. (1984) and the present FE analysis show that the slits in an oblique bar formation loaded at $\Phi = 0^\circ$ open up (Figs. b and c). In contrast, square models of the same size (Fig. 3.11c) subjected to uniformly distributed uni-axial strains along the edges predict that the slits are compressed for a load angle of $\Phi = 0^\circ$ (Fig. 3.11d). Evidently, for such “longitudinal” loads there is a marked effect of the boundary conditions on the slit face displacements. For normal loads ($\Phi = 90^\circ$), which are biologically more relevant, however, the difference in the slit face displacements obtained for the above types of boundary conditions amounts to only 3%. The boundary conditions corresponding to actual spider sensory organs are unknown. They can, however, be approximated by three-dimensional shell models, e.g. of segments of spider legs, and incorporated into local shell or plane stress models.

3.2.2 3D FE models

In the present thesis we employed two kinds of three-dimensional FE models: (i) three-dimensional structural models to model the slits’ morphology (shape and stiffness of the membranes and filling of the slits) and (ii) three-dimensional shell models that explore the effects of the three-dimensional shape of the cuticle at the site of the organs on the slit deformations.

In the Finite Element models the cuticle was treated as a transversely isotropic elastic material with the effective material parameters given in Table 2.3. Unless stated otherwise the deformations were evaluated in the mid-plane at the centers of the slits and all analyses were performed with geometrically linear models.

3.2.2.1 3D FE structural models

Unless stated otherwise quarter models of the slit arrangements were employed, which make use of the mirror symmetries of the arrangements with respect to the xz - and yz -planes (Fig. 3.12). Therefore, these models are restricted to far-field loads acting normally or tangentially to the slits. All 3D structural models for studying the influence of the

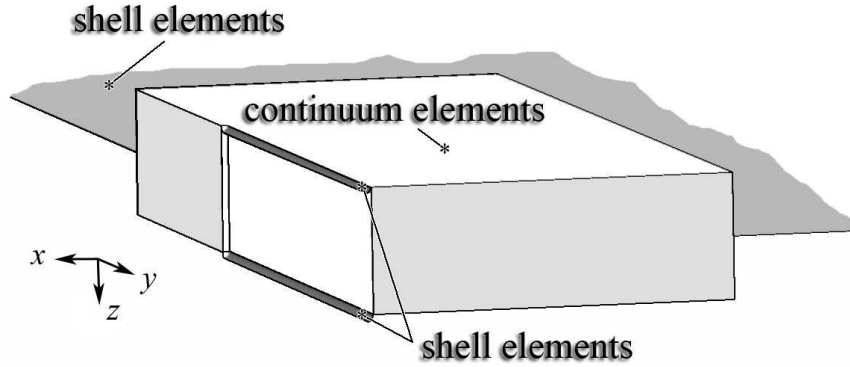


FIGURE 3.12: Three dimensional Finite Element quarter model of a single slit making use of its mirror symmetry. Continuum elements were used in the vicinity of the slit embedded in an outer region meshed with shell elements. Both membranes were meshed with shell elements.

cross sections of the membranes and of the fluid present inside the slits on the slit face deformation were square disks of size $40\text{ }\mu\text{m} \times 40\text{ }\mu\text{m}$ at the centers of which single slits of length $l = 100\text{ }\mu\text{m}$ and width $b = 1\text{ }\mu\text{m}$ were located as in most of the planar FE models introduced in Chapter 3.2.1.2. The disks were $10\text{ }\mu\text{m}$ thick, which corresponds to the thickness of the exocuticle of the tibiae of *C. salei*. Both the outer and inner slit membranes were assumed to be $0.25\text{ }\mu\text{m}$ thick and to show a linear elastic isotropic material behavior with a Young's modulus of 1.5 MPa and a Poisson's ratio of 0.3 . The same material behavior was used for the coupling cylinder with diameter $0.3\text{ }\mu\text{m}$, length $0.25\text{ }\mu\text{m}$, and thickness $0.125\text{ }\mu\text{m}$ with a ring at the inner rim of inner diameter $0.24\text{ }\mu\text{m}$ necessary to fix the dendrite (geometrical proportions as in Fig. 3.13a). The coupling cylinder was positioned at the center of the outer membranes according to fine structural studies of the long single slit on the tarsus of *C. salei* (Barth, 1971).

In order to study the influence of the shape of the outer membrane on the deformation of the coupling cylinders of single isolated slits membranes of low curvature (circular sector with radius $0.707\text{ }\mu\text{m}$ and height $0.3\text{ }\mu\text{m}$), of semi-circular cross section, and with a dimple of diameter $0.8\text{ }\mu\text{m}$ (Fig. 3.13b) and height $0.1\text{ }\mu\text{m}$ in a semi-circular cross section were used (Fig. 3.14a). These models were suggested by SEM images of organ HS9 (Barth and Stagl, 1976) and by images of semi-thin slices of the organ HS8 (Fig. 3.13c) both positioned on the tibia of *C. salei*. Because the mechanical properties of the slits' contents are unknown both

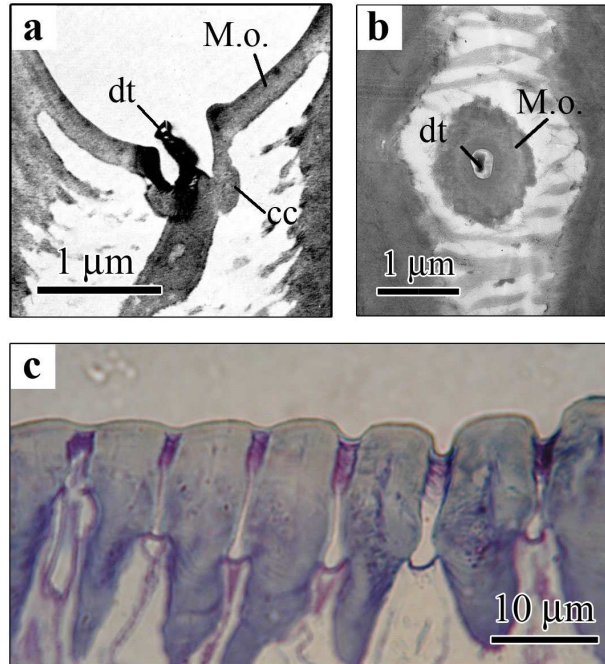


FIGURE 3.13: **a** Cross section of the long single slit on the tarsus of *C. salei* at the location of the dendrite (Barth, 1971). **b** Slit of lyriform organ HS8 on the tibia of *C. salei* cut in a plane parallel to the surface showing the additional dimple in the outer membrane at the location of the dendrite (Müllan, 2005). **c** Semi-thin slice of lyriform organ HS8 on the tibia of *C. salei* cut laterally to the longitudinal axes of the slits close to the location of the dendrite of the shortest slit in the arrangement (Müllan, 2005). cc coupling cylinder; dt dendritic tip; M.o. outer membrane.

highly compressible (gas-like) and weakly compressible (liquid-like; Bulk modulus 2.2 GPa) behaviors were modeled with hydrostatic fluid elements. In these models the analyses were geometrically nonlinear and the results were compared to the results of the deformations of the outer membranes in the organ HS8 of *C. salei* measured interferometrically under biologically relevant loads. In the models considering the slits' contents membranes of semi-circular cross sections were incorporated without taking the coupling cylinders into account (Fig. 3.15). Both membranes were modeled as impermeable, i.e. the volumes of the slits are closed and deformation of the slit faces increases the pressure inside the slits.

Under compressive far-field loads acting normally to the longitudinal axis of the slits the effect of the stiffness of the membranes on the mid-length deformation of the slit was studied in square models of stacks of five equal parallel capped rectangular slits with length

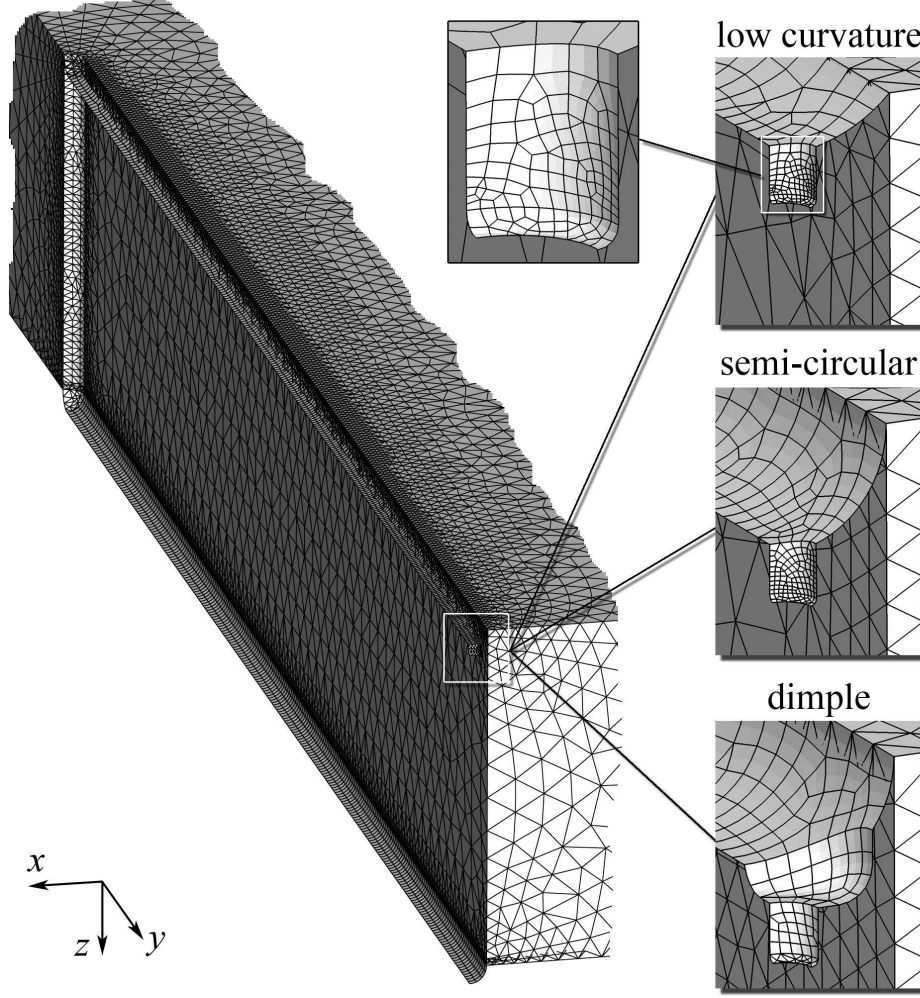


FIGURE 3.14: Detail of a model for studying different cross sections of the outer membrane, i.e. low curvature, semi-circular cross section, and a dimple in a semi-circular cross section, of a single isolated slit.

$l = 100 \mu\text{m}$, width $b = 1 \mu\text{m}$, and lateral spacings of $S/l = 0.02$ (Fig. 3.16). Semi-circular linear elastic isotropic membranes of thickness $0.25 \mu\text{m}$ were assumed and the coupling cylinders were not considered. The slit face deformations were normalized with respect to a reference slit face displacement $D_{\text{sc}} = 5.034 \text{ nm}$, which pertains to the center of a single isolated slit of length $l = 100 \mu\text{m}$ and width $b = 1 \mu\text{m}$ without outer and inner membrane and subjected to far-field strains of $\varepsilon_a = 2.5 \times 10^{-5}$ in analogy to the planar studies and Appendix B.

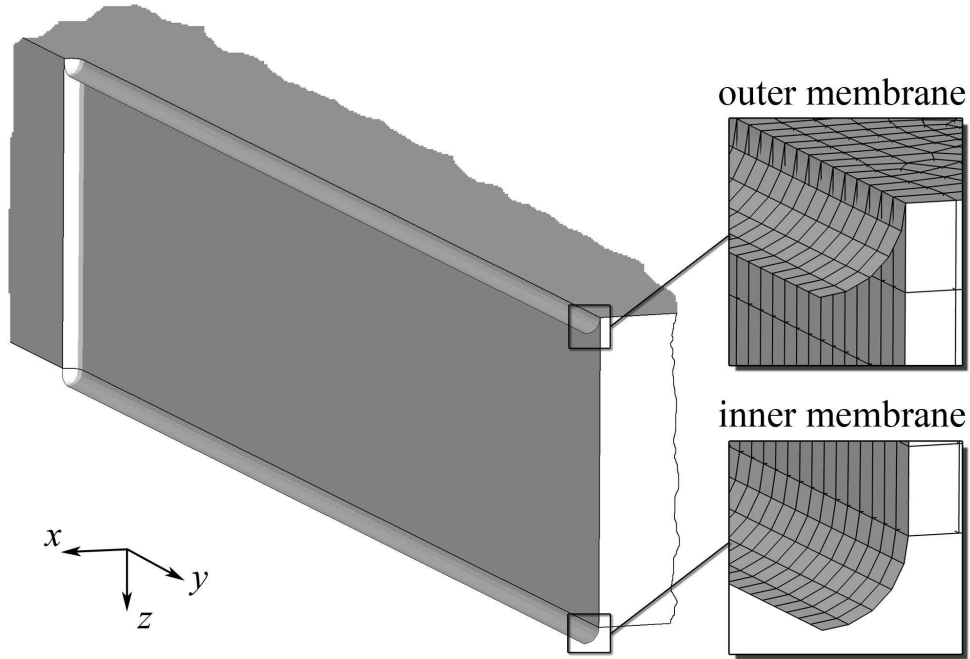


FIGURE 3.15: Detail of a quarter model of a single slit used to study the influence of the slit filling.

In all 3D FE models described in the present section the exocuticle in the vicinity of the slits was discretized by continuum elements that were embedded in a square region meshed with 6-noded triangular shell elements using shell to solid element coupling (Fig. 3.12). The models for investigating the influence of different cross sections of the membranes on the deformation of the coupling cylinder (models of single slits) and the influence of the stiffness of the membranes on the mid-length slit deformation (models of stacks of five similar parallel slits) were meshed with 10-noded tetrahedral continuum elements in the vicinity of the slits. The membranes were discretized by combinations of 8-noded rectangular and 6-noded triangular shell elements. In the models accounting for the fluid present inside the slits elements with linear interpolation functions were used at the inner faces of the slits and for the elements of the membranes in order to ensure compatibility with the finite elements used for hydrostatic modeling of the fluid. Therefore the models of the disks were meshed with 8-noded brick continuum elements close to the slits and the membranes were meshed with 4-noded rectangular shell elements.

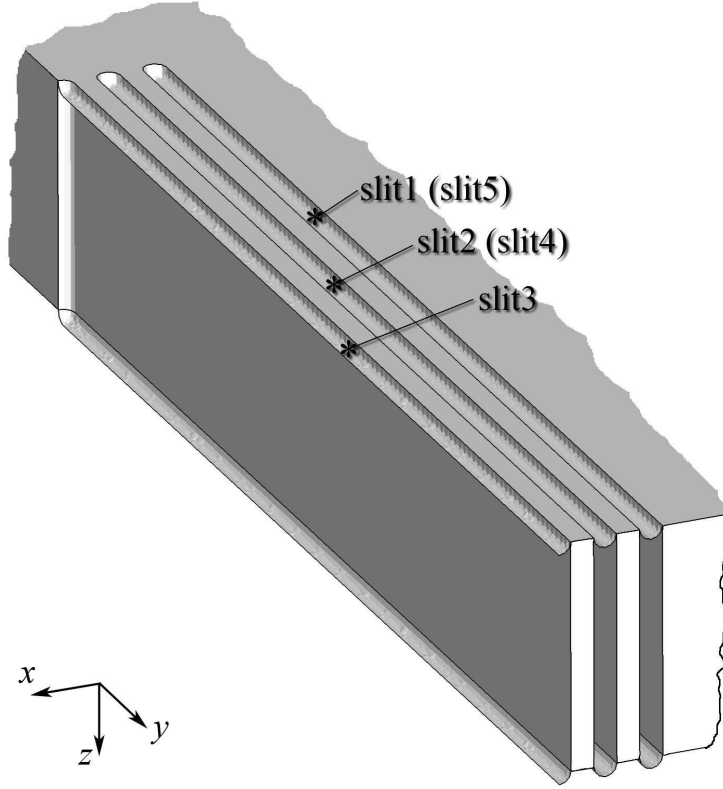


FIGURE 3.16: Detail of a model of a quarter of a disk for studying the influence of the stiffness of the membranes on the slit deformation in a stack of five similar parallel slits at a neighboring distance of $S = 0.02 l_0$.

A convergence study was performed for the continuum model of a single slit filled with fluid using linear elements. The results presented in Table 3.2 show that the solution of this problem does not fully converge even when a fine mesh (element edge length along the slit faces of $\ell_{\text{edge}}/l = 0.002$; element edge length over the thickness of the cuticle of $\ell_{\text{edge}}/l = 0.05$) is used. To obtain results in reasonable time we used meshes with an element edge length along the slit faces of $\ell_{\text{edge}}/l = 0.004$ and an element edge length over the thickness of the cuticle of $\ell_{\text{edge}}/l = 0.05$ (D_c^2 in Table 3.2).

All models were loaded by a prescribed compressive far-field strain of $\varepsilon_a = 2.5 \times 10^{-5}$ ($=25 \mu\varepsilon$) acting on the edges parallel to the y -direction as described in Chapter 3.2.1.2. This strain value is well within the range of physiological values (Blickhan and Barth, 1985; Brüssel, 1987). The outer edges parallel to the x -direction were allowed to deform freely

TABLE 3.2: Difference in mid-slit face displacement ($\Delta D_c^i = (D_c^{i+1} - D_c^3)/D_c^3$ in percent) and in mid-slit out-of-plane deformation of the outer membrane ($\Delta u_z^i = (u_z^{i+1} - u_z^3)/u_z^3$ in percent) in a single slit filled with fluid between a model with a coarse mesh D_c^1 (element edge length along the slit faces of $\ell_{\text{edge}}/l = 0.004$; element edge length in thickness (z -)direction of the cuticle of $\ell_{\text{edge}}/l = 0.1$), a fine mesh D_c^3 (element edge length along the slit faces of $\ell_{\text{edge}}/l = 0.002$; element edge length in thickness (z -)direction of the cuticle of $\ell_{\text{edge}}/l = 0.05$), and a mesh with intermediate fineness D_c^2 (element edge length along the slit faces of $\ell_{\text{edge}}/l = 0.004$; element edge length in thickness (z -)direction of the cuticle of $\ell_{\text{edge}}/l = 0.05$).

D_c^1	D_c^2	D_c^3	ΔD_c^1	ΔD_c^2
0.8169 nm	0.884 nm	0.926 nm	-11.8%	-4.5%
u_z^1	u_z^2	u_z^3	Δu_z^1	Δu_z^2
3.823 nm	3.811 nm	3.8453 nm	-0.6%	-0.89%

in the in-plane and out-of-plane directions (coordinates as in Fig. 3.12). Since the amount of slit deformation remains small contact of the membranes and the inner faces of the slits did not have to be considered.

3.2.2.2 3D FE shell models

For studying the relevance of the three-dimensional shapes of the cuticular regions surrounding the slits (global and local curvature effects) on the slit face displacements single slits were incorporated at the centers of planar square disks of size 10 mm \times 10 mm into different local geometrical features in the form of bumps and ridges (Figs. 3.17b and c) that are frequently seen in SEM images (Figs. 3.18a and b). Analogous studies were carried out on slits parallel to the axis of cylinders of diameter 5 mm (Fig. 3.19b and c). The thickness of the models being 10 μ m in both cases. From SEM images of lyriform organ HS8 of the spider *C. salei*, that was fractured along the longest slit of the organ (Fig. 3.20a and b), we know that this sensillum is situated on a ridge that has a height of approximately 45 μ m and a width of 160 μ m (Müllan, 2005). Accordingly, the bumps in the models took the form of spherical caps of radius 100 μ m (Figs. 3.17b and Fig. 3.19b), the cross sections of the ridges were circular segments of radius 100 μ m (Figs. 3.17c), both of height 45 μ m, and in the cylindrical models ridges of similar geometry were arranged to run circumferentially around the cylinder, forming stiffening rings (Fig. 3.19c). For studying the principal effects

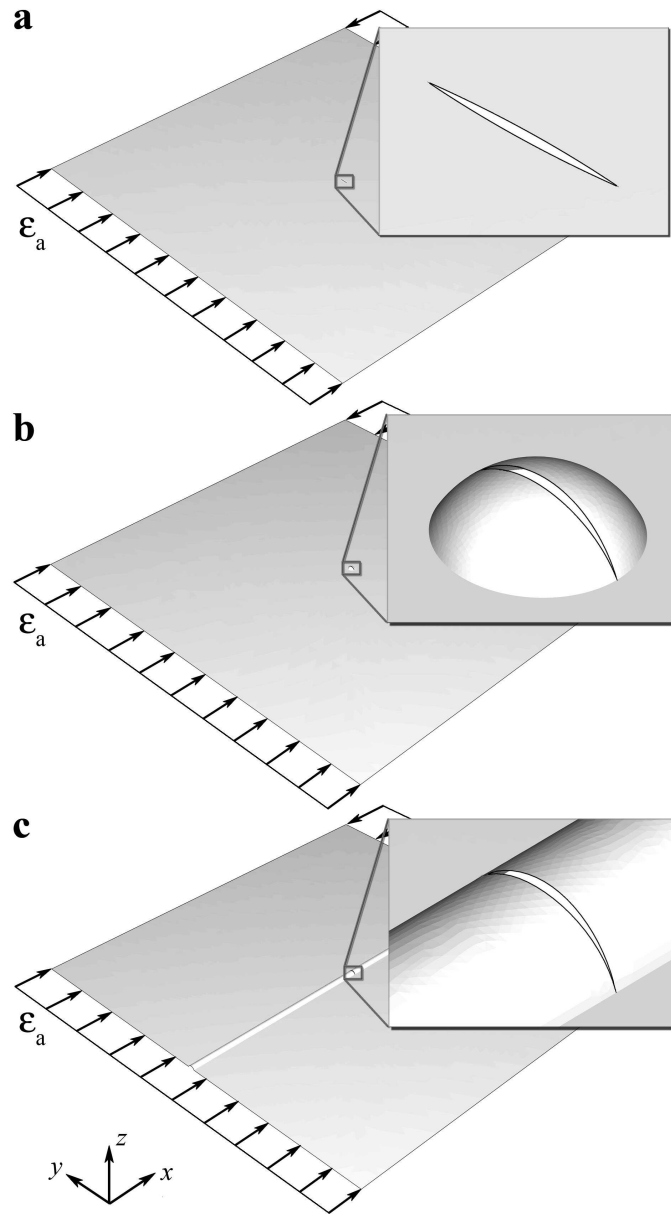


FIGURE 3.17: Single isolated slits modeled in **a** a flat disc, **b** a spherical bump, and **c** a ridge-like structure.

of three-dimensional shapes of the cuticle at the site of the organs on the slit deformation bumps and rings were located in the middle of the cylinders. The latter configuration is similar to the stiffening ring on the trochanter of *C. salei* where the organ HS2 is located (Fig. 3.18b). To account for the effect of the slit length we modeled single slits of length

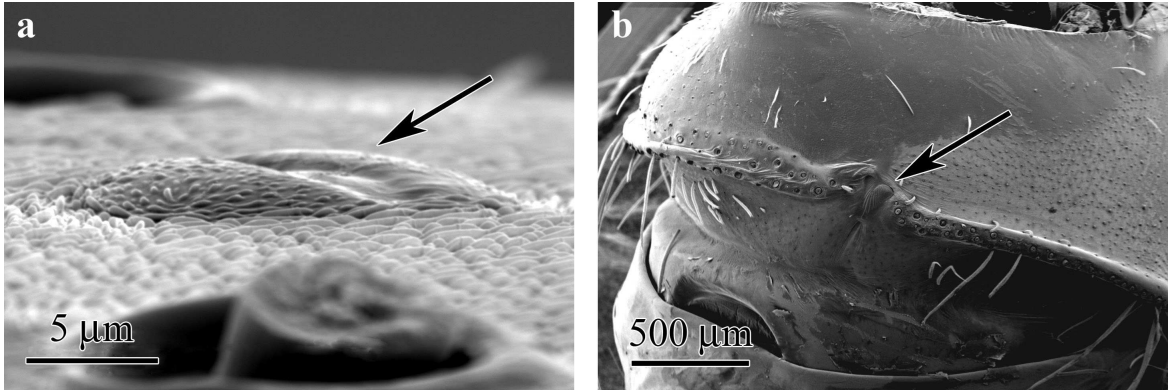


FIGURE 3.18: SEM images of **a** a single slit positioned on a spherical bump on the coxa and **b** lyriform organ HS2 located on a stiffening ring on the trochanter of *C. salei* (Müllan, 2005). The arrows point to the location of the sensilla.

$l = 186 \mu\text{m}$, corresponding to the arc length of the openings (projected length $160 \mu\text{m}$, see Fig. 3.20c) in the spherical bumps, the ridges, and the rings, in smooth planar disks or smooth cylinders. The ratio of slit length vs. diameter of the modeled cylinder is 0.037 which is smaller than the value of approximately 0.09 found for the longest slit of the organ HS8 of *C. salei*. Accordingly, higher slit face deformations are expected in the spider leg for slits located in bumps or rings under similar boundary conditions.

The planar disks were loaded by compressive far-field strains of $\varepsilon_a = 2.5 \times 10^{-5}$ ($=25 \mu\varepsilon$) acting on the edges parallel to the y -direction and the edges parallel to the x -direction were allowed to deform freely in y - and z -direction (Fig 3.17). In addition all edges were allowed to rotate freely. The half models of the cylinders were free to deform in the axial direction and symmetry boundary conditions (no displacements in z -direction and no rotations about the x - and y -axes) were applied in the section plane (xy). In this plane a tensile far-field displacement of $100 \mu\text{m}$ was applied in the x -direction (Fig 3.19) so that the maximum strains in the models are $\varepsilon = 5 \times 10^{-3}$ and all analyses are linear. This load case results in an ovalization of the cylinder and therefore in bending moments at the location of the slits in contrast to the in-plane uni-axial stress loading of planar discs.

Additional models were used to compare interaction effects between the slits modeled in disks under in-plane loads and bending moments. The models were smooth planar disks

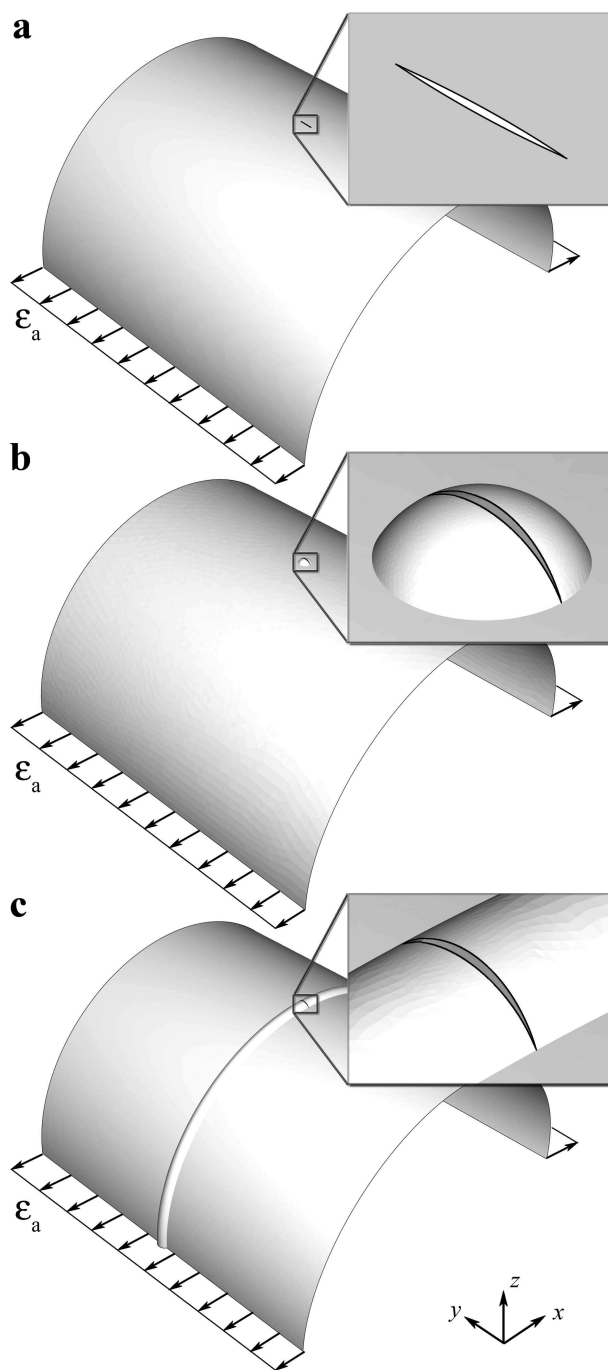


FIGURE 3.19: Model of a single slit incorporated in cylinders. **a** Single slit in a smooth cylinder, **b** single slit in a spherical bump, and **c** single slit in a ring-like structure.

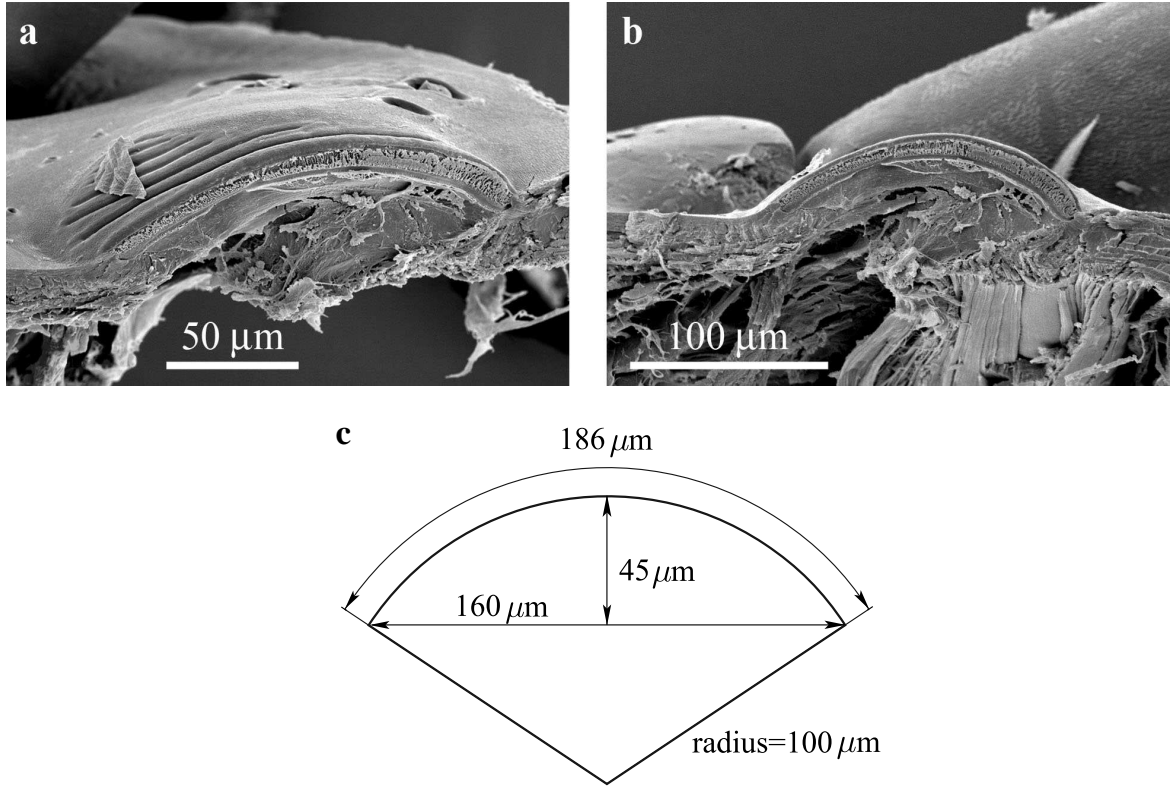


FIGURE 3.20: SEM images of lyriform organ HS8 on the posterior side of the tibia of the spider *C. salei* in isometric (a) and frontal view (b) (Müllan, 2005). c Cross section of the models of spherical bumps and ridges.

and disks incorporating a diagonal ridge of circular cross section with a radius of 100 μm and a height of 45 μm. The size of the models was 4 mm × 4 mm and their thickness 10 μm (Fig. 3.21b). At the center of the disk a slit formation based on lyriform organ HS8 of *C. salei* (projected length 160 μm, see Fig. 3.20c), oriented at an angle of -5° relative to the x -axis (similar to the organ's orientation at the distal end of the tibia of the walking leg) (Figs. 3.21a and b), was positioned.

The latter models were loaded as described before by compressive far-field strains of $\varepsilon_a = 2.5 \times 10^{-5}$ ($=25 \mu\varepsilon$) acting in the x -direction. In addition bending moments M_y were introduced into the disks as rotations of the edges parallel to the y -axis of 0.001 radians ($= 0.057^\circ$) about the y -axis of the disks (Fig. 3.21b) so that the maximum local strains in the models are 5×10^{-5} .

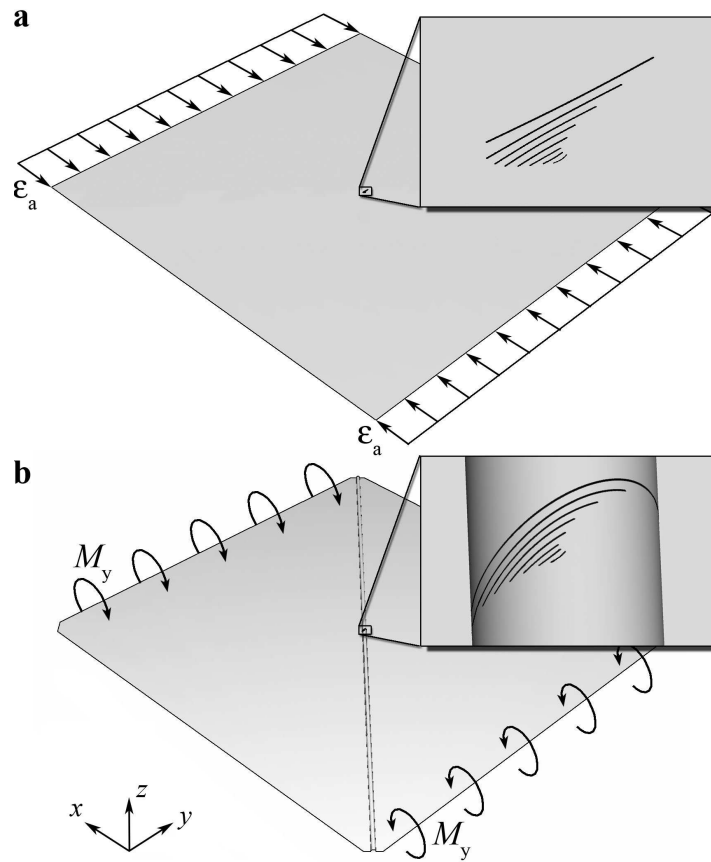


FIGURE 3.21: Arrangement of slits based on lyriform organ HS8 of *C. salei* modeled in **a** a planar disks under planar uni-axial loads and **b** a planar plate under bending loads.

For comparison we performed simulations of similar setups with a linear elastic isotropic material using a Young's modulus of 18 GPa and a Poisson number of 0.3. All shell models were meshed with 6-noded triangular shell elements and the analyses were materially linear and geometrically nonlinear. The element edge length along the slit faces was chosen in accordance to the convergence study presented in Fig. 3.10 as $\ell_{\text{edge}}/l_0 = 0.004$.

Chapter 4

Planar models

4.1 Results

4.1.1 Analytical models using Kachanov's method

4.1.1.1 Comparisons between analytical and FE models

Because of the approximations involved in Kachanov's method, the degree of accuracy of the predicted crack opening distances must be known to assess their usefulness in the present context. Gorbatiikh and Kachanov (2000) examined the accuracy of the predictions for the SIFs and the stress fields for three specific arrangements of straight cracks, viz. two non-staggered parallel cracks, two staggered parallel cracks, and two cracks positioned at an angle to each other. Non-staggered parallel cracks of equal length l_0 were found to be the worst case scenario in terms of crack interaction. For such configurations errors in the SIFs are reported as 7% for a lateral spacing of $S/l_0 = 0.5$ and 30% for $S/l_0 = 0.25$, respectively.

The accuracy of the crack opening displacements, D , obtained by Kachanov's approach can be assessed by comparing its results to FE predictions for arrangements of five non-staggered, uniformly spaced, parallel cracks of equal length (Fig. 4.2a). The errors of the

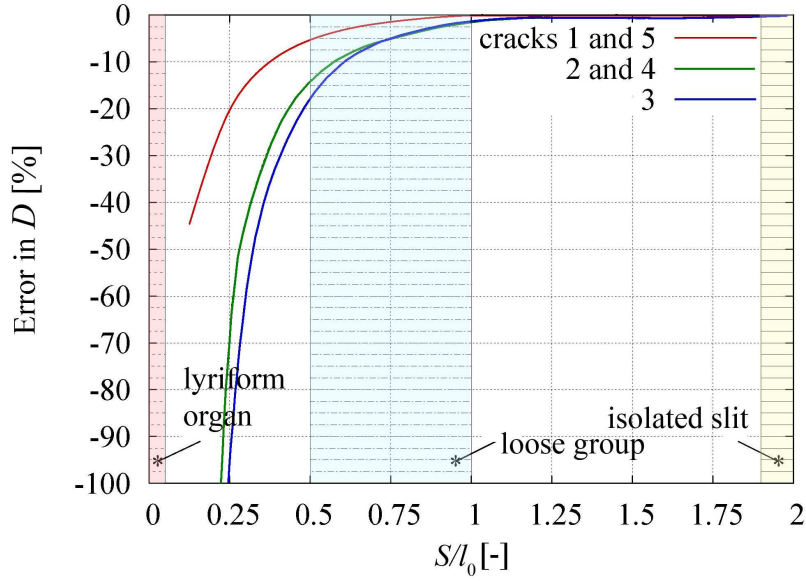


FIGURE 4.1: Error in Kachanov's approximation ($D_{c,K}$) for the crack opening distances with respect to FE results ($D_{c,FE}$), $(D_{c,K} - D_{c,FE})/D_{c,FE}$, for the case of five non-staggered parallel uniformly spaced cracks as functions of the lateral distances of the cracks, S . Kachanov's method predicts smaller crack D s than the FEM. Ranges for different spacings occurring in slit sensilla are referred to as I (single slits), II (loose groups), and III (lyriform organs).

opening D s at the centers of the cracks, D_c , calculated according to Kachanov are shown in Fig. 4.1 as functions of the distance S between neighboring cracks. Evidently, Kachanov's method can be used for studying arrays of cracks with lateral spacings $S/l_0 \gtrsim 0.5$, i.e., in the present context of slit sensilla, for isolated slits and for loose groups of slits. For spacings $S/l_0 \lesssim 0.25$, however, the approximations for the crack D given in section 3.1.3 break down.

Alternatively, on the one hand an enhanced Kachanov's method (see Chapter 3.1.1) or, on the other hand, Finite Element analyses can be used to study arrangements of slits with spacings as close as those found in lyriform organs. Even though some effort has to be put into meshing and the requirements on computational power are higher than for Kachanov's method, Finite Element models can easily handle slits of a wide range of shapes, of finite width, and of arbitrary distributions. They also provide the capability of modeling slits in non-planar regions of the cuticle. Accordingly, the most promising route for studying the

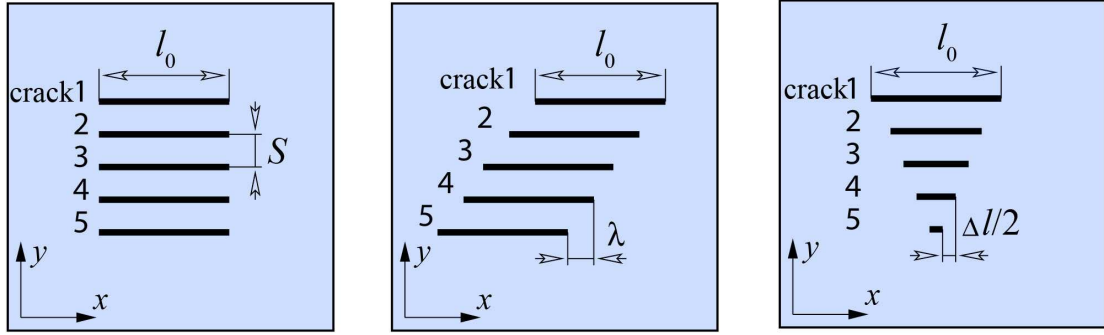


FIGURE 4.2: Basic patterns of planar models examined by Kachanov's method and geometrical parameters of arrays of five cracks. **a** Non-staggered array of five parallel slits, **b** oblique bar arrangement of five parallel cracks, and **c** triangular arrangement of five parallel cracks.

crack opening distances of slits in lyriform organs appears to be the use of Finite Element models rather than extended versions of Kachanov's theory.

4.1.1.2 Results of the analytical models

As a step towards understanding the functioning of the slit sense organs of arachnids the effects of a number of geometrical parameters on the crack opening distances in generic groupings of five parallel cracks (Fig. 4.2) were studied by Kachanov's method. The parameters of primary interest are the lateral spacing between neighboring cracks, S , the amount of longitudinal staggering of the cracks, λ , and the difference in length between neighboring cracks, Δl . For all models the geometrical parameters are normalized to the length of the longest crack which is held constant at l_0 . The results for the opening distances, D , are normalized with respect to a reference configuration, which is the mid-length opening distance of an isolated crack $D_{cc}/l_0 = 11.21 \times 10^{-5}$ under mode I unit loading, $\sigma_{a,r} = 1$ MPa, in an infinite medium (Hahn, 1976). Uniaxial loading, i.e. uni-axial stress, in the direction transverse to the cracks is considered. For convenience, the above parameters of the reference configuration are also listed in Table B.2.

In this section by convention positive values of D_c/D_{cc} correspond to the opening displacement of the faces of a given crack.

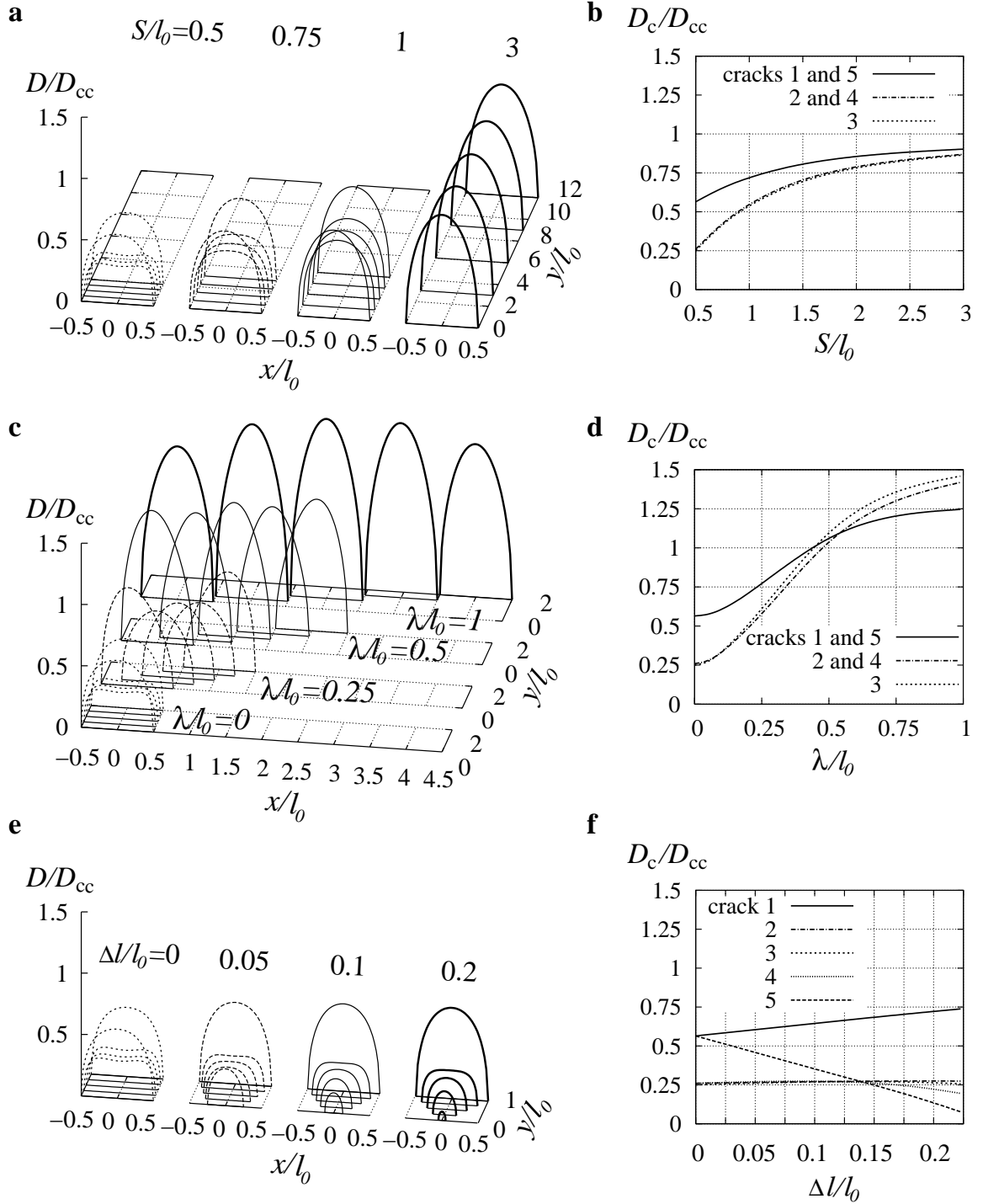


FIGURE 4.3: Parametric study of the relevance of the main geometrical parameters on the crack opening distances in groups of 5 cracks. **a** and **b**: Shielding effects change nonlinearly as the distance between slits, S , increases. **c** and **d**: Increasing the longitudinal shifts λ between cracks results in a transition from shielding to amplifying effects within the array of cracks (lateral spacing of $S/l_0 = 0.5$). **e** and **f**: Changing the lengths of the cracks within an arrangement by increments Δl increases the range of inputs that elicit a response ($S/l_0 = 0.5$). **b**, **d**, and **f** show the normalized D s at the centers (D_c/D_{cc}) of the cracks as functions of the varied parameters.

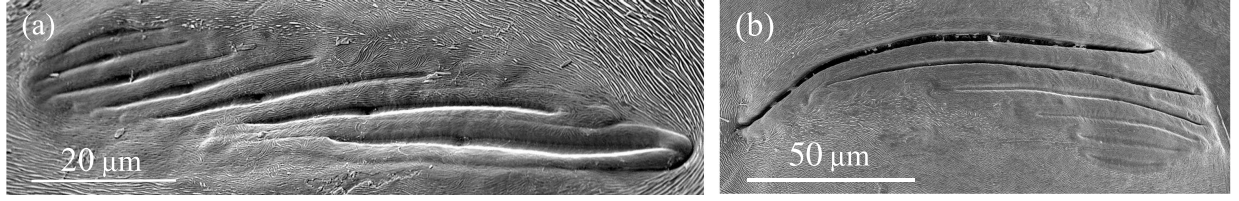


FIGURE 4.4: SEM images of (a) lyriform organ VS3 on the patella and (b) lyriform organ HS8 at the distal end of the tibia of *C. salei* (Müllan, 2005).

The results of the parameter studies are summarized in Fig. 4.3. Two examples of lyriform organs are shown in Fig. 4.4 to illustrate actual configurations. In the oblique bar arrangement VS3 of *C. salei* (Fig. 4.4a) a gradation of the slit lengths of l_0 , $0.96 l_0$, $0.8 l_0$, $0.64 l_0$, $0.54 l_0$, $0.48 l_0$, and $0.32 l_0$ and a longitudinal shift between the slits of $\lambda/l_0 = 0.29$, 0.24 , 0.24 , 0.18 , 0.11 , and 0.01 is found. Organ HS8, which is depicted in Fig. 4.4b, is of triangular shape and has a gradation of the slit lengths of l_0 , $0.87 l_0$, $0.62 l_0$, $0.38 l_0$, $0.27 l_0$, and $0.2 l_0$ and a longitudinal shift between the slits of $\lambda/l_0 = 0.16$, 0.14 , 0.1 , 0.04 , and 0.02 . The values of D predicted for arrays of parallel cracks of equal length l_0 and transverse spacings of $S/l_0 = 0.5$, 0.75 , 1 , and 3 are depicted in Fig. 4.3a. Note that at the inner cracks at $S/l_0 = 0.5$ the shapes of the curves of the deformations along the crack faces of the inner cracks are no longer ellipses which is the effect of the enrichment of the elliptical shape approximating the crack face displacements by quadratic functions (Eq. 3.7 in Chapter 3.1.3). In Fig. 4.3b the normalized opening distances at the centers of the cracks are plotted as functions of S/l_0 . Figure 4.3c shows the crack face opening displacements obtained for staggered parallel cracks of equal length l_0 and spacing $S/l_0 = 0.5$, the longitudinal shifts taking values of $\lambda/l_0 = 0$, 0.25 , 0.5 , and 1 . The dependence of the relative center opening displacements on λ/l_0 for such configurations is presented in Fig. 4.3d. The effects of decreasing crack lengths introduced via constant length decrements Δl into symmetrical loose groupings are visualized in Fig. 4.3e, where the crack D s predicted for $\Delta l/l_0 = 0$, 0.05 , 0.1 , and 0.25 are shown for $S/l_0 = 0.5$. Figure 4.3f depicts the variation of D_c/D_{cc} as functions of $\Delta l/l_0$ for arrangements of this type. Note that the left side in Figs. 4.3b, d, and f pertains to an arrangement of five parallel straight cracks at $S/l_0 = 0.5$, $\lambda/l_0 = 0$, and $\Delta l/l_0 = 0$.

4.1.2 Planar FE models of generic slit arrays

The shapes of individual slits and the arrangements of multiple slits covered by the present work are shown in Fig. 4.5 together with the geometrical parameters used to describe them. They are all based on the diversity of slit sensilla actually occurring in arachnids (see Chapter 4.2.2 and Barth (2002a)).

In a first step towards understanding the working principles of slit sense organs we evaluated the slit face displacements of idealized slit arrangements (Fig. 4.5) at the slits' centers, D_c , which do not necessarily coincide with the displacements at the locations of the dendrites in actual slit sensilla (see Chapter 4.2.2).

4.1.2.1 Deformation of a single slit subjected to a normal uni-axial load

A study of important geometrical parameters of isolated slits, i.e., aspect ratio, shape, centerline geometry, slit length, and orientation of the slit with respect to the uni-axial loads, is carried out in order to identify their influence on the face displacements of the slits. The effects of the aspect ratio are of special interest, because the campaniform sensilla of insects are typically circular to elliptical with aspect ratios l_0/w_0 rarely exceeding 3 (Barth, 1981), whereas arachnid slit sensilla are much more elongated.

Figure 4.6a depicts the relative slit face displacements predicted for capped rectangular slits and ellipses of length l_0 with aspect ratios ranging from $l_0/w_0 = 1$ to 100 under the action of normal uni-axial stresses. The increase of D_c/D_{sc} to 1.5 (by 50%) obtained for $l_0/w_0 = 1$ is mainly a consequence of the area of such circular openings in the cuticle, which is about eighty times larger than that of a slit with $l_0/w_0 = 100$ (Fig. 4.6a').

In Fig. 4.6a and 4.6a' it is difficult to distinguish the predictions for D_c/D_{sc} pertaining to capped rectangular slits and to ellipses. Therefore, the normalized difference in the relative face displacements, $\Delta D_c/D_{sc} = (D_{c,slit} - D_{c,ell})/D_{sc}$, is plotted in Fig. 4.6b, and the difference between the areas of capped rectangles and ellipses of equal length l_0 , $\Delta A/l_0^2 = (A_{slit} - A_{ell})/l_0^2$, normalized by the area of a square of size $l_0 \times l_0$, is plotted versus the aspect ratio l_0/w_0 in Fig. 4.6b'. The capped rectangles give rise to higher face displacements for all nontrivial aspect ratios. This behavior is largely due to the larger area of the capped

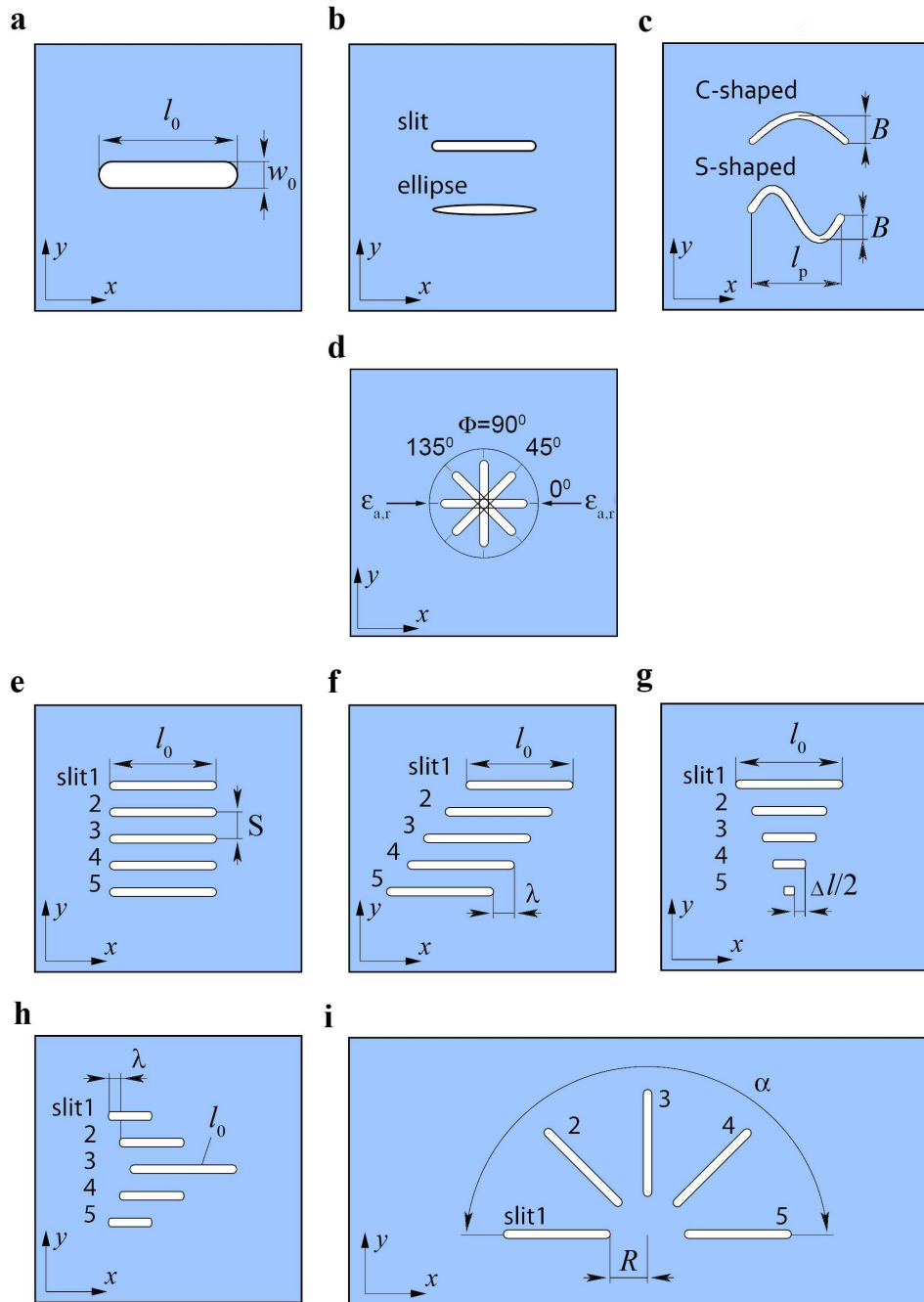


FIGURE 4.5: Basic patterns of planar models examined by FE analysis and geometrical parameters of a single slit and of arrangements of five slits. **a** Slit geometry, **b** "capped rectangular" and elliptical slits, **c** C-shaped and S-shaped slit geometries, **d** orientation of a single slit relative to a uni-axial reference compressive load $\epsilon_{a,r}$, **e** non-staggered array of five parallel slits, **f** oblique bar arrangement of five parallel slits, **g** triangular arrangement of five parallel slits, **h** heart shaped arrangement of five parallel slits, and **i** fan arrangement of five slits.

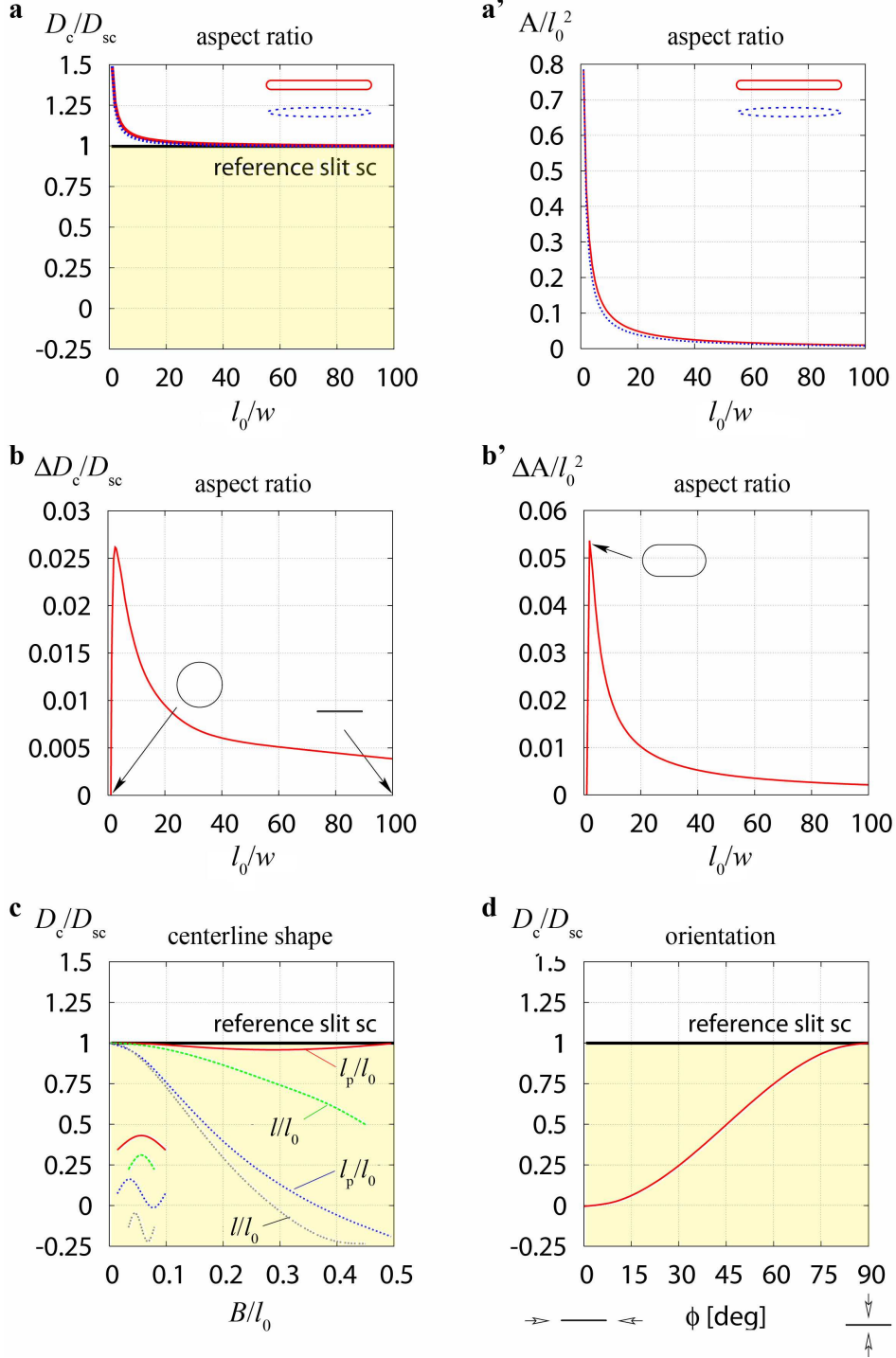


FIGURE 4.6: Parametric study of the influence of the principal geometrical parameters of a single slit on the normalized relative slit face displacements at mid-length. **a** Dependence of D_c/D_{sc} on the slits' aspect ratio l_0/w_0 , **a'** normalized area of "capped rectangular" and elliptical slits, and **b** variation of the normalized difference between the relative face displacements of "capped rectangular" and elliptical slits as function of l_0/w_0 , **b'** normalized difference in area between capped rectangles and ellipses of given the aspect ratio, plotted versus l_0/w_0 (peak at 2) **c** dependence of D_c/D_{sc} on the amplitude parameter B/l_0 describing C-shaped and S-shaped slit geometries (insets correspond to fixed distances $l_p = l_0$ between the endpoints, and to fixed slit length $l = l_0$, respectively, for $B/l_0 = 0.4$), and **d** dependence of D_c/D_{sc} on the orientation angle Φ of the uni-axial far-field stress. Note that **a** to **c** correspond to $\Phi = 90^\circ$.

rectangles (A_{slit}) compared to ellipses (A_{ell}) of equal aspect ratio. The maximum difference in $\Delta A/l_0^2$ is only 0.053 (=5.3%) of the area of a square of size $l_0 \times l_0$. It is reached at an aspect ratio of $l_0/w_0 = 2$, whereas the maximum of $\Delta D_c/D_{\text{sc}} \approx 0.026$ (=2.6%) is predicted for $l_0/w_0 \approx 2.5$. Note that for the aspect ratio of $l_0/w_0 = 1$ both the capped rectangular and the elliptical slits degenerate into circles of diameter l_0 .

The relative face displacements of slits with straight, C-shaped and S-shaped geometries under normal loadings are compared in Fig. 4.6c. For the latter two cases the centerlines of the slits are half and full periods, respectively, of sine waves of amplitude B/l_0 (see Fig. 4.5c). Two sets of results are plotted in Fig. 4.6c, in one of which the integrated length of the slits' midline, l , is set to l_0 (green and grey lines), whereas in the other the distance between the slits' endpoints, i.e. their projected length l_p , is maintained at l_0 (dark red and blue lines). The predictions show that, among the geometries examined, straight slits give rise to the largest relative face displacements under normal compressive loading. When the distance l_p between the endpoints in C- and S-shaped slits is held constant, the slit faces of the C-shaped slit deform similarly to those of a straight slit. In S-shaped slits increasing B/l_0 causes the center region of the slit to rotate progressively, so that the relative slit face deformation D_c/D_{sc} decreases quickly (the local load angle progressively deviates from 90° in the center region). For both C-shaped and S-shaped slits the values of D_c/D_{sc} decrease with increasing values of B/l_0 when the integrated length of the slits is held at $l = l_0$, because the projected lengths of the slits facing the load are reduced. For configurations with $B \gtrsim 0.28 l_0$ S-shaped slits of length $l = l_0$ show negative values of D_c/D_{sc} , i.e. such slits open up at mid-length when subjected to compressive normal loads. Figure 4.6d which gives the directional dependence of slit deformation of a single slit which will be discussed in Chapter 4.2.2.2.

In contrast to Fig. 4.6 the changes in D_c (ΔD_c) are evaluated and plotted as functions of the relative changes in the geometrical parameters varying in slit sensilla, viz. slit length l , aspect ratio l/w_0 , orientation Φ , and shape parameter B in C- and S-shaped slits (Fig. 4.5a-c) in a single diagram (Fig. 4.7) to allow a direct comparison of the sensitivities to such changes. The limits of the relative changes to geometrical parameters are presented in Table 4.1.

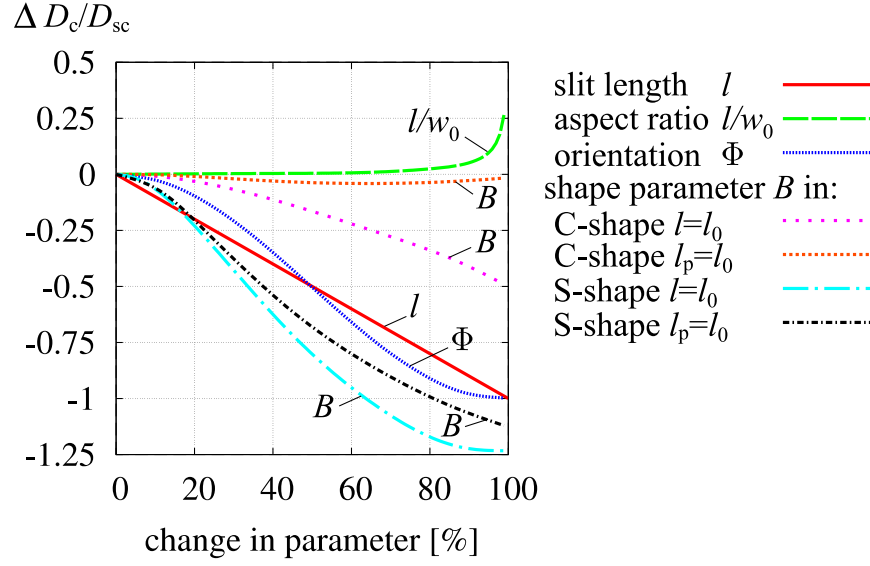


FIGURE 4.7: Parametric study of the change in relative slit face displacement $\Delta D_c/D_{sc}$ as function of changes in the principal geometrical parameters of a single slit, viz. slit length l , aspect ratio l/w_0 , orientation Φ , and amplitude parameter B in C- and S-shaped slits.

TABLE 4.1: Relative change of parameters in single slits as used in Fig. 4.7

Parameter	0%	100%
l	$l = 1$	$l = 0$
l/w_0	$l/w_0 = 100$	$l/w_0 = 1$
B	$B/l = 0$	$B/l = 0.45$
Φ	$\Phi = 90^\circ$	$\Phi = 0^\circ$

4.1.2.2 Deformation of arrays of five parallel slits under a uni-axial normal load

The influence of selected geometrical parameters on the response of arrays of mechanically interacting slits was studied for three generic arrangements consisting of five parallel slits each, a non-staggered array (Fig. 4.5e), an oblique bar arrangement (Fig. 4.5f), and a triangular arrangement (Fig. 4.5g) (see Barth et al. (1984)). For the latter two arrangements the lateral spacing between neighboring slits was set to $S/l_0 = 0.04$, which

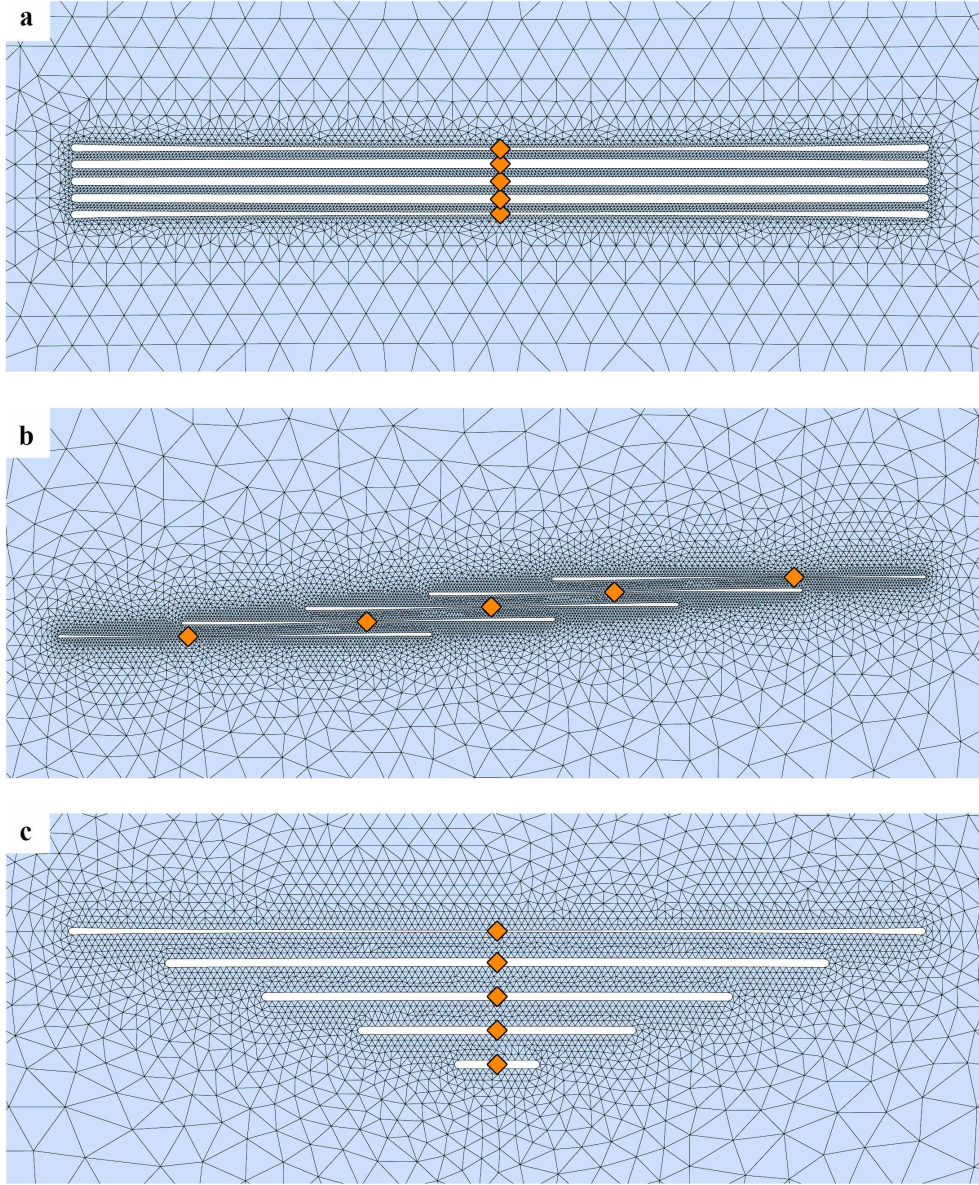


FIGURE 4.8: Deformed configurations of three FE models subjected to uni-axial compressive loading at $\Phi = 90^\circ$. **a** Stack of five parallel slits with aspect ratios $l_0/w_0 = 100$ and lateral spacings $S/l_0 = 0.02$. Due to bending of the “ligaments” (cuticular material between slits), the outer slits are strongly compressed whereas the inner slits expand (displacement scaling factor 2×10^4). **b** Oblique bar array in the deformed state at lateral spacings $S/l_0 = 0.04$. Using a lateral shift $\lambda/l_0 = 0.35$ gives rise to similar mid slit face deformations D_{sc} for all of the slits (displacement scaling factor 5×10^3). **c** Triangular arrangement of slits spaced at $S/l_0 = 0.04$ with a linear gradation in slit length $\Delta l/l_0 = 0.225$. Considerable shielding is evident (displacement scaling factor 1.5×10^4). Positions of maximum slit face displacement are indicated by orange diamond shaped symbols.

TABLE 4.2: Change of parameters in a stack of five slits

Parameter	0%	100%
S	$S/l = 0.02$	$S/l = 3$
Δl	$\Delta l/l = 0$	$\Delta l/l = 0.2$
λ	$\lambda/l = 0$	$\lambda/l = 3$

corresponds to spacings found in real lyriform organs. This lateral spacing gives rise to thin “ligaments” (cuticular material between neighboring slits) with a width of $0.03 l_0$ each. Uni-axial stresses acting normal to the slits ($\Phi = 90^\circ$) were applied. Figure 4.8 shows the corresponding deformed configurations, the displacements being multiplied by factors of 2×10^4 , 5×10^3 , and 1.5×10^4 for visualization. The orange diamond shaped symbols indicate the positions of maximum slit face displacements.

Lateral spacing. The effects of the lateral spacing between neighboring slits, S , were investigated for an array of five non-staggered slits of equal length l_0 . Figure 4.9a (left: overview, right: detail plot for low values of S/l_0) shows that interaction effects essentially vanish for $S/l_0 \gtrsim 3$, where the difference in D_c of the neighboring slits is smaller than 3% of the maximum slit face displacements of the outer slits. For closely spaced slits with $S/l_0 \lesssim 0.1$, i.e. in the range found in lyriform organs, the inner slits of the arrays show very small or even negative relative face displacements. Bending of the “ligaments” between slits, especially of the outermost ones, is prominent in this regime.

Longitudinal shift. Oblique bar formations were studied by FE simulations of five closely arranged parallel slits, in which the lateral spacings were kept fixed at $S/l_0 = 0.04$, whereas the longitudinal shift between neighboring slits, λ/l_0 (Fig. 4.5f), was varied. As is evident from Fig. 4.9b the relative slit face displacements significantly exceed those of a single slit for the range $0.25 \lesssim \lambda/l_0 \lesssim 2.5$. Note that the values for λ found in lyriform organs, e.g. $0.25 \lesssim \lambda/l_0 \lesssim 0.33$ in organ VS3 of *C. salei*, fall into this range. A maximum magnification factor of $D_c/D_{sc} \approx 4.25$ is predicted for the center slit at $\lambda/l_0 \approx 0.85$. D_c decreases rapidly as λ approaches l_0 (i.e. $\lambda/l_0 = 1$). For $\lambda/l_0 = 0.34$ the face displacements of all slits are nearly equal (Fig. 4.9b) with an amplification factor of $D_c/D_{sc} \approx 1.5$.

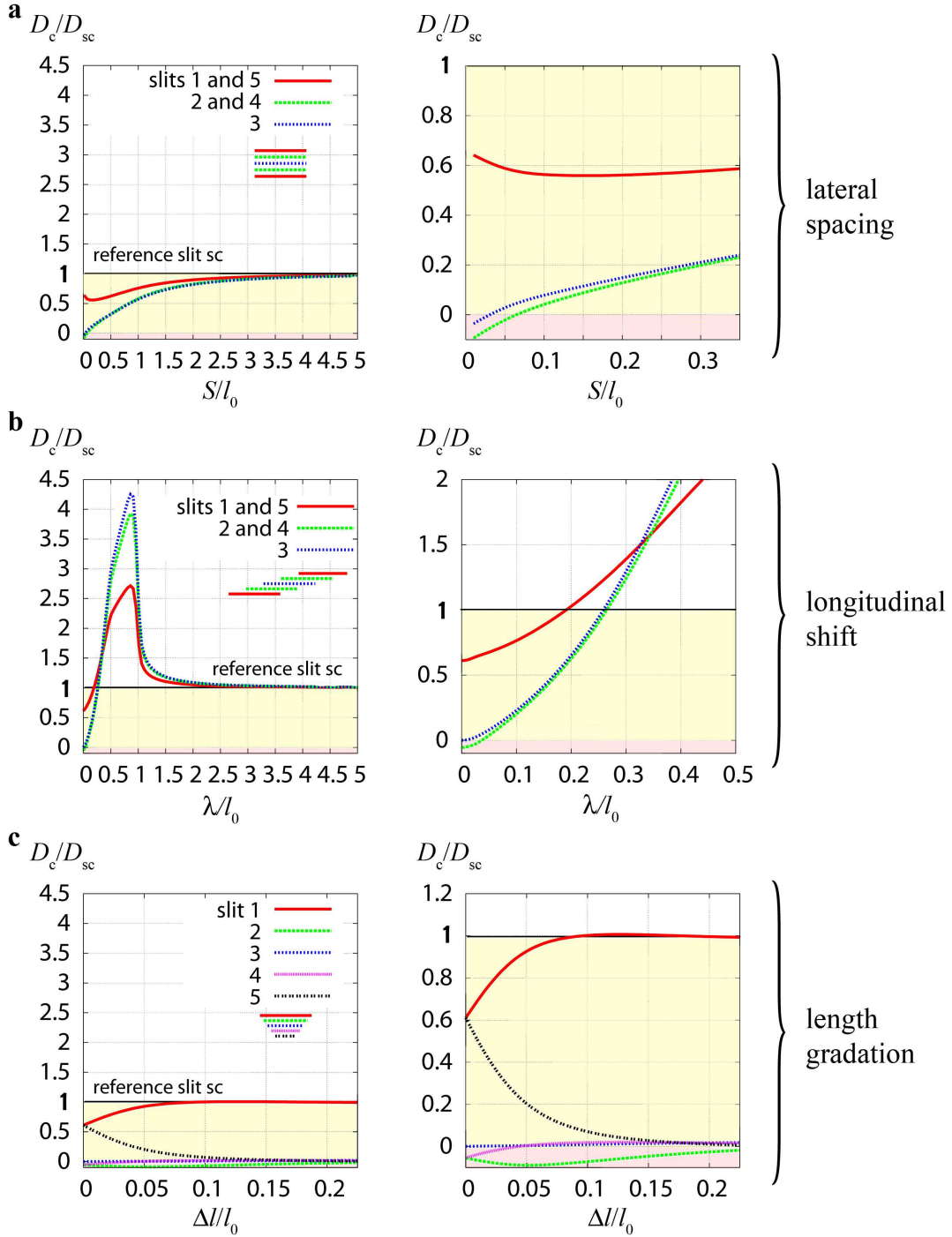


FIGURE 4.9: Parametric study of the influence of the principal geometrical parameters of arrays of five parallel slits on the normalized relative slit face displacements at mid-length ($\Phi = 90^\circ$). Note difference in scaling of both x -axes in left and right panels, respectively. **a** As lateral spacings S/l_0 between slits are reduced shielding effects increase and the inner slits open up (D_c/D_{sc} negative) for $S/l_0 \leq 0.07$ due to bending of the cuticular “ligaments” between slits (see also Fig. 4.8a). **b** Increasing the longitudinal shift λ/l_0 between slits from 0 to 0.85 while maintaining $S/l_0 = 0.04$ causes D_c/D_{sc} to increase rapidly to a maximum. At $\lambda/l_0 \approx 0.34$ the relative face displacements of all slits take nearly identical values. **c** Changing the length of the slits by $\Delta l/l_0$ in triangular arrangements with lateral spacings of $S/l_0 = 0.04$ results in marked shielding of the shorter slits 2, 3, 4 and 5. For $\Delta l/l_0 \gtrsim 0.09$ the longest slit behaves similarly to a single slit ($D_c/D_{sc} = 1$).

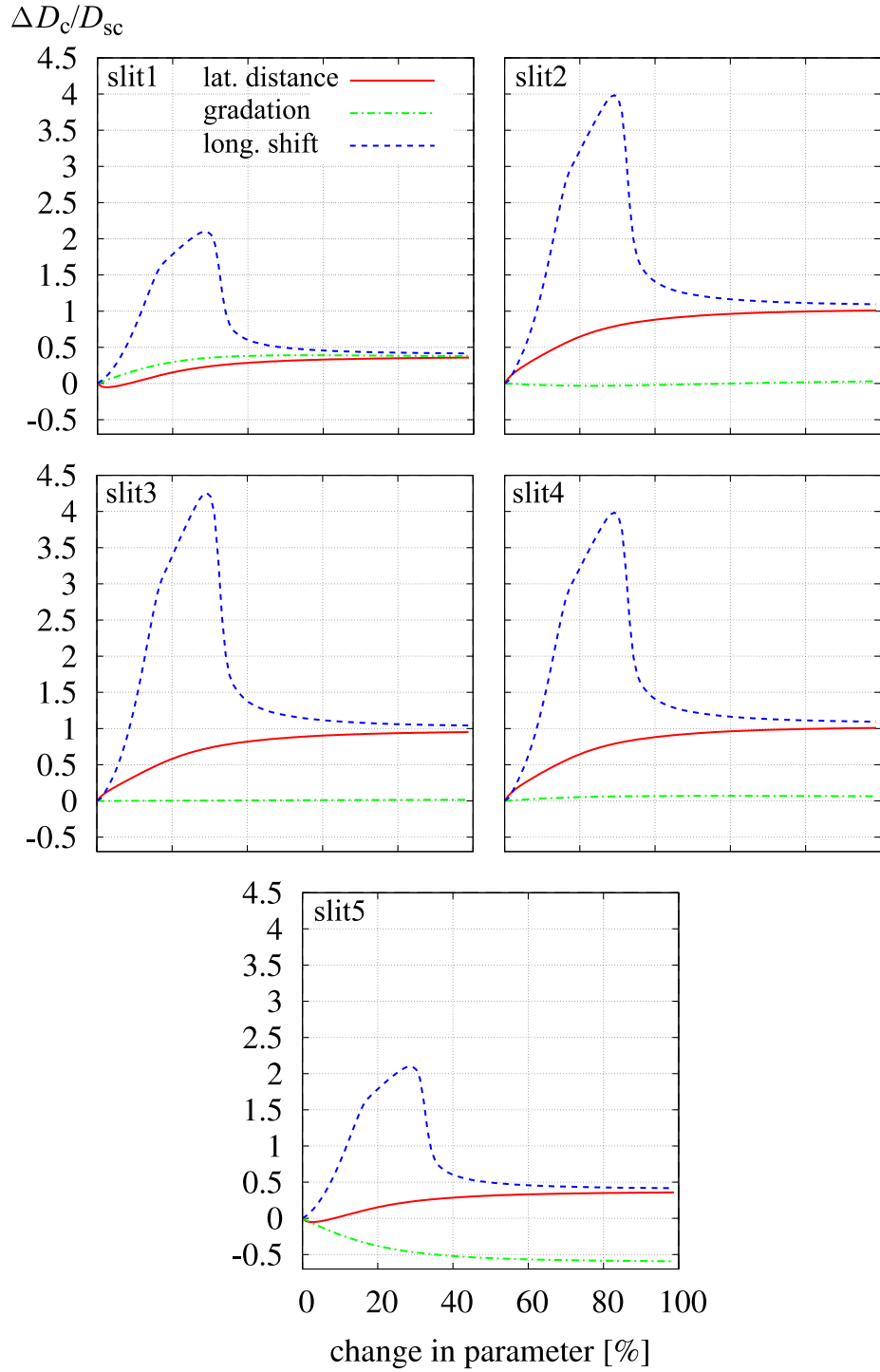


FIGURE 4.10: Parametric study of the change in relative slit face displacement $\Delta D_c/D_{sc}$ as function of the changes in principal geometrical parameters of stacks of five parallel slits, viz. lateral distance S in parallel, gradation Δl in triangular, and longitudinal shift λ in oblique bar formations. See Table 4.2 for ranges of geometrical parameters.

Length gradation. The lengths of the slits in symmetric triangular arrays can be described by the length gradation $\Delta l/l_0$ (Fig. 4.5g). For the studied lateral spacing of $S/l_0 = 0.04$ marked shielding effects are present for $\Delta l/l_0 \gtrsim 0.1$ (see Fig. 4.8c and Fig. 4.9c). Typically, slit length gradations found in natural lyriiform organs such as organ HS8 vary throughout the organ from $\Delta l/l_0 \approx 0.08$ to 0.3. It is interesting to note that for the above value of S the mid-length relative face displacement of slit2 is negative throughout the range of $\Delta l/l_0 \gtrsim 0.1$, i.e., the slit opens up under compressive uni-axial stresses acting at an angle of $\Phi = 90^\circ$ (for the definition of Φ see Fig. 4.5d).

Alternatively, the results of the previous parametric study can be plotted as function of the change of each parameter describing generic arrays of slits, i.e. S , λ , and $\Delta l/l_0$ (Fig. 4.10). The ranges of variation of the geometrical parameters are listed in Table 4.2.

4.1.2.3 Dependence of the deformation of a single slit on the direction of uni-axial loads

Uni-axial far-field stresses were applied to single slits of straight, C-shaped and S-shaped geometries in directions varied by increments of 5° of the in-plane angle Φ . A value of $B/l_0 = 0.25$ was chosen for the shape parameter of the curved slits (Fig. 4.5c), which lies within the range observed in real C- and S-shaped slits (Fig. 2.3b). The integrated lengths of the slits' centerlines were set to $l = l_0$ in each case.

Figure 4.6d shows the dependence of D_c of a straight slit of capped rectangle shape on the orientation angle Φ of the compressive uni-axial far-field strain as defined in Fig. 4.5d. In Fig. 4.11 the predicted relative slit face displacements at mid-length are presented in the form of a polar diagram. The maxima of D_c for both the straight and the C-shaped slits occur at load directions that are perpendicular to the slits' long axes, i.e. $\Phi = 90^\circ$. The C-shaped slit displays a lower sensitivity at all loading angles, the maximum value of D_c/D_{sc} reaching a value of about 0.85. For the S-shaped slit with $B/l_0 = 0.25$ the maximum face displacements are predicted to occur for uni-axial stresses oriented at $\Phi \approx 140^\circ$ from the slit axis and their absolute values are comparable to those predicted for the C-shaped slit, i.e., they are also smaller than those of the straight slit.

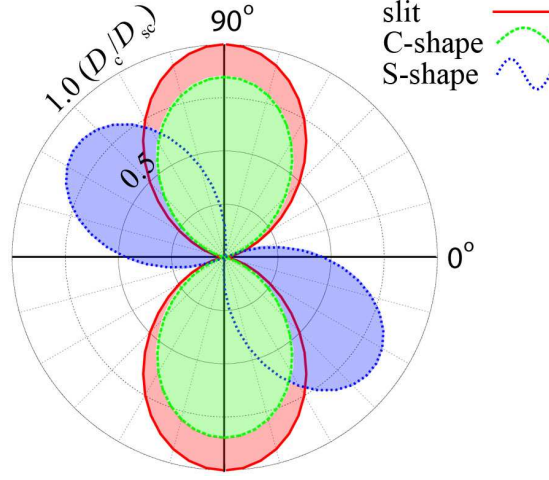


FIGURE 4.11: Directional sensitivity to uni-axial compressive far-field loads of straight, C-shaped and S-shaped slits having the same length l_0 and an amplitude parameter of $B/l_0 = 0.25$. The maximum of D_c for the straight and C-shaped slits is found at $\Phi = 90^\circ$. The S-shaped slit is predicted to be most sensitive to loads acting at $\Phi = 140^\circ$.

4.1.2.4 Dependence of the deformation of fan-type arrangements of five slits on the direction of uni-axial loads

The influence of the direction of far-field uni-axial compressive stresses was studied for fan-type arrays of five slits of aspect ratio $l_0/w_0 = 100$ each, the total angles α subtended by the arrangements being 45° , 90° , and 180° , respectively. The slits were arranged radially at angular increments of $\alpha/4$ and their “inner” tips were positioned at a radius of $R = 0.35 l_0$. This value of R was chosen on the basis of an actual lyriform organ on the chelicerae of the spider *Cupiennius salei* (Barth and Libera, 1970). For details of the configurations see Fig. 4.5i.

In a fan-type array with $\alpha = 45^\circ$ considerable shielding is present for the inner slits (Fig. 4.12a), so that for them D_c does not exceed $0.25 D_{sc}$. The maximum value of D_c for the outermost slits was found to reach approximately $0.8 D_{sc}$ for this arrangement. Increasing the angle α subtended by the slits changes the directional sensitivity of the outermost slits, 5 and 1, and reduces the shielding of the inner slits (Fig. 4.12b). Fans with $\alpha = 180^\circ$ are well suited for sensing uni-axial loads acting in any direction (Fig. 4.12c), with predicted values of D_c exceeding $0.65 D_{sc}$ for all orientations. The sensitivity at $\Phi = 0^\circ$ is

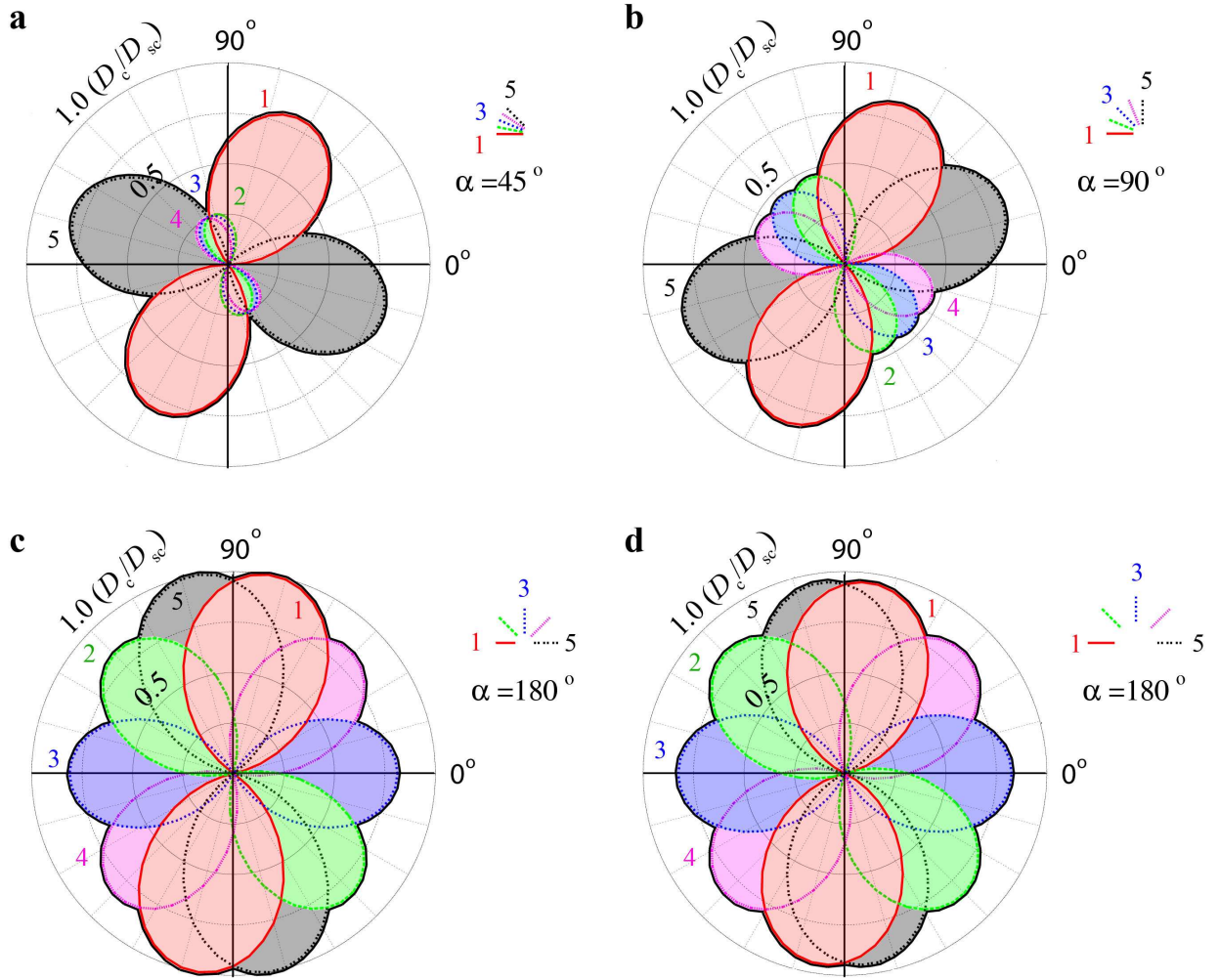


FIGURE 4.12: Effects on the directional sensitivity of varying the subtended angle α and the radial position of the slits' ends R within fan-shaped arrangements of five slits. **a** The inner slits are shielded at $\alpha = 45^\circ$ and $R = 0.35 l_0$ (R see Fig. 4.5i). **b** Shielding effects decrease when α is increased to 90° . **c** At $\alpha = 180^\circ$ at least one slit is sensitive to any loading direction. **d** Shielding of the outer slits is only slightly increased by shifting the slits radially to $R = 0.85 l_0$ at $\alpha = 180^\circ$. The envelopes of the responses are shown as bold solid lines.

about 20% lower than at $\Phi = 90^\circ$.

A second fan-type arrangement with $\alpha = 180^\circ$ and $R = 0.85 l_0$ is inspired by a lyriform organ on the trochanter of the whip spider *Admetus pumilio* (Barth and Stagl, 1976). Figure 4.12d shows the relative face displacements at mid-length predicted for this set

of parameters, the results being slightly more isotropic compared to those obtained for $R = 0.35 l_0$ (Fig. 4.12c).

To relate the positions of the dendrites (red filled circular markers in Fig. 4.13) to the slit face deformations, the latter are plotted along the slits in Fig. 4.13a for the fan-type arrangement with $R = 0.35 l_0$ and $\alpha = 90^\circ$ subjected to uni-axial far-field stresses acting at angles of $\Phi = 90^\circ$ and $\Phi = 120^\circ$. The maxima of the D_c are not at the slits' centers and the slit face displacements are skewed towards the outer ends of the slits. This effect is a consequence of the geometrical arrangement of the slits. The values for the load direction in Fig. 4.13 are chosen either to match the load direction a single slit is most sensitive to ($\Phi = 90^\circ$) or to check if the location of the maximum slit face displacement changes when the load angles are altered ($\Phi = 120^\circ$).

4.1.2.5 Dependence of the deformation of arrays of five parallel slits on the direction of uni-axial loads

All results in this section pertain to parallel slits with transverse spacings of $S = 0.04 l_0$, which is well within the range found in arachnid lyriform organs.

Figure 4.14a shows the predicted directional sensitivities of the relative face displacements at mid-length of five slits making up an oblique bar formation with a longitudinal shift of $\lambda = 0.34 l_0$. This value of λ is special because the D_c of all slits coincide at $\Phi = 90^\circ$ (Fig. 4.9b). The largest deformations occur in the center slit at an angle of $\Phi \approx 80^\circ$, where D_c/D_{sc} reaches a value of approximately 1.6, i.e., there is considerable amplification. The shapes of the curves of the slit face deformations along the slits are symmetric for the inner slits and are skewed for the outermost ones (Fig. 4.13b). Note that the left part of Fig. 4.13b ($\Phi = 90^\circ$) describes the same situation as Fig. 4.8b.

The predicted response of a heart shaped array (Fig. 4.5h) to uni-axial compressive loads of different orientations is depicted in Fig. 4.14b, which pertains to a longitudinal shift of $\lambda/l_0 = 0.15$ and slit lengths of $0.4 l_0$, $0.6 l_0$, l_0 , $0.6 l_0$, and again $0.4 l_0$ (compare (Barth et al., 1984)). The highest sensitivity is predicted to occur under normal loading, $\Phi = 90^\circ$, but strong side lobes (slit1, 2, 4, and 5) are present at angles of $\Phi = 60^\circ$ and $\Phi = 120^\circ$, indicating multi-directional sensitivity. Figure 4.15 depicts the deformed FE model of the

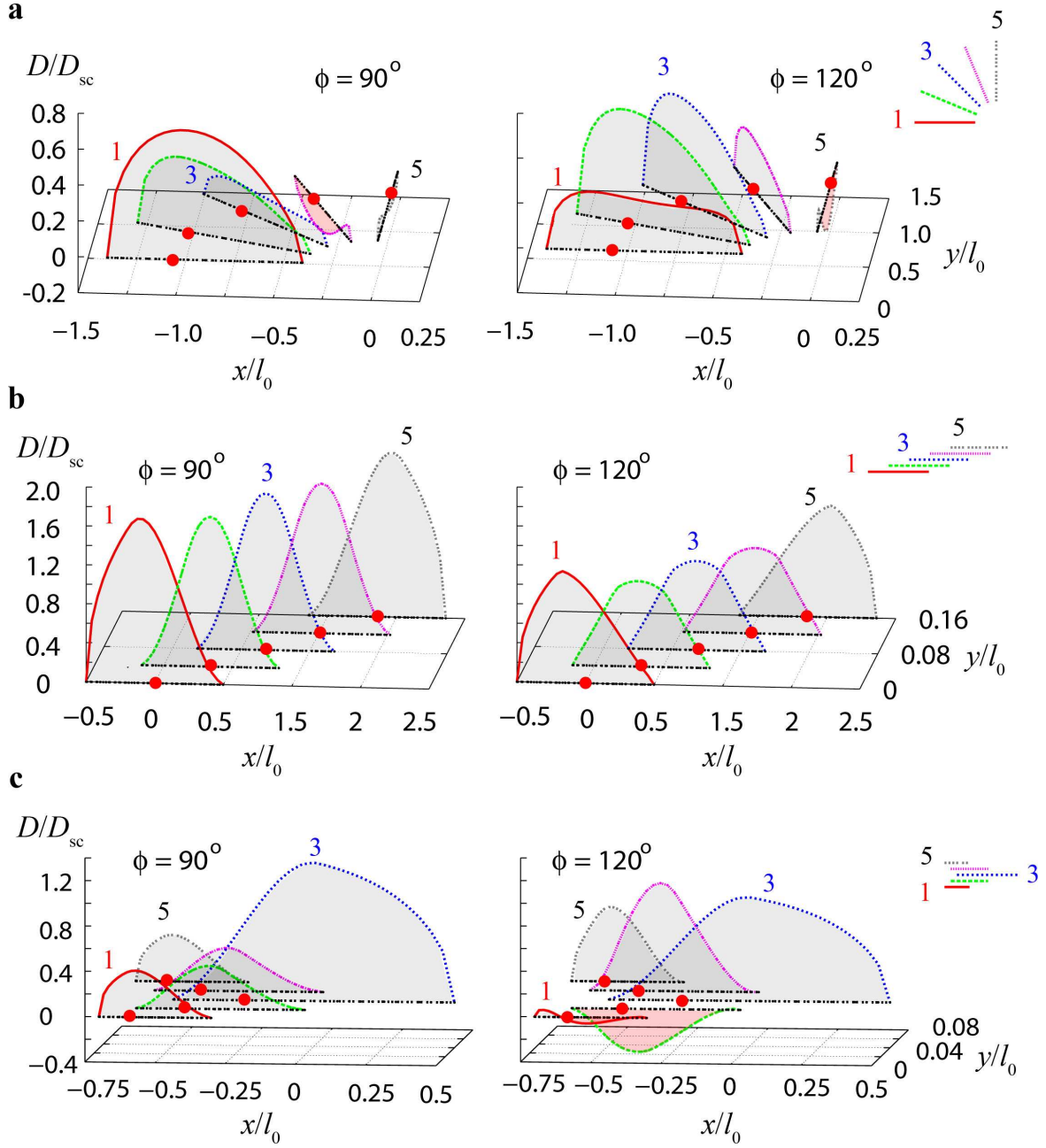


FIGURE 4.13: Slit face deformations D along the slits. **a** Fan-like arrangement with $R = 0.35 l_0$ and $\alpha = 90^\circ$. The deformations along the faces are skewed for both loading directions, $\Phi = 90^\circ$ and $\Phi = 120^\circ$. **b** Oblique bar array with $S = 0.04 l_0$ and $\lambda = 0.34 l_0$. Symmetric slit face deformations are evident for the inner slits and skewed shapes for the outermost slits at load directions $\Phi = 90^\circ$ and $\Phi = 120^\circ$. **c** Heart shaped array with $S = 0.04 l_0$, $\lambda = 0.4 l_0$ and $\Delta l = 0.2 l_0$. The slit face deformations are skewed due to the lateral shift of the slits. At $\Phi = 120^\circ$ slits 1 and 2 show negative values of D_c/D_{sc} , i.e. they open up. Approximate positions of the dendrites are indicated by red filled circles.

heart shaped arrangement under loading perpendicular to the slits' long axes, $\Phi = 90^\circ$, corresponding to Fig. 4.13c. It shows that the maximum slit face displacements (orange diamond shaped symbols in Fig. 4.15) are shifted to one end with the exception of the center slit. The positions of the maximum face displacements of slits 1 to 5 at $\Phi = 135^\circ$ are similar to those predicted for $\Phi = 90^\circ$, but the values of D_c are different (Fig. 4.13c), which means that the sensitivities of the slits are different under different load directions.

For a symmetric triangular array with a linear gradation of the slit lengths of $\Delta l/l_0 = 0.15$ the relative face displacements at mid-length, D_c , of the longest slit closely approach those of a single slit (Fig. 4.14c). The shorter slits show similar directional responses of the relative face displacements, but are strongly shielded, as is evident from the detail view in Fig. 4.14c. Note that no data is given for slit 2, which widens under compressive loading and, accordingly, shows negative values of D_c/D_{sc} .

4.1.3 Planar FE models of slit arrays imitating lyriform organs

Note that the load angle Φ is measured relative to the longitudinal axis of slit1 in each arrangement. In the combination of the organs HS8/HS9 the reference slit is slit1 of HS8. In the figures the slit configurations are depicted for loadings acting under $\Phi = 0^\circ$ (Fig. 4.5d).

4.1.3.1 A special case: The measured and simulated deformation of organ HS8

In Barth and Libera (1970) it is shown that lyriform organs may be positioned in close neighborhood so that interaction effects between the organs may be encountered. On the anterior face of the tibia of *C. salei* two triangular lyriform organs, HS8 and HS9, are found in close proximity (Fig. 4.16a). The orientations of the two organs differ by approximately 26° and their distance from each other is approximately the size of the longest slit in the arrangements. Therefore, in agreement with Chapter 4.1.1 interaction effects are to be expected between the organs. When the organ HS8 is considered in isolation the interaction effects between HS8 and HS9 are obvious and pertain only to the amplitudes of D_d/D_{sc}

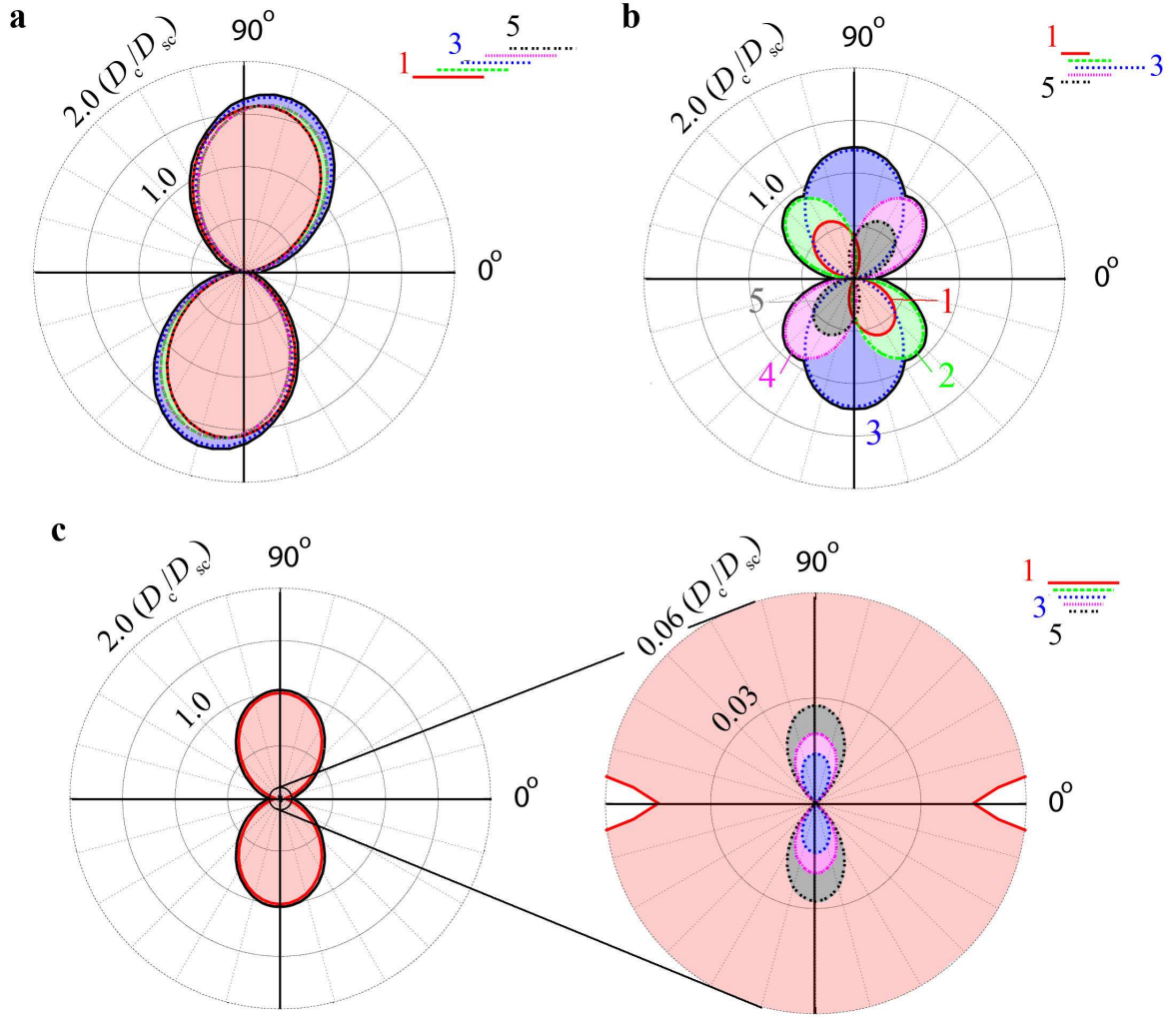


FIGURE 4.14: Directional sensitivities of three arrangements of five parallel slits with $S/l_0 = 0.04$. **a** An oblique bar formation with $\lambda/l_0 = 0.34$ is most sensitive to loads offset by some 10° from the normal direction. **b** For a heart shaped formation with $\lambda/l_0 = 0.4$ and $\Delta l/l_0 = 0.2$ the relative face displacements D_c vanish only for $\Phi = 0^\circ$, so that the array is sensitive to loads acting at directions between $\Phi = 10^\circ$ and 170° . **c** A triangular arrangement of slits with a linear gradation in slit length of $\Delta l/l_0 = 0.15$ is sensitive mainly to loads acting in the normal direction. The outer slits are markedly more sensitive than the inner ones. The envelopes of the responses are shown as bold solid lines. Note the different scaling of the axes in c.

of the slits 1 to 3 (Figs. 4.17a and a'). According to simulations using planar FE models the slits are most sensitive to uni-directional loads acting at angles between approximately $\Phi = 60^\circ$ and 135° . The amplitude ranges of both arrangements overlap as shown in Figs. 4.16b and c and cannot clearly be separated.

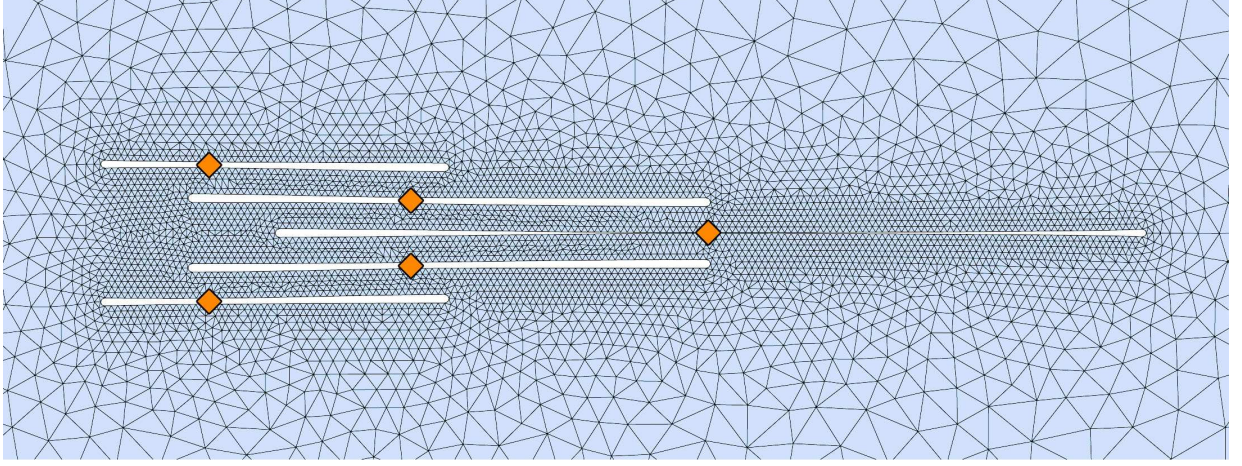


FIGURE 4.15: Deformed FE model of a heart shaped array with $S/l_0 = 0.04$, $\lambda/l_0 = 0.4$, $\Phi = 90^\circ$ and $\Delta l/l_0 = 0.2$. This arrangement results in maximum slit deformations that are not at the slits' mid-length positions. The displacements are scaled up by a factor of 10^4 . Positions of maximum slit face displacement are indicated by orange diamond shaped symbols.

Because organ HS8 is easily accessible to measurements and can be stimulated under controlled conditions results of interferometric measurements can be compared to FE data. Figure 4.18a shows the measured changes in slit width D_d in μm plotted against the deflection angle of the metatarsus in degrees for the seven slits composing the organ HS8. In Fig. 4.18b and b' examples of white light interferometric images are given. At a lateral force of 4 mN, which corresponds to a deflection of the metatarsus by $\Theta = 3.8^\circ$, the longest slit (slit1) is compressed by approximately 860 nm ($\approx 39\%$). When the load is further increased to 10 mN, which corresponds to a deflection angle Θ of 9.3° , even the shortest slit (slit7) in the arrangement is deformed by approximately 80 nm. For a deflection angle of 0.01° where the material behavior of the cuticle is linear and the deformation curves are in the linear regime, the sum of the slit deformations evaluated at the location of the dendrites is approximately 7.4 nm (Fig. 4.18a). With an estimated width of the organ of $\approx 100\ \mu\text{m}$ this gives a strain of 7.4×10^{-5} ($=74\ \mu\epsilon$). In the planar FE model of HS8 loaded by far field strains of $\epsilon_{a,r} = 2.5 \times 10^{-5}$ comparable strains at the location of the organ of approximately 4.49×10^{-5} ($=44.9\ \mu\epsilon$) occur. Under uni-axial loads at $\Phi \approx 111^\circ$ the model of the organ is most sensitive in resolving the amplitude of a load (Fig. 4.17a). When the results of the simulations evaluated at $\Phi \approx 111^\circ$ were scaled to the strains measured by

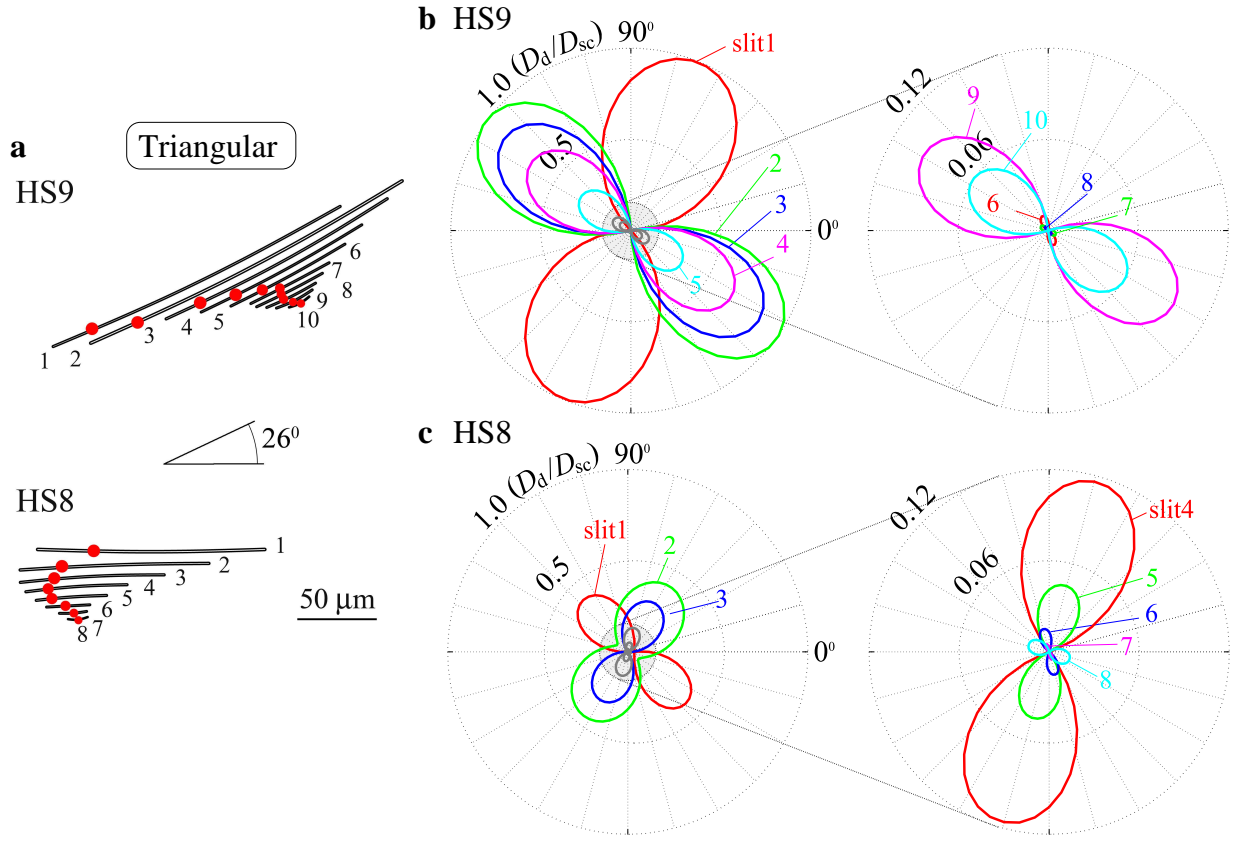


FIGURE 4.16: Directional sensitivities of two neighboring lyriform organs, HS8 and HS9 on the tibia of *C. salei*. **a** Models of the organs. Orientation and neighboring distance taken from SEM images. Red filled circles indicate locations of dendrites. **b** Directional responses of the slits of organ HS8 and **c** of organ HS9.

white light interferometry and to a slit length $l_0 = 120 \mu\text{m}$, i.e. to the length of the longest slit in HS8, as shown in Appendix B, the deformation of slit1 becomes approximately 2.75 nm. This is close to the value of 2.9 nm (difference 5%) measured in the actual organ (Fig. 4.19b). In addition, in the measurements and in the simulations the orderings of the slits in terms of magnitude of slit deformation are very similar to the ordering in slit length (Figs. 4.19a and b). This shows that the models used for FE analysis are well suited to estimating the deformations of real lyriform organs.

In Fig. 4.18b the deflection angle of the metatarsus closely approaches a linear dependence on the applied force. The measured slit face displacements evaluated at the deflection

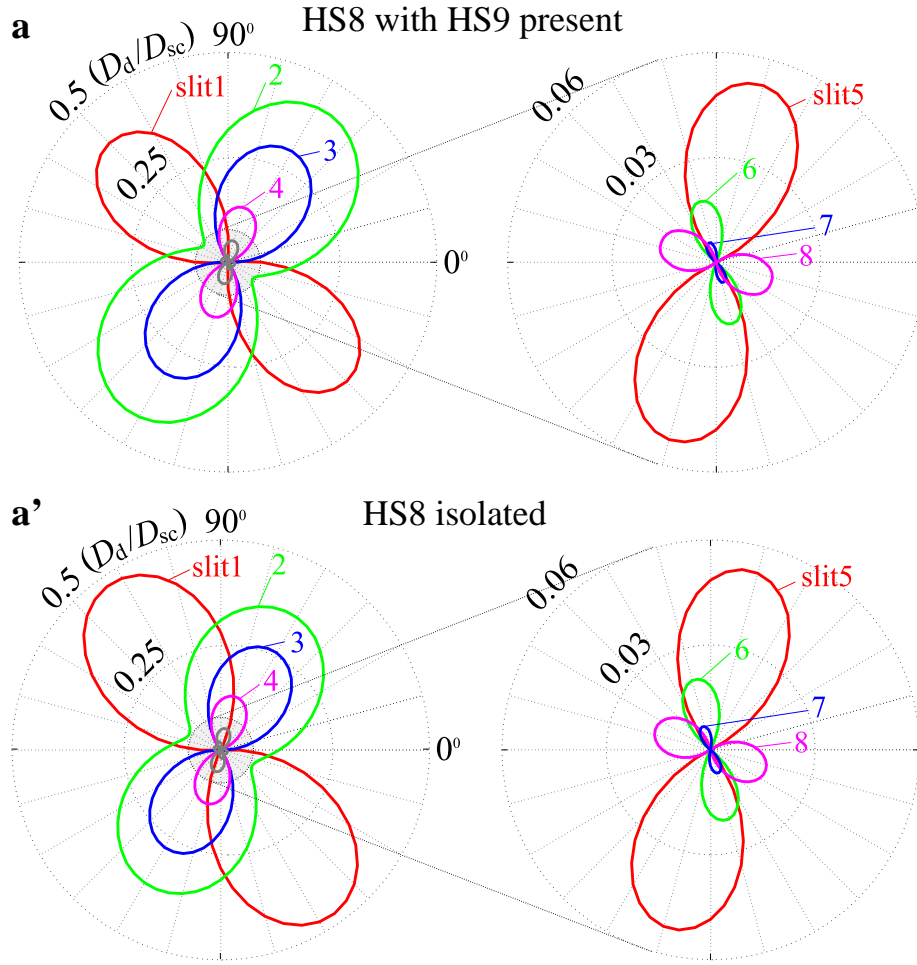


FIGURE 4.17: Comparison of the interaction effects of the organ HS9 on the organ HS8. **a** Response of the organ HS8 when the organ HS9 is present and **b** directional response when the organ HS8 is isolated.

angles (all below 1°) of the metatarsus corresponding to the threshold stimulus amplitudes eliciting an impulse response of the sensory cells measured electrophysiologically by Barth and Bohnenberger (1978) are ≈ 1.7 nm for slit2, ≈ 14 nm for slit3, ≈ 37 nm for slit4, ≈ 43 nm for slit5, and ≈ 10 nm for slit6 (see solid black circles in the detail of Fig. 4.18a). Surprisingly, the sensitivity of slit6 is higher than that of slit5.

White light interferometric measurements on the deformations of the slits were performed by C. Schaber in collaboration with S. Gorb and Prof. E. Arzt of the Max Planck In-

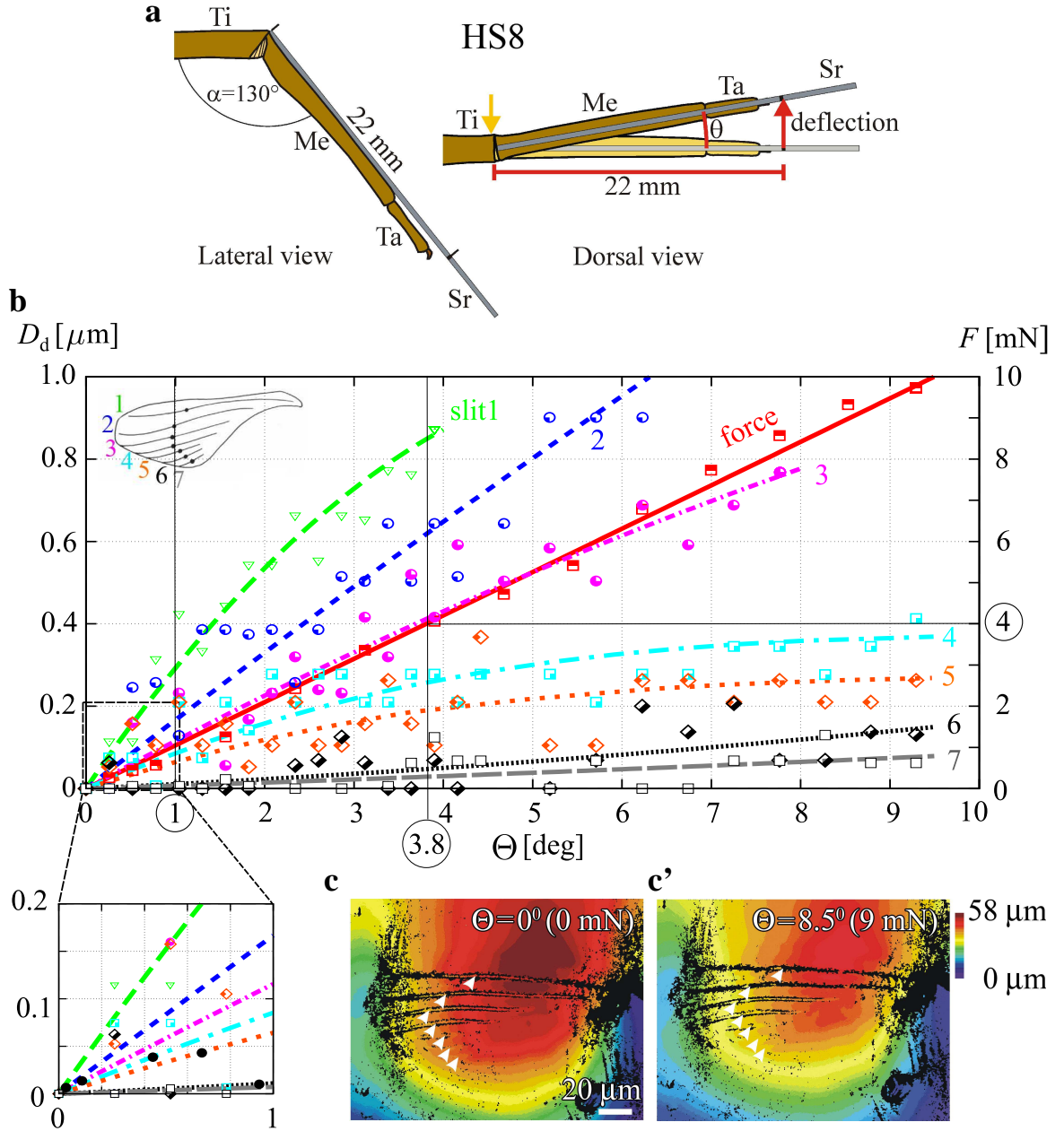


FIGURE 4.18: **a** Arrangement of the leg for white light interferometric examination of the deformation of lyriform organ HS8 and simultaneous force measurements. The angle between tibia (Ti) and metatarsus (Me) Θ is kept at 130° in the dorsoventral plane. A steel rod (Sr) waxed to the metatarsus dorsally serves to deflect it laterally against the fixed tibia. Yellow arrow points to location of lyriform organ HS8 on the posterior aspect of the tibia, which was scanned with the white light interferometer. **b** Measured slit deformation at the location of the dendrites D_d of the slits (white arrowheads in **c** and **c'**); experimental results are given as symbols, the lines are quadratic regression curves. Interferometry images in the undeformed (**c**) and deformed configuration at a deflection angle of the metatarsus of 8.5° (**c'**). The black dots in the detail of **b** indicate the deflection angles Θ for the electrophysiologically measured threshold stimulus amplitudes of the slits by Barth and Bohnenberger (1978). The color code pertains to the distance in out-of-plane direction at the position of the organ (Höbl et al., 2007b).

stitute for Metals Research in Stuttgart, Germany. The setup for the measurements is depicted in Fig. 4.18a and more detailed information on the soft- and hardware used in the measurements is given in Hößl et al. (2007b) and Schaber and Barth (in prep.).

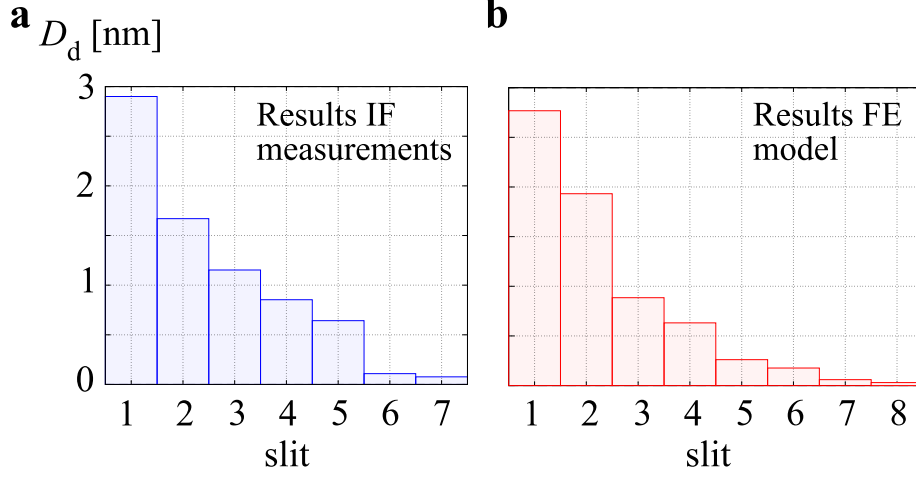


FIGURE 4.19: Absolute slit face displacements of the slits of organ HS8 in nm at a deflection angle of the metatarsus of 0.01° according to the interferometric (IF) measurement (a) and FE analysis (b) at $\Phi = 111^\circ$, $\varepsilon_{a,r} = 4.5 \times 10^{-5}$, and $l_0 = 120 \mu\text{m}$ (compare Fig.4.16).

4.1.3.2 Directional dependence of the deformation of natural slit patterns other than that of lyriform organ HS8

The mechanical responses of some basic simplified slit formations, e.g. oblique bar, triangular, and fan-like arrangements, were studied in Chapter 4.1.2. We now investigated models of lyriform organs showing the same basic arrangements of slits but also took the morphological details of the natural geometry into account. For the geometrical parameters describing the tested slit arrays see Fig. 4.5.

Oblique bar formations. In oblique bar formations the face deformations of the individual slits are very similar provided the slits are of equal length (Barth et al., 1984). A slightly simplified natural arrangement and a more realistic planar geometry based on the organ VS3 are shown in Figs. 4.20a and b, respectively. The organ was modeled with straight slits of equal width at longitudinal shifts of $\lambda/l_0 = 0, -0.29, -0.62, -0.86, -1.04, -1.15$, and

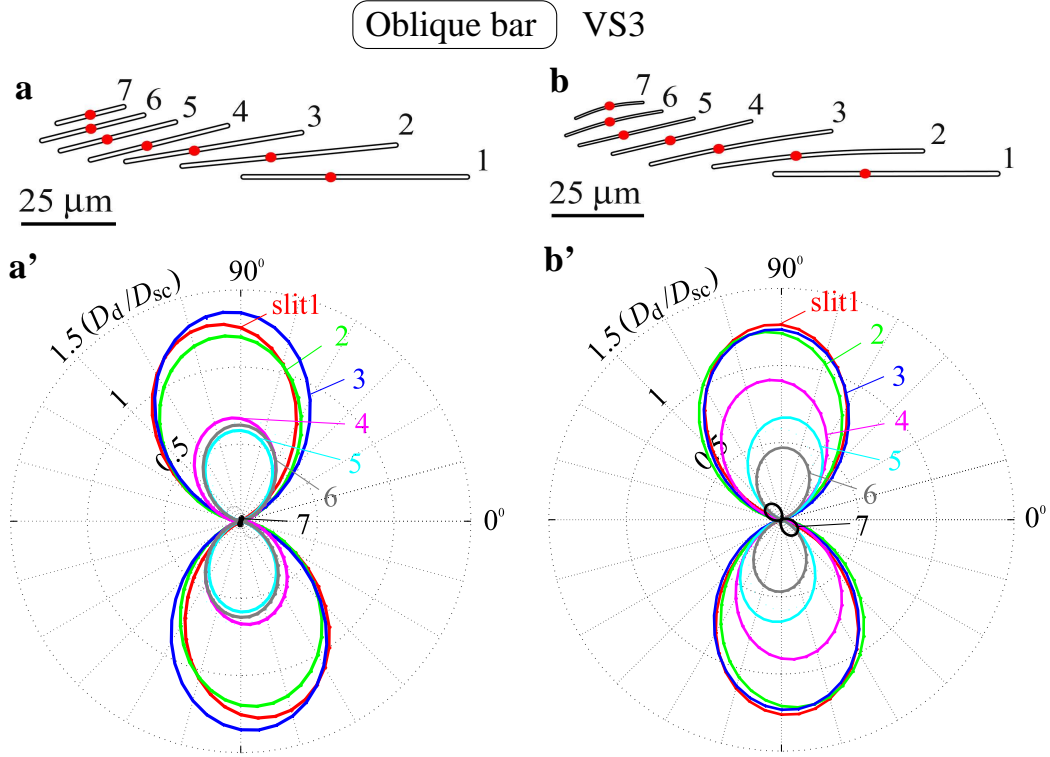


FIGURE 4.20: Directional sensitivity to uni-axial compressive far-field loads of two arrangements of slits based on organ VS3 on the patella of *C. salei*. **a** Simple model and **b** detailed model of the organ with the corresponding mechanical responses to loads from different directions (**a'**, **b'**).

-1.16 (Fig. 4.20a) and with slightly curved slits of varying widths at $\lambda/l_0 = 0, -0.3, -0.64, -0.9, -1.1, -1.2$, and -1.22 (Fig. 4.20b) corresponding to SEM images of VS3. The slit face displacements of individual slits show noticeable sensitivity to the changes in aspect ratio and shape of the centerline of the slits (Chapter 4.1.2.1). This indicates that minor variations in the longitudinal and lateral shift between the slits considerably influence the face deformations of the slits. Figures 4.20a' and b' compare the responses of corresponding arrangements. In contrast to findings presented in Chapter 4.1.2.5 where all five parallel slits of equal length respond to similar ranges of loads, in Fig. 4.20a' slit1 to slit3 and slit4 to slit6, respectively, show similar amplitudes of D_d/D_{sc} . When the morphology of the organ is modeled in more detail, i.e. C-shaped slits of varying width are used as depicted in Fig. 4.20b', slit4 to slit6 are no longer adjusted to similar load levels but the response is more evenly distributed in the range of the deformation amplitudes the entire

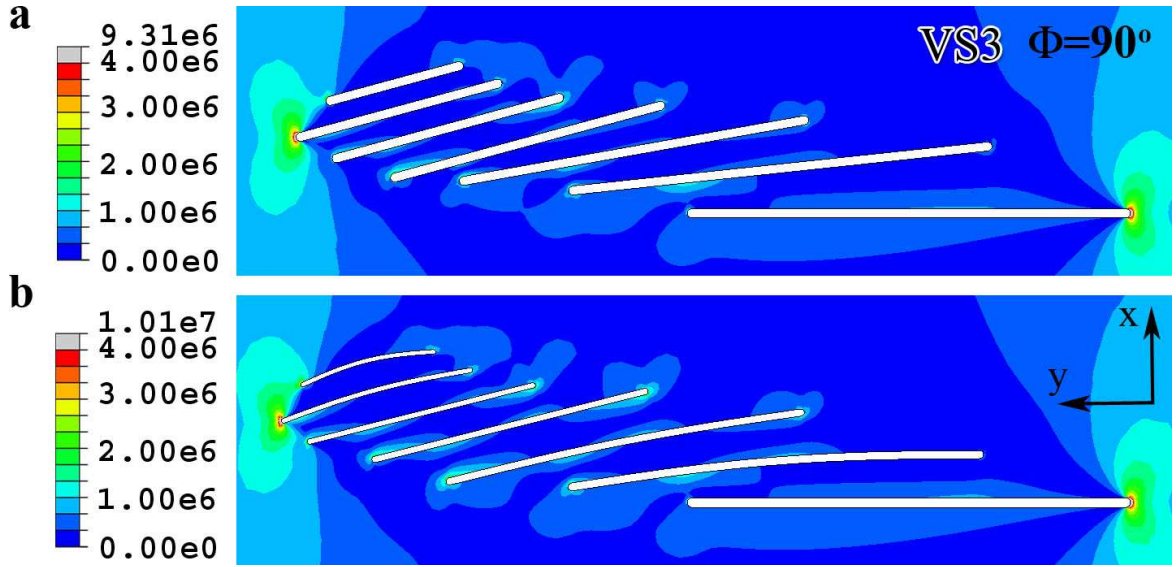


FIGURE 4.21: Von Mises stresses in the vicinity of slit formations based on organ VS3 under loads acting normally to their longitudinal direction ($\Phi = 90^\circ$). Slit formation in **a** as depicted in Fig. 4.20a and in **b** as depicted in Fig. 4.20b.

organ responds to. The similarities in the directional response are more clear when the equivalent stresses in the models are compared (Figs. 4.21 a and b). Small differences are mostly seen in the maximum stresses close to the tips of the slits in the modeled organs. In both arrays slit7 shows only small deformations, i.e. in real organs it sends signals to the central nervous system under very high load amplitudes only. This was expected because slit7 is arranged almost symmetrically ($\lambda = 0.01$) relative to its neighbor, slit6, and therefore heavily shielded (compare Figs. 4.21 a and b) similarly to the smallest slit in a symmetric triangular arrangement of five parallel slits at lateral distances between the slits of $S/l_0 = 0.04$ (Chapter 4.1.2.5).

Dendrite position. To relate the positions of the dendrites to the positions of the maximum slit face displacements, the deformations of the slit faces $D(x)/D_{sc}$ were plotted along the slits in Figs. 4.22a and b for the slit arrangement shown in Fig. 4.20b. In Fig. 4.22a the load direction is normal ($\Phi = 90^\circ$) to the longest slit, slit1, in the arrangement, which is similar to the load direction a single isolated slit is most sensitive to. In addition, in Fig. 4.22a' the results for $\Phi = 60^\circ$ are plotted to show the dependence of the deformation along the

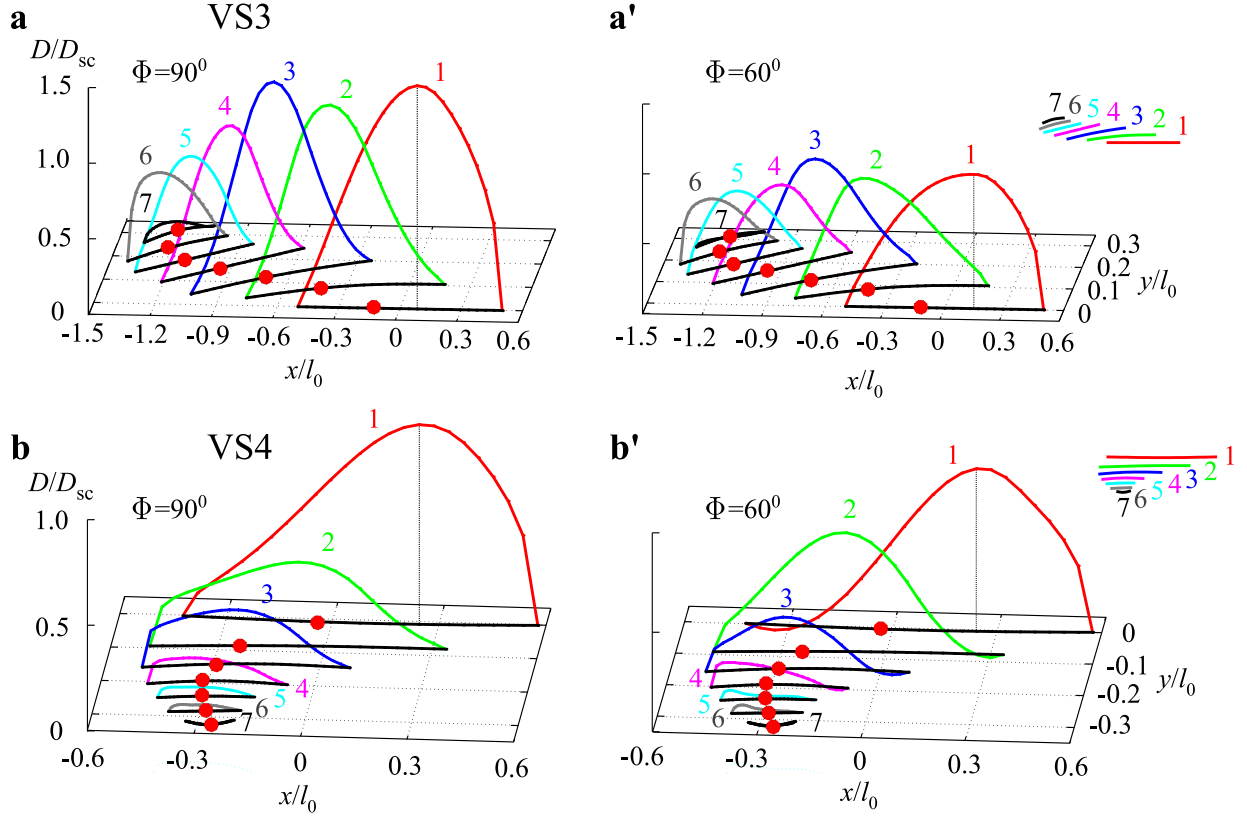


FIGURE 4.22: Slit face deformations $D(x)$ along the slits. **a, a'** Arrangements based on organ VS3 (Fig. 4.20b). Deformation maxima along the faces are close to the slits' midpoints for both loading directions, $\Phi = 90^\circ$ and $\Phi = 60^\circ$. **b, b'** Model based on organ VS4 (Fig. 4.23b). In slit2 the deformation increases but simultaneously decreases in slit1 when the load direction changes from $\Phi = 90^\circ$ to $\Phi = 60^\circ$. Note positions of the dendrites (red filled circles).

slits on the load direction. The amplitudes of $D(x)/D_{sc}$ change in a similar way in all slits and the positions of the maximum slit face deformations are shifted. For example, in slit2 of the model based on VS3 the distance between the center of the slit and the location of the maximum slit face displacement changes from $-0.11 l_0$ to $-0.19 l_0$ ($= 8\% \text{ of } l_0$) when the load direction changes from $\Phi = 90^\circ$ to 60° (Figs. 4.22a and a') which is due to the changed interaction effects when the load is rotated. Here a change in loading direction affects the amount in slit face displacement but not the results in terms of detection of different load levels. Similar changes are expected when the slit deformations along the slit faces are plotted for the model shown in Fig. 4.20a.

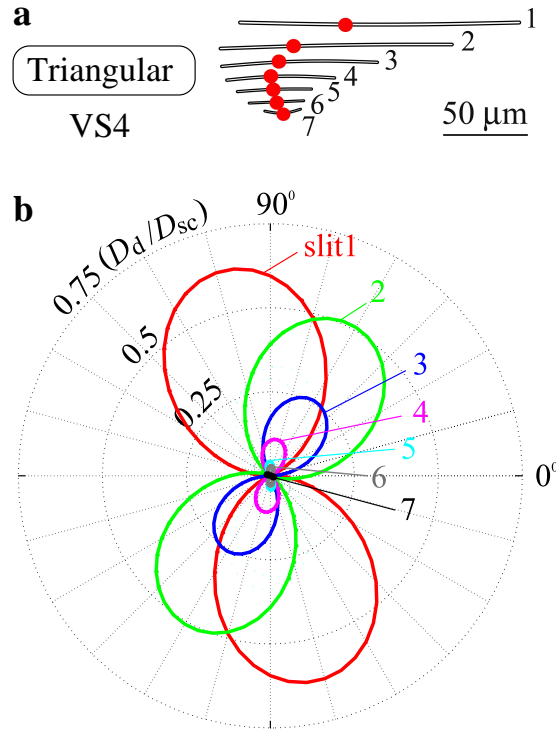


FIGURE 4.23: Directional mechanical sensitivity of slits arranged like in lyriform organ VS4 of *C. salei*. **a** 2D model and **b** mechanical response of slits to uni-axial compressive far-field loads.

Triangular slit arrangements. In triangular slit arrangements a longitudinal shift λ/l_0 (see Fig. 4.5f) is required to move the shorter slits out of the shielding zone of the outer longer slit. In real slit formations the slits indeed show a conspicuous tendency to be slightly shifted longitudinally as exemplified by the triangular arrangement VS4 (Fig. 4.23a). Here the length of slit1 is l_0 and that of slit2 is $0.84 l_0$ which in combination with a longitudinal shift of $\lambda/l_0 = 0.14$ moves the left tip of slit2 out of the shadow of slit1 by a distance of $0.06 l_0$. Close to $\Phi = 90^\circ$ the amplitude ranges of the deformations of the individual slits are more or less evenly distributed over the entire range of the organ's mechanical sensitivity (Fig. 4.23b).

The slits are most sensitive to uni-axial loads acting in directions between $\Phi = 60^\circ$ and 105° . In contrast to the model based on organ VS3, in the model of VS4 the amount of change in the slit face deformations along the slits is different in each slit when Φ is altered.

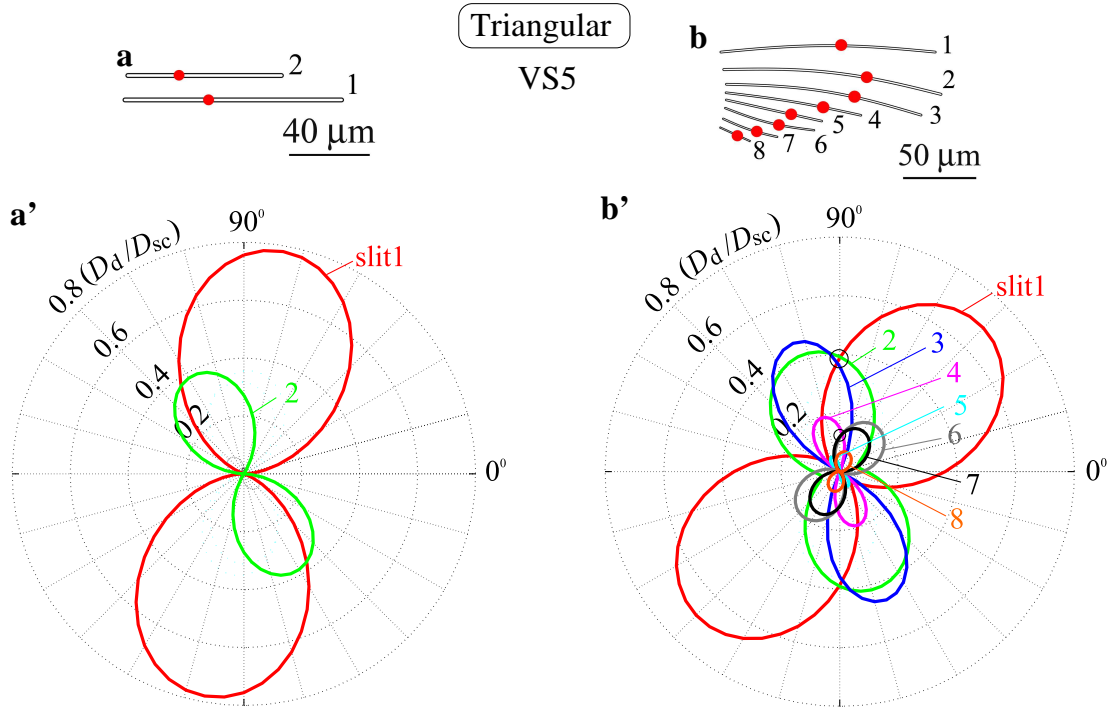


FIGURE 4.24: Comparison of models based on the organ VS5 of **a** *C. salei* and **b** the bird spider *Aphonopelma*. **a'** The slit face deformation of the smaller slit is 1/3 of the value for the longer slit at $\Phi = 90^\circ$. **b'** Slits 1, 2, and 3 on the one hand and slits 4, 6, and 7 on the other hand measure similar load levels at $\Phi = 90^\circ$ (black circles). The curves are evaluated at the locations of the dendrites (red filled circles).

Thus $D(x)/D_{sc}$ strongly increases in slit 2 and decreases in slit 1 when the load direction changes from $\Phi = 90^\circ$ to 60° . The change in positions of the maximum displacements along the slits between the load directions of $\Phi = 90^\circ$ and 60° measures less than approximately 2 % (Figs. 4.22b and b') which is smaller than in VS3. In arrangement VS4 even a small change in the load direction of a uni-axial stress influences the D_{ds} of the slits.

In a model representing organ VS5 of *C. salei* (Fig. 4.24a) at $\Phi = 90^\circ$ the slit face deformation at the dendrite of the longer slit is roughly three times the value of that of the shorter slit (Fig. 4.24a'). In the bird spider *Aphonopelma sp.* this organ has similar orientation and is located at the same position on the tibia. However, in contrast to that of *C. salei* it consists of some 8 slits that are arranged in a triangular pattern (Fig. 4.24b). According to the value for the slit deformations evaluated at $\Phi = 90^\circ$ the slits can be collected in two

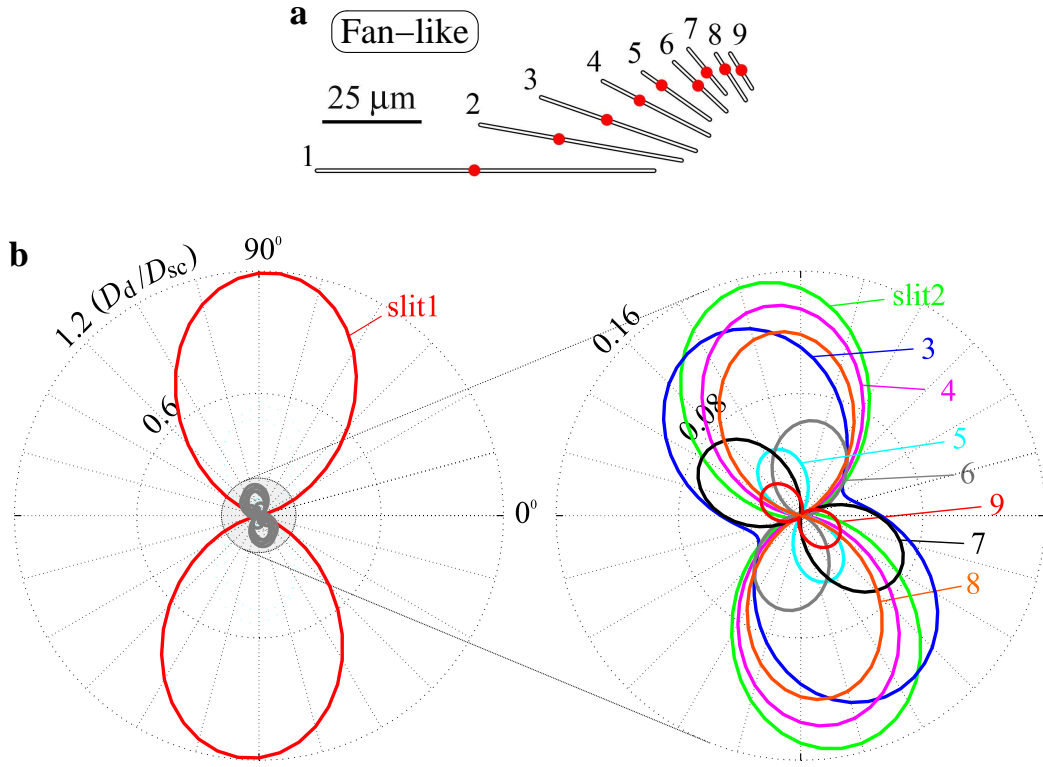


FIGURE 4.25: Model of a hybrid fan-like triangular slit pattern based on a lyriform organ on the chelicera of *C. salei*. **a** 2D model of the slits and **b** directional sensitivity to uni-axial compressive far-field loads.

groups (slit1, 2, and 3 versus slit4, 6, and 7) which show a ratio of slit face deformations of $1/3$ ($D_d/D_{sc} \approx 0.39$ and $D_d/D_{sc} \approx 0.13$ in Fig. 4.24b'), which is similar to VS5 in *C. salei*.

Fan-like slit patterns. Amplification and shielding effects determine the deformations in the model of a fan-like slit pattern based on a lyriform organ on the chelicera of *C. salei* (Fig. 4.25a). Accordingly, the D_d/D_{sc} value of the longest slit is 1.2 at a load direction of $\Phi = 90^\circ$ and that of the smaller slits is less than 0.16 at Φ between approximately 80° and 150° (Fig. 4.25b). This slit pattern is very directional for low or moderate loads, but approaches omni-directionality at high loads. Loads between $\Phi = 15^\circ$ and 30° are only resolved at high amplitudes ($D_d/D_{sc} = 0.055$), which is in contrast to the idealized fan-like slit arrangements presented in Chapter 4.1.2.4 and may be due to the graded slit lengths in the lyriform organ on the chelicera.

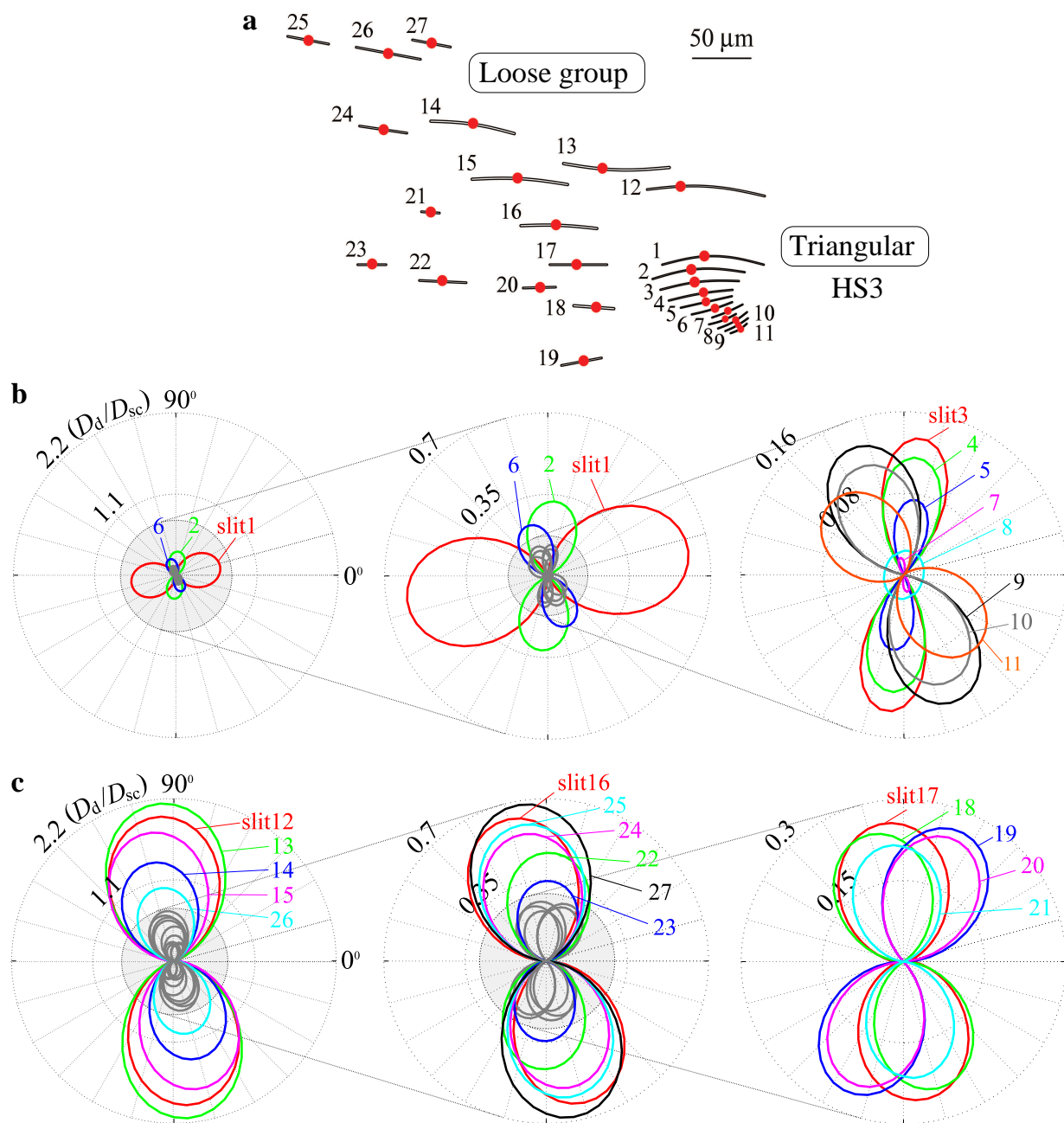


FIGURE 4.26: Interaction effects between the slits of a loose group and organ HS3 **a** on the coxa of *C. salei*. **b** Directional sensitivity of the organ HS3 and **c** of the slits belonging to the loose group. The overall response is approximately uni-directional with the exception of slit1 in HS3.

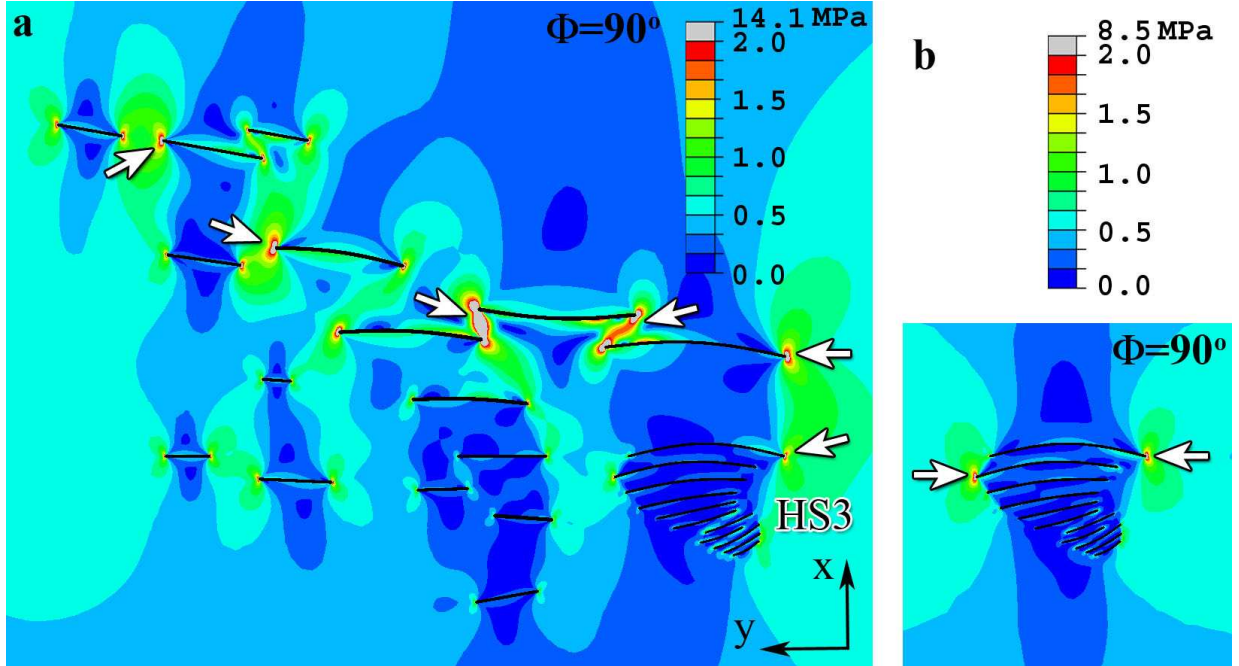


FIGURE 4.27: Von Mises stresses in MPa in the vicinity of lyriform organ HS3 of *C. salei* loaded by uni-directional stresses at $\Phi = 90^\circ$. **a** Loose group of slits in close neighborhood of HS3 and **b** isolated slit sensillum HS3. Note that in the isolated organ the maximum stress concentration factor (SCF) is 19 and therefore lower than in an isolated slit of aspect ratio 100 (SCF=21.9) and in the entire arrangement including the loose group (SCF=31). The white arrows point to the regions of high stresses.

4.1.3.3 Interactions between a lyriform organ and a closely positioned group of slits

At the beginning of this section we investigated two interacting lyriform organs. Now we ask for the interaction effects between a lyriform organ and a loose group of slits. Due to its closeness the loose group of slits found next to the triangular lyriform organ HS3 of *C. salei* interacts with this organ (see Fig. 4.26; closest longitudinal distance between the organ and the slits of the loose group $0.3 l_0$; closest lateral distance $0.6 l_0$). Here the working range of the lyriform organ is supplemented by the working range of the loose group of slits close to it. The maximum slit face deformation in the loose group, in slit13, is approximately 3.5 times larger than that of the longest slit, slit1, of the lyriform organ due to interaction effects, i.e. amplification of the slit face displacements, between the

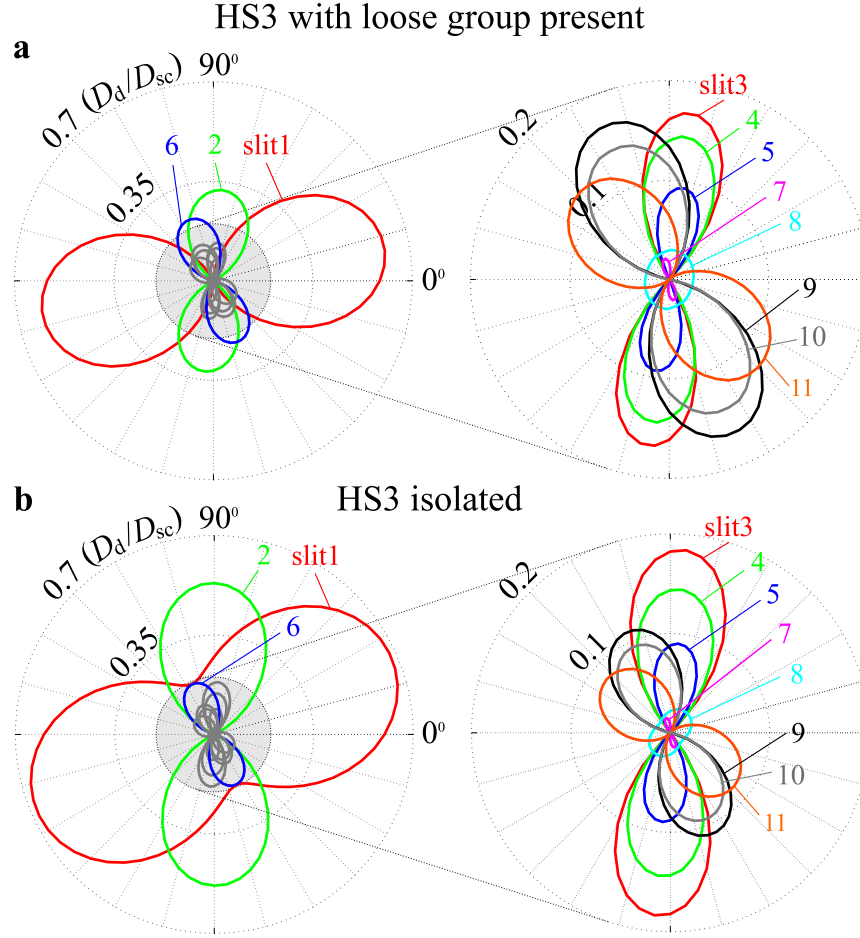


FIGURE 4.28: Comparison of the interaction effects of the loose group of slits on the slit arrangement based on the organ HS3 (compare Figs. 4.26a and b). **a** Directional response of the slits of HS3 when the loose group is present. **b** Slit1 shows omnidirectionality when the organ HS3 is isolated. The directional sensitivities of slit1, slit2, and slit8 change as well as the thresholds for all slits.

slits. This is also reflected in the maximum stress concentration factor of approximately 29 ($SCF = \text{local maximum stress} / \text{far field stress}$), compare ≈ 21.9 for a single isolated slit of aspect ratio 100, in the vicinity of the ends of the slits which is evident in fringe plots of the Von Mises stresses (Fig. 4.27a). Here regions with high stresses are colored red and regions of low stresses are colored blue. As load levels increase, at first the slits of the loose group respond (Fig. 4.26c), followed by the slits of the lyriiform organ (Fig. 4.26b). The response of this arrangement is highly directional due to the slits of the loose group, i.e.

the highest sensitivities of the slits of the loose group are found at load directions close to 90° . At high loads a fine resolution of the load direction between $\Phi = 60^\circ$ and 120° can be obtained by the organ HS3. At $\Phi = 90^\circ$ slit1 is shielded by the other slits in the arrangement (compare Fig. 4.27b) similar to findings in the organ VS5 of the bird spider (Figs. 4.24b and b'). Slit1 in HS3, in contrast to the remaining slits of the organ, is most sensitive at $\Phi \approx 10^\circ$ which is in principle similar to findings for the organs HS8 and HS9 (Figs. 4.16b and c). A somehow different “wiring”, i.e. slit1 may operate as a trigger for the onset of the load, may also be indicated by electrophysiological measurements of the stimulus amplitudes of the slits of the organ HS8 of *C. salei* (Barth and Bohnenberger, 1978), where it was difficult to measure the activity of slit1 because of its high sensitivity.

The interaction between the loose group and the lyriform organ is clearly seen when comparing the response of the lyriform organ (slit1 to slit11) in the presence (Fig. 4.27a and Fig. 4.28a) and absence (Fig. 4.27b and Fig. 4.28b) of the loose group (slit12 to slit27). The amplitudes of D_d/D_{sc} , the directions of maximum sensitivity, and also the order of the slits in terms of maximum mechanical sensitivity in the slit pattern change when the organ is studied without the loose group. Remarkably, slit1 has a more omnidirectional response when the organ HS3 is isolated because it is not shielded by the slits of the loose group close to $\Phi = 90^\circ$. Note that the stress concentration factors (SCF=local maximum stress/far field stress) evaluated at the ends of the slits strongly depend on the interaction effects between the slits, i.e. there is a maximum $SCF \approx 29$ (slit13) for the formation depicted in Fig. 4.27a and a maximum $SCF \approx 17$ (slit1) for the isolated lyriform organ shown in Fig. 4.27b.

4.2 Discussion

The normalized results presented in the figures of this chapter can be adapted to any configuration by scaling with appropriate values of l_0 , the far field strain ε_a , or the far-field stress σ_a for cracks or slits, on which D depends linearly. An example of this procedure is presented in Appendix B.

4.2.1 Analytical models using Kachanov's method

4.2.1.1 Lateral crack spacing

Kachanov's method predicts that in arrangements of five parallel cracks with increasing lateral crack spacing S/l_0 starting from 0.5 shielding and amplification rapidly decrease (Figs. 4.3a and 4.3b). The effects of crack interaction are fairly small at $S/l_0 = 1.5$ and the D_c of a non-interacting single crack given e.g. in Hahn (1976) is closely approximated at $S/l_0 = 3$. These results support the idea that interaction effects play no appreciable role in the mechanical response of isolated slits as defined in section 2.2, but must be accounted for when studying loose groups of slits.

4.2.1.2 Oblique bar arrangements

According to experimental studies arrays of longitudinally staggered slits like those in Fig. 4.4a, which are referred to as oblique bar formations by Barth et al. (1984), give rise to geometrically similar distributions of the face deformations in all slits. It was proposed that such arrangements can be interpreted as potentially allowing an improvement of the signal-to-noise ratio by central nervous convergence of the signals (Barth et al., 1984). Applying Kachanov's method to arrays of five parallel cracks of equal length it was found that geometrical similarity of the D s of the individual cracks can be closely approached by staggering them by a constant distance of $\lambda/l_0 = 0.5$ (Figs. 4.3c and 4.3d). For shifts smaller or larger than $0.5l_0$ the D s of the three inner slits remain similar, but those of the two outermost slits clearly differ. For arrangements of five parallel slits with lateral spacings

of $S/l_0 = 0.5$, when λ/l_0 exceeds a value of approximately 0.35, the maximum D s in all slits exceed the exact result for a single crack (Hahn, 1976), i.e., there is amplification. Sensilla that approximate this type of arrangement can indeed be found in arachnids (Fig. 2.1e).

It is interesting to note that some spider lyriform organs, like the lyriform organ VS3 on the patella of the walking leg of *C. salei*, (Fig. 4.4a), are superficially similar to the above oblique bar formation. However, according to scanning micrographs the neighboring slits of VS3 are shifted longitudinally by about $0.35 l_0$, differ in slit length, and vary slightly in their orientation and the position of the slits' dendritic endings. Accordingly, the configuration differs significantly from the one predicted under the assumption of maximum redundancy (all cracks show similar values of opening displacements) by Kachanov's approach. These differences may be due to the much closer transverse spacing of the slits in VS3, or may reflect somewhat different "design goals".

4.2.1.3 Triangular and "bell shaped" arrangements

When the lengths of neighboring slits within an array differ by a constant increment Δl , the longest crack shows the largest and the shortest crack the smallest D s, respectively (Figs. 4.3e and 4.3f). Accordingly, if sensors sensitive to a given range of face displacements are placed in the slits, a triangular arrangements of slits can respond to a considerably larger range of inputs than an individual slit. For arrays of five parallel slits with lateral spacings of $S = 0.5 l_0$ this effect becomes marked for $\Delta l \gtrsim 0.15$. The predicted opening distances agree well with experimental observations on more closely spaced slits in model systems (Barth et al., 1984).

When Kachanov's method was used for identifying symmetrical triangular arrangements of five parallel slits with D_c s that correlate with electrophysiologically measured threshold stimulus amplitudes of spider lyriform organ HS8 (Fig. 4.4b) (Barth and Bohnenberger, 1978), a sequence of crack lengths of l_0 , $0.9 l_0$, $0.56 l_0$, $0.3 l_0$, and $0.18 l_0$ was obtained (Fig. 4.29a). Here the first two slits are of almost equal length on account of the shielding effect, whereas the lengths of the subsequent slits decrease more and more rapidly. Skewed triangular arrangements of slits can be obtained by shifting the slits longitudinally. The resulting sequences of opening distances at the slits' centers do not change appreciably

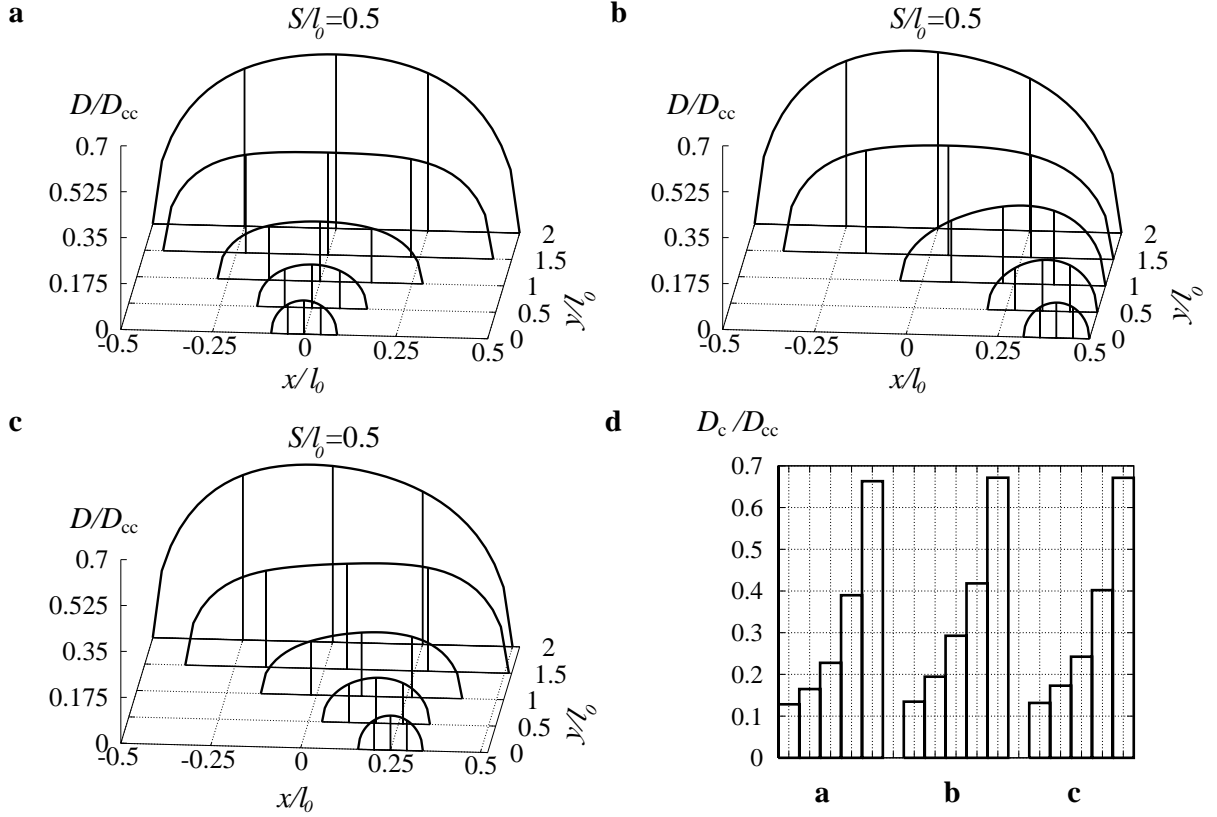


FIGURE 4.29: Arrangements of cracks with lateral spacings $S/l_0 = 0.5$ (where l_0 is the length of the longest crack in the array) as simplified models of triangular arrangements of slits. (a) Symmetric arrangement giving non-linear gradation of crack D s, (b) arrangement with all cracks aligned at the right ends and (c) intermediate geometry giving maximum crack D s similar to (a). (d) Bar diagrams of the normalized D s at the centers (D_c/D_{cc}) of the five cracks of arrangements (a), (b), and (c).

(Fig. 4.29d). However, the positions of the maximum D s within the individual slits are shifted (Figs. 4.29b and 4.29c).

The above sequence of slit lengths leads to “bell shaped” sensilla. Even though the above models employ a lateral spacing of $S = 0.5l_0$ the outlines of the arrangements are in good qualitative agreement with that of the lyriform organ HS8 of *C. salei* (Fig. 4.4b).

4.2.2 Planar FE models of generic slit arrays

Even though the models discussed in the present chapter are geometrically relatively simple planar arrangements of slits and the exact 3D morphology of the slits and of the cuticle surrounding them are not taken into account, characteristic features can be investigated and valuable conclusions can be drawn from the results obtained. The main features found are in good agreement with expectations derived from the biological view and discussed in the following. In addition the results clearly demonstrate the potential of different slit arrangements with respect to engineering applications to strain sensors.

4.2.2.1 Dendrite positions in arachnid lyriform organs

In arrangements of slits that are not symmetric about the transverse axis, like the arrays shown in Fig. 4.5f and h, the locations of the maximum slit face displacements in general do not coincide with the mid-length positions (Fig. 4.13). To be consistent throughout this chapter we decided to compare the slit face displacements at the slits' centers by default, exceptions being explicitly marked. Checking the load direction dependent locations of the maximum values of D , however, provides important information towards explaining the configurations of real lyriform organs. The discussion of the results obtained for slit face displacements at the actual site of the dendrites in lyriform organs is presented in Chapter 4.2.3.

The dendrites' locations in a fan-type arrangement (see red filled circular markers in Fig. 4.13) on the chelicerae of *C. salei* with $\alpha \approx 90^\circ$ (see Barth and Libera (1970)) are close to the positions of the calculated maximum slit face displacements in the simplified FE models (Fig. 4.13a and b), provided only slits with marked compressive face displacements are considered. In the lyriform organ VS3 on the patella of *C. salei* (see schematic drawing in Barth and Libera (1970) and SEM images in Müllan (2005)), where the slits are arranged in an oblique bar pattern, however, the dendrites are not located at the positions of the maximum slit face displacements predicted by the present simplified model (Fig. 4.13b). For the largest slit in organ VS3 the difference in position is approximately $0.29 l_0$ for $\Phi = 120^\circ$, which is probably due to the gradation of the slit lengths ($l_0, 0.94 l_0, 0.823 l_0, 0.642 l_0, 0.531 l_0, 0.447 l_0, 0.314 l_0$) and the different orientations ($0^\circ, 4.5^\circ, 11^\circ, 14^\circ$,

14°, 15°, 14°) of the slits found in organ VS3. This lyriform organ appears to combine aspects of the geometry and deformation of oblique bar and triangular arrays. In a heart shaped array such as the lyriform organ HS2 on the trochanter of *C. salei*, the dendrites are not located at the mid-lengths of the slits, either, but are shifted proximally (towards the left in Fig. 4.5h) (Barth and Libera, 1970). These locations are close to the positions of the calculated maximum slit face displacements, with the exception of the center slit in the corresponding model (Fig. 4.13c).

The above examples indicate that the positions of the maximum slit face displacements depend on the loading direction. They do not necessarily coincide with the locations of the dendrites, although they are mostly close to them, which is in agreement with Barth et al. (1984). Possibly, the sites of the dendritic endings are related to the function of the organ, e.g. measuring the load direction or extending the stimulus amplitude ranges. Changing the positions of the dendrites may provide a further way of tuning the response of slit sensilla, in addition to adapting the lengths and orientations of the slits.

4.2.2.2 Single slits

Sensilla consisting of single, noninteracting slits are best suited for detecting compressive uni-axial stresses that act normal to the slits' axes (Barth et al., 1984). The primary geometrical parameter for adjusting the slit face displacements is the slits' length l , which (under the assumption of linear material behavior) linearly scales D and, consequently D_c . Changing the aspect ratio of straight slits, l_0/w_0 , from 20 to 100 decreases D_c/D_{sc} from 1.026 to 1 (Fig. 4.6b). Remarkably, in this context the aspect ratio of slits plays a minor role at best.

Slits of capped rectangular shape form larger holes in the cuticle compared to elliptical openings of the same length and aspect ratio (Fig. 4.6b'). The normalized difference in area, $\Delta A/l_0^2 = (A_{\text{slit}} - A_{\text{ell}})/l_0^2$, has its maximum at $l_0/w_0 = 2$. Evaluating the difference in slit face deformations gives a maximum value of $D_c/D_{sc} \approx 2.6\%$ that occurs at $l_0/w_0 \approx 2.5$ (Fig. 4.6b). This shows that the response is a nonlinear function of the slit area and is also influenced by the slit shape, though to a lesser extent. The latter effect is negligible at the high aspect ratios typically pertinent to arachnid slit sensilla. The campaniform sensilla

of insects, however, which have evolved low aspect ratios of $l_0/w_0 \approx 2$ to 3 (Barth, 1981), tend to be elliptical, which may indicate selection for openings of smaller area that weaken the cuticle to a lesser extent than openings of capped rectangular shape on the basis of similar aspect ratios.

Curved slit geometries, such as C-shaped and S-shaped slits lead to a reduction in the relative slit face displacements under loads acting at $\Phi = 90^\circ$ for equal slit lengths, because the projected slit lengths l_p decrease with increasing B (Fig. 4.6c). In the case of a C-shaped slit with $B = 0.25 l_0$ the decrease in D_c amounts to some 15%. The maximum sensitivity of C-shaped slits to uni-axial stresses, like that of straight slits, is predicted to occur at normal orientation. For S-shaped slits, in contrast, the direction of maximum sensitivity depends on the shape parameter B . For example, for $B = 0.25 l_0$ S-shaped slits are most sensitive to uni-axial loads acting at $\Phi = 140^\circ$ (Fig. 4.11), and their maximum sensitivity is about 13% smaller than that of a straight slit of equal length. Apparently, a given orientation of the maximum mechanical sensitivity of a single slit can be either achieved by orienting a straight slit normal to the load direction or by using a suitable value for B/l_0 for an S-shaped slit. Due to their lower sensitivity, S-shaped slits are less efficient in terms of slit area compared to straight ones and, accordingly, are rarely found. Examples of C-shaped and S-shaped slits occur e.g. within lyriform organ HS1 on the coxa of *Cupiennius salei* (Fig. 2.3b).

4.2.2.3 Arrangements of five slits

A striking feature of arachnid slit sensilla is the occurrence of a rich variety of arrays of mechanically interacting slits referred to as lyriform organs. By changing the lateral distances S between slits, by offsetting them longitudinally by λ , or by grading their lengths by Δl , considerable amplification or shielding of the relative face displacements of the individual slits can be achieved. Furthermore, by varying the geometrical parameters characterizing the arrangements widely differing or nearly equal responses of the individual slits can be produced, as well as a wide range of intermediate behaviors Barth et al. (1984). In the present study the Finite Element Method allowed us to evaluate on a quantitative basis the effect of geometrical parameters on the deformation behavior of different slit arrangements. This opens up the possibility of parametric studies explaining

the evolutionary adjustments of the arrangement geometries towards fulfilling a measuring task such as sensing load directions with different sensitivities in different directions.

Under the assumption that the membranes at the outside and the bottom of the slits as well as the liquid within the slits do not markedly influence their behavior, non-staggered arrays of parallel slits tend to show marked bending of the cuticular ligaments between the outermost slits, which leads to dilatation of the inner slits for lateral spacings $S/l_0 \lesssim 0.1$. In many lyriform organs the ligaments are shortened by staggering the individual slits and/or by a gradation of the slit lengths, so that ligament bending plays a lesser role.

If the purpose of organ VS3 on the patella, which is of the oblique bar configuration, is to measure similar levels of loads with all slits in the arrangement to increase the signal-to-noise ratio, the evolutionary strategy would be to increase the length of the smaller slits so that all slits in the array have the same length l_0 .

Arrangements with cascades of widely differing mechanical responses of the individual slits, e.g., organs of triangular type, appear to be aimed at maximizing the range of loads strengths that can be detected. As is shown in 4.9c shielding is the dominant interaction effect in triangular arrangements, which is the reason why slit 2 in the simplified model is never compressed. From electrophysiologically measured response thresholds and stimulus amplitude ranges of the lyriform organ HS8 on the tibia of spiders (Barth and Bohnenberger, 1978) we know, however, that all slits in this triangular formation are compressed and active. A closer inspection shows that in organ HS8 the first two slits are longitudinally shifted by $\lambda \approx 0.2 l_0$, which decreases the shielding effects on slit 2. Nonlinear gradations of slit lengths and longitudinal shifts between slits are, in fact, common in lyriform organs and are an important means of controlling shielding effects and thus the sensitivity of individual slits.

Lyriform organs of fan-like or heart shaped configurations achieve directional sensitivity over a wide range of loading angles. The former type of arrangement is essentially omnidirectional, whereas the latter appears to be more suitable for confined spaces and to cases where loads acting in parallel to the slits, i.e. at $\Phi = 0^\circ$, are of minor or no importance. Spider legs may be viewed as cylindrical shells with stiffened ends. As suggested by the location of lyriform organs strains caused by loads that are transferred by the articular

condyles between the leg segments are typically measured close to the condyles or at the stiffening rings along the circumference of the leg. In the latter case the stiffening rings are made more compliant by slits running parallel to the leg's longitudinal axis concentrating the strains at the positions of the slits. As a consequence, a higher sensitivity to changes of the segment's cross section, i.e. its ovalization, can be achieved. If strains have to be measured close to the condyles, at locations where there is no interruption of a stiffening ring by the slits (and no strain concentration due to this effect), the omnidirectionality of fan-like slit arrangements can be used to advantage. Accordingly, the "choice" between these types of organ depends on the given location and the configuration of the exoskeleton at this location. Remarkably, under uni-directional loads, fan-like arrays of slits are also suitable for measuring different load levels similar to triangular slit arrangements.

In technical applications strain gauges are employed in rosette arrangements of three gauges at angles of 45° , 60° , or 120° in order to measure all in-plane components of the strain tensor at a given position. Slits, in contrast to typical usage of strain gauges, noticeably influence the strain fields in their vicinity and thus give rise to shielding or amplification effects. Fan-type arrangements of slits as shown in Figs. 4.12c and 4.12d with $\alpha = 180^\circ$, corresponding to 45° rosette of strain gauges, appear to be well suited for analogous measurements. Even more potential in technical applications might lie in the development of bio-inspired strain sensors for micro and nano devices.

4.2.3 Planar FE models of slit arrays imitating lyriform organs

4.2.3.1 Comparing models with properties of original lyriform organ HS8

A comparison between the results of the simulations, the interferometric measurements of the slits' face displacements of the organ HS8 of *C. salei*, and the electrophysiological results presented by Barth and Bohnenberger (1978) shows a number of important agreements underlining the significance of the FE models. (i) In the simulations the amount of maximum slit deformation found in the organ in the longest slit, slit1, is in good agreement with the interferometrically measured value (only 5 % difference). (ii) In addition the order of the slits in terms of threshold stimulus amplitudes eliciting action potentials

corresponds to the order of the magnitudes of slit face displacements (Fig. 4.19).

The threshold stimulus amplitudes reported in the latter work correspond to slit face displacements of ≈ 43 nm (slit4) or less. For the most sensitive slit analyzed electrophysiologically in HS8, slit2, the physiologically effective threshold stimulus amplitude corresponds to a slit deformation of approximately 1.7 nm. This is close to 3 nm which was estimated for slit1 by Blickhan (1983) for natural loads resulting in strains of 1.4×10^{-5} ($=14\mu\varepsilon$) at the location of the organ during slow locomotion measured in live spiders. In our FE-simulations we found a slit face deformation of 1.7 nm of slit2 ($D_{sc} = 8.6$ nm) at $\Phi \approx 111^\circ$ for an applied uni-axial far field strain of 1.8×10^{-5} ($=18 \mu\varepsilon$) which is also well within the range measured by Blickhan and Barth (1985). According to recent micromechanical studies (Schaber and Barth, in prep.) on spider trichobothria, which are sensors responding to airflow, the deflection of the hair shaft at the site of stimulus transduction is about 6 nm/ $^\circ$ at a physiologically effective threshold hair deflection of 0.01° (Barth and Höller, 1999). The value found for spiders is very similar to those pertinent to insects (Gnatzy and Tautz, 1980; Thurm, 1982). The larger values now found for the slit sensilla may well be explained by the fact that the coupling cylinder “gears” down the deformation of the slits (Barth, 2002a).

Blickhan (1986) reported a nonlinear and hysteretic relationship between the force applied at the tip of the metatarsus and its angle of deflection (maximum angle approximately 20°), whereas Fig. 4.18 shows a linear response. This difference is probably due to the visco-elastic material behavior of the cuticle and the fact that Blickhan (1986) used cyclic loads whereas the measurements underlying Fig. 4.18 were quasistatic. The present FE models pertain to the small deflection part of Fig. 4.18, in which the deflection angles Θ are less than 1° , where nonlinear effects play a negligible role in the measurements.

4.2.3.2 Simple, generalized and more realistic slit patterns

Generalized patterns. The generalized patterns of lyriform slit sense organs are: (i) oblique bar formation with slits of equal length that are laterally shifted and are sensitive to the same amplitude and directional range of loads and with the potential to increase the signal to noise ratio by central nervous convergence of the nervous signals of the individual slits;

(ii) triangular patterns with slits of different length with the potential of considerably increasing the amplitude range of a single slit; (iii) heart shaped or fan-like arrangements with the potential of sensing the load direction on the basis of varying patterns of the slits active in the array (Barth et al., 1984).

Realistic patterns. Morphologically, organ VS3 of *C. salei* is a hybrid between an oblique bar and a triangular formation. Slits 1 to 3 mechanically respond to the same range of load amplitudes whereas the remaining shorter slits gradually increase the organ's mechanical working range (Fig. 4.20b). Remarkably, the interaction effects of slit7 are limited to slit6 in this arrangement (Fig. 4.30), i.e. when slit7 is removed only slit6 increases its slit face displacement.

For slits spaced as closely as in actual lyriform organs ($S/l_0 = 0.04$) symmetric triangular arrangements cannot be used to measure different evenly distributed ranges of loads because the shorter slits are strongly shielded by the longest slit (compare Chapter 4.1.2.5). Such arrangements may only be used when they are designed for an extremely high range of sensitivity to loads of two orders of magnitude (Höbl et al., 2007a). However, a longitudinal shift between the largest slit and its neighbor is a prominent feature of most arachnid lyriform organs. Organ VS4 represents such an arrangement and its intrinsic asymmetry (Fig. 4.23a). At $\Phi = 90^\circ$ the difference in magnitude of load necessary for stimulating further slits decreases with increasing load level (Fig. 4.23b).

Another triangular lyriform organ, organ VS5, consists of only two slits in *C. salei* (Fig. 4.24a) and of eight slits in the bird spider *Aphonopelma* (Fig. 4.24b). Again, the symmetry of the arrangement has to be broken so that the shorter slits are deformed (Fig. 4.24a'). From *in vivo* measurements of the strains occurring at the location of lyriform organ VS5 of *Aphonopelma* during locomotion (Blickhan and Barth, 1985) we know that it is stimulated during the stem phase, i.e., when the body is lifted, and therefore possibly measures the increasing hemolymph pressure (up to 50 kPa (Blickhan and Barth, 1985)) used to extend the legs at the tibia-metatarsus joint.

Interestingly, the organs of both spiders are sensitive in two load ranges ($D_d/D_{sc} = 0.76$ and $D_d/D_{sc} = 0.27$ in *C. salei*; $D_d/D_{sc} \approx 0.39$ and $D_d/D_{sc} \approx 0.13$ in *Aphonopelma*) at $\Phi = 90^\circ$ with a ratio of slit face deformation of roughly 1/3. Remarkably, a triangular

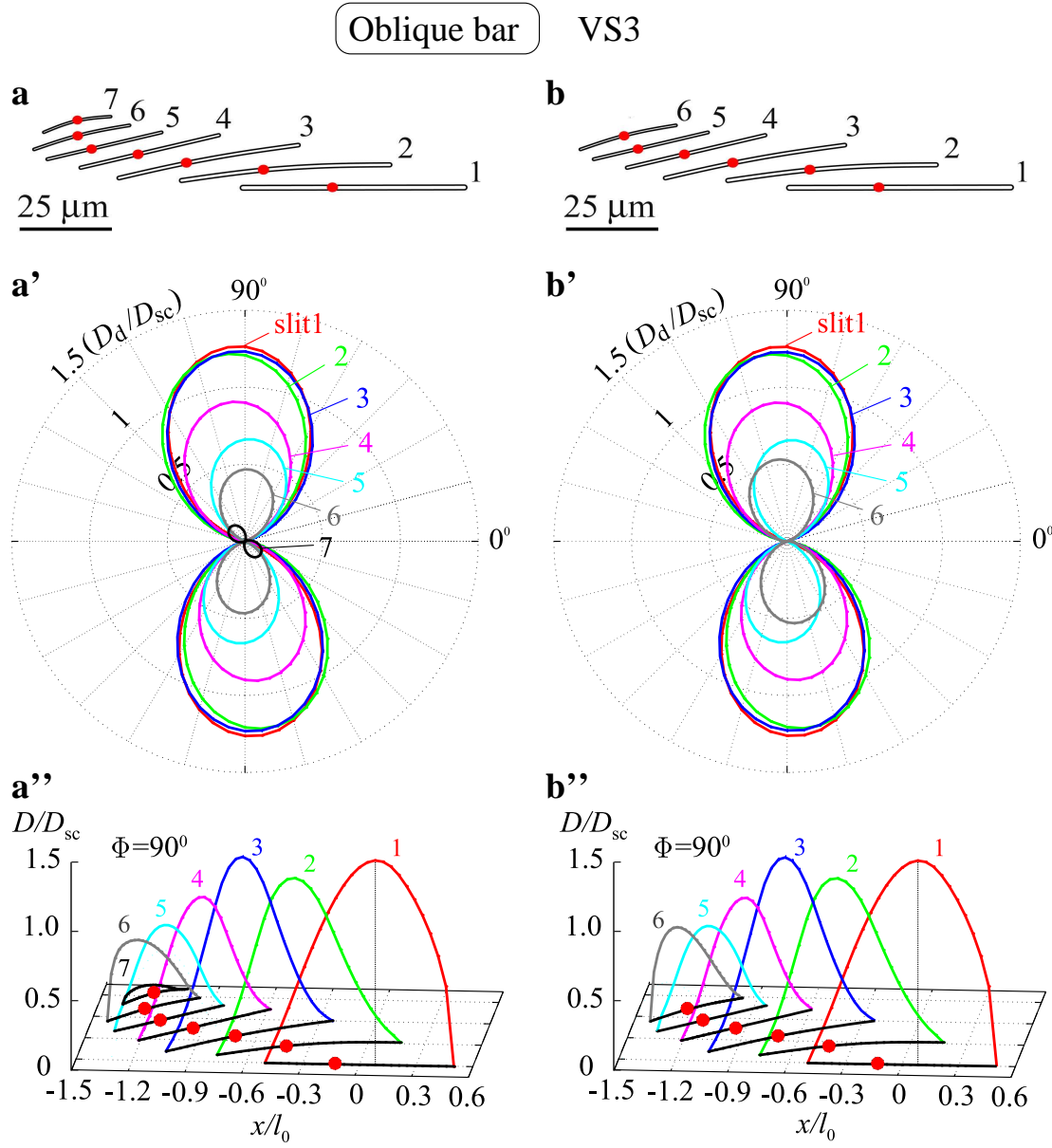


FIGURE 4.30: Interaction effects of the smallest slit, slit7, on the remaining slits in the models based on organ VS3. Model (a), response (a') and displacements along the slit faces (a'') of the original model (seven slits). When slit7 is removed in the model (b) the directional sensitivity (b') and the amount slit face deformation along the faces (b'') of slit6 change.

formation can also be used to measure similar load ranges with different slits of different length. This characteristic was so far thought to be typical only for oblique bar formations

(compare Chapter 4.1.2.5) (Barth et al., 1984) and demonstrates the tailorability of the organs' responses by adjusting the slit length, the angular offset between the slits and the location of the dendrites. There is, however, a difference in the maximum slit face displacements and in the stress concentration factors at the tips of the slits (Table 4.3). Due to shielding effects in the triangular formation VS5 of *Aphonopelma sp.* (Fig. 4.24b') the maximum of D_d/D_{sc} is approximately 0.7 (SCF=15.6) compared to approximately $D_d/D_{sc} = 1.25$ (SCF=23) in the oblique bar formation VS3 of *C. salei* (Fig. 4.20b'), where the slit face displacements of slit1 to 3 are amplified.

A possible conclusion is that in regions not critical in terms of failure of the cuticle an oblique bar formation is better suited to extracting the load amplitude. In contrast, triangular formations are suited for positioning on ring-like stiffening structures, such as those present at the location of lyriform organ VS5, which is oriented perpendicularly to the circumferential direction (90°). In the latter case the deformations concentrate at the location of the organ when the cross sections of the legs change from circular to oval due to the loads transferred at the joints or due to the increased hemolymph pressure inside the legs.

As shown in Barth et al. (1984) and in Chapter 4.1.2.4 simplified fan-like slit arrangements consisting of five slits of equal length l_0 subtending total angles of 45° , 90° , and 180° have omnidirectional sensitivity to uni-directional stresses. In contrast the model of an actual lyriform organ studied here consists of 9 slits of graded lengths ($l/l_0=1, 0.61, 0.49, 0.36, 0.25, 0.22, 0.18, 0.17$, and 0.13) subtending a total angle of 58° . Although the models differ in geometry some similarities can be found: (i) at $\Phi = 90^\circ$ slit1 dominates the response; (ii) the direction of the highest sensitivities of the inner slits are between the ones of the first and the last slit in the arrangement; and (iii) the directional response of the last slit in the arrangement, slit9, has its maximum at $\Phi = 150^\circ$ similar to slit5 in the simplified formation that subtends an angle of 45° . The lyriform organ studied in the present work is positioned closely to the joint of the fang and the basal segment of the chelicera, oriented perpendicularly to the longitudinal axis of the latter. Here it may be used to detect the onset of the contact with prey (slit1 responds) and the direction of the much higher loads needed to manipulate it is determined by the remaining slits (slits2 to 9). Similar findings were reported by Noah et al. (2004) for the activity of the proximal group of campaniform sensilla oriented perpendicularly to the leg axis on the tibia of the cockroach. Here the

sensilla respond to the onset of the body weight at the beginning of the stance phase but the sensillum discharges were prolonged and could encode the level of load when increases were sustained.

Location within stiffening ring. For example, at the distal ends of the tibiae of the walking legs of *C. salei* stiffening rings increase the resistance to buckling and to changes of the cross section of the segment. Along the circumference of the ring there are 4 triangular lyriform organs, VS4, VS5, HS8, and HS9, subdividing it into four different sections. The ring thereby becomes more compliant at the positions of the organs where the deformations concentrate when the cross section of the tibia changes. Organs HS8 and VS4 are located at comparable positions on the front- and backsides of the legs and have similar sizes and outlines (compare Fig. 4.16a and Fig. 4.23a). From electrophysiological measurements we know that HS8 is stimulated when the metatarsus is moved in an anterior direction (Barth and Bohnenberger, 1978) by which the cross section of the tibia ovalizes. This effect is described in Chapter 5.1.4 in more detail. Similar deformations occur at the position of VS4 ($D_{d,max}/D_{sc} \approx 0.6$) when the metatarsus is moved backwards.

4.2.3.3 Mechanical interaction between lyriform organs and nearby slit arrays

Lyriform organs and groups of slits. In Chapters 4.1.1 and 4.1.2 we concentrated on different types of slit arrangements analyzing slit interaction either in loose groups or in lyriform organs. In addition, interactions between loose groups and lyriform organs and between neighboring lyriform organs can be expected if their neighboring distance is less than three times the length of the longest slit in the arrangement (compare Chapter 4.1.1). Examples found on the walking legs of *C. salei* are the triangular lyriform organ HS3 and a loose group, the triangular lyriform organ VS1 and a loose group on the trochanter, the triangular lyriform organs HS6 and HS7 on the patella, the triangular lyriform organs HS8 and HS9 on the tibia, and two fan-like triangular lyriform organs on the chelicera (Barth and Libera, 1970).

Slit arrangements involved. Note that in most of the above cases triangular formations are involved. The different geometrical arrangements of the slits may result from potential differences in the load introduction. The principle behind the close neighborhood appears

to be to increase the overall working range in a particular area of the exoskeleton (Fig. 4.16 and Fig. 4.26). The working range of a slit pattern, e.g. range and number of distinguishable load levels and range of load directions, can be increased by adapting slit length, slit orientation and/or the number of slits.

Distinguishable load levels. In contrast to the anterior side of the distal end of the tibia at the position where the organ VS4 is located at the posterior side for some reason (may be to achieve some information for different behavioral purposes) extending the range of distinguishable load levels appears to be required. This can be achieved by using lyriform organ HS9 located close to (lateral distance approximately the length of the longest slit in HS9) and therefore interacting with organ HS8, which is similar in size to VS4. The amplitude ranges of HS8 and HS9 cannot be clearly separated, which may imply that the information from both organs is integrated in the spider's brain to determine the amplitude of the load. This can be best achieved at loading directions of $\Phi \approx 111^\circ$ where in both organs the slits deform in the order of their length. Remarkably, in the simulations using planar FE models loaded by uni-axial stresses we found that D_d/D_{sc} is roughly 0.6 at $\Phi \approx 111^\circ$ for both arrangements, VS4 and the combination of HS8 and HS9, respectively. In these formations a small change in the orientation of the uni-directional load of a few degrees drastically changes the amount of slit deformation. This suggests that the load direction is more or less constant at the locations of these organs.

Extension of the range of distinguishable load levels. On the trochanter of *C. salei*, where there is a flat region of the cuticular exoskeleton, the load ranges that can be detected by the organ HS3 can be extended by those of a loose group from $D_d/D_{sc} = 0.6$ to $D_d/D_{sc} = 2.2$ (Fig. 4.26). Similar to HS8 and VS4, the lyriform organ HS3 has its opponent VS1 on the anterior side of the trochanter. Note that, although extending over a larger area, a loose group has the advantage that the slit face displacements are less sensitive to changes of the geometrical arrangement of the slits, i.e. slit position, slit orientation, and slit length.

Extension of the range of load directions. Instead of a single large organ two closely neighboring fan-like triangular formations can also be used to detect loads in different directions as on the chelicera of *C. salei* close to the joint of the fang, where two organs of similar geometry are located in close neighborhood (closest distance $0.4 l_0$). One is oriented parallel to the longitudinal direction of the chelicera and the other one perpendicular to

it (Barth and Libera, 1970), which will result in a more omnidirectional response of the compound that may be used to control the clamping and releasing of the captured prey. Similarities are found on the tibia of the cockroach, where the longitudinal axes of two groups of campaniform sensilla are perpendicular (Zill and Moran, 1981). Here the sensilla are used to control the extension (proximal group perpendicular to the leg axis activated) and the flexion (distal group parallel to the leg axis activated) of the hind leg of the cockroach.

4.2.3.4 Dendrite positions

In models imitating lyriform organs the maxima of the slit face displacements typically are not found at the mid-length of the slits due to the skewed (non symmetric) slit patterns and the gradations in slit length (Fig. 4.22). In general, when the direction of a unidirectional load is altered the positions of the deformation maxima along the slits change, which was also found in generic slit arrangements (compare Chapters 4.1.2.4 and 4.1.2.5). For slit1 in the organ VS3 the difference between dendrite position and maximum face displacement is approximately $0.18 l_0$ for $\Phi = 90^\circ$ and $0.22 l_0$ for $\Phi = 60^\circ$. This is less than the value of $0.29 l_0$ estimated in Chapter 4.2.2.1 on the basis of a generic oblique bar formation consisting of five perfectly parallel slits of equal length. Even larger differences between the positions of the dendrites and the maximum face displacements were found for the triangular formation VS4. For $\Phi = 90^\circ$ and $\Phi = 60^\circ$ the shift of the dendrite from the position of maximum face displacement in slit1 is approximately $0.37 l_0$. Therefore, in agreement with Chapter 4.2.2.1 and Barth et al. (1984) also in the models based on real lyriform organs the positions of the dendrites are not always at the exact locations of the maximum slit face displacements but close to them, which may indicate that they are designed for maximum sensitivity to loads in a certain range of directions. May be the exact dendrite position indicates the actual load direction under natural conditions.

4.2.3.5 Stress concentrations associated with slit arrangements

Slits represent openings in the cuticle that give rise to local stress concentrations at their tips, that can be described by the stress concentration factor (SCF=local maximum

TABLE 4.3: Stress concentration factors (SCF) at the tips of the slits for single slits/ellipses and slit arrangements studied within the present work.

geometry/slit arrangement	load direction Φ in deg	SCF
single isolated slit (aspect ratio =100)	90	21.9
single isolated slit (aspect ratio =2.5)	90	4.2
single isolated ellipse (aspect ratio =2.5)	90	5.96
VS3 (straight slits)	95	20.7
VS3 (detailed model)	95	23
VS4	100	19.5
VS5 (<i>C. salei</i>)	80	15.9
VS5 (<i>Aphonopelma sp.</i>)	45	15.6
HS3 (isolated)	10	17.3
HS3 with neighboring loose group	90	29.3
HS8/HS9	145	25.9

stress/far field stress) (Peterson, 1974). The stress concentrations can be best visualized in fringe plots of the stresses in the vicinity of the slit arrangements. Similar to fracture mechanical investigations in (Höbl et al., 2006) where the stress intensity factors (SIF) describing the intensity of the stress singularity at the crack tips are correlated to the crack face opening displacements here the stress concentration factors at the ends of the slits are connected to the slit face displacements. Accordingly, fringe plots of the stresses can be used to find the slits with the highest deformations. When slits are embedded in regions of low stresses then they are shielded by other slits in the arrangement.

In the planar models a single isolated capped rectangular slit with an aspect ratio of 100 has a SCF of approximately 21.9. When the aspect ratio decreases to 2.5 then the SCF decreases to 4.2 which is close to that of a circular opening (SCF=3). In contrast, for ellipses with aspect ratios of 2.5, as found in strain sensitive campaniform sensilla in the cuticle of insects, a SCF of approximately 6 is found, i.e. the stress concentrations at their ends are higher than in capped rectangular slits with parallel faces and rounded ends as found in arachnids.

High stress concentration factors are present when amplification effects determine the slit

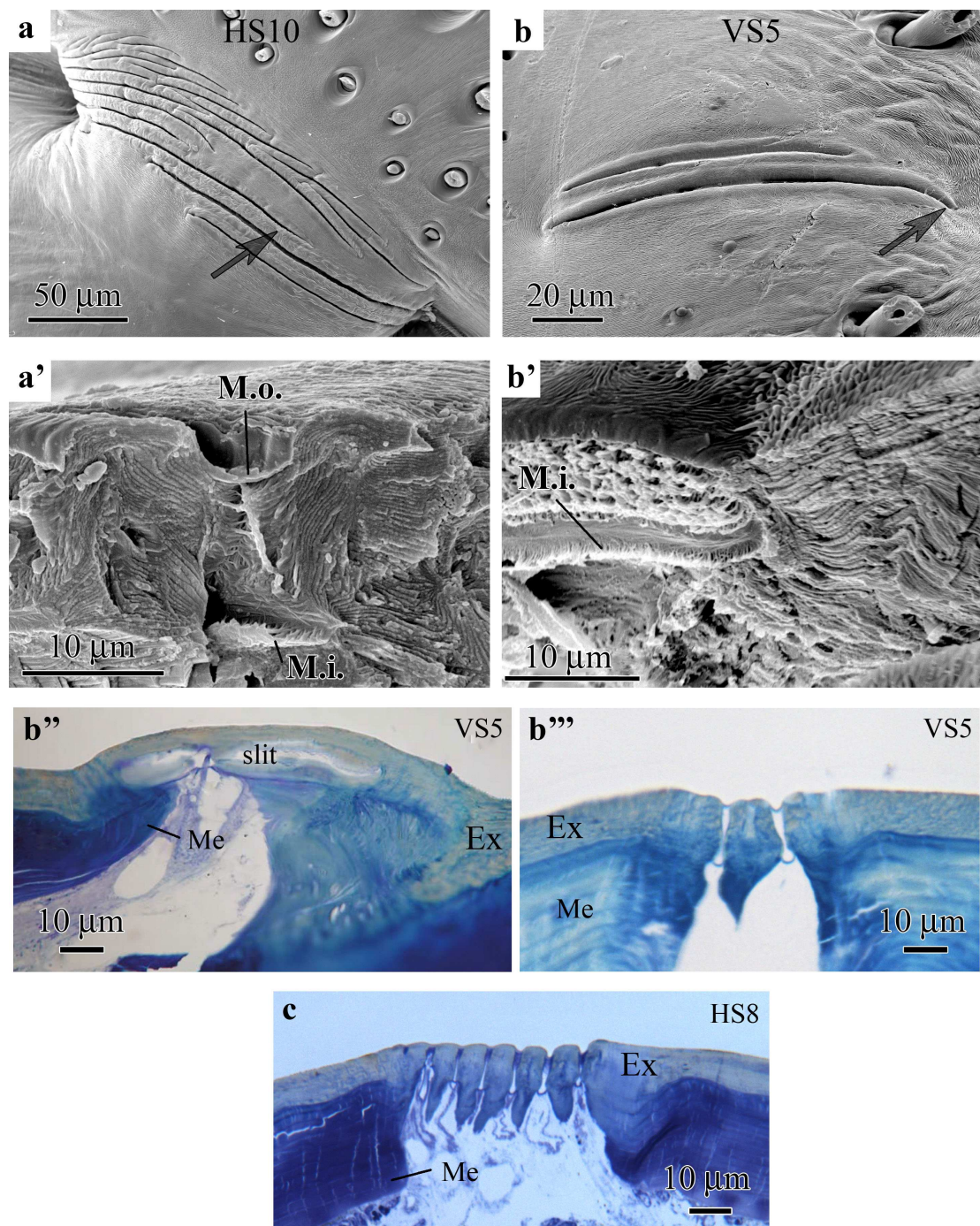


FIGURE 4.31: Details of lyriform organs VS5 and HS8 on the tibia and of organ HS10 on the metatarsus of the spider *C. salei*. **a** SEM image of organ HS10 fractured perpendicularly to its slits (**a'**). **b** SEM image of organ VS5 fractured along its longest slit (**b'**). **b''** Semi-thin slice along one of the two slits of VS5. **b'''** Semi-thin slice normal to the slits longitudinal axes of VS5 and **c** of HS8 close to the location of the dendrite of the smallest slit in the arrangement (Müllan, 2005). The black arrows in **a** and **b** point to the location where the pictures **a'** and **b'** were taken. Ex exocuticle; Me mesocuticle; M.o. outer membrane; M.i. inner membrane.

face displacements between the slits in lyriform organs. For example in the formation HS3, which closely neighbors a loose group of slits (maximum $D_d/D_{sc} \approx 2.2$), the SCF is approximately 29. It may be noted that in this arrangement the highest value of the SCF is found within the arrangements studied in the present work (see Table 4.3). In contrast when HS3 is isolated a maximum value of $D_d/D_{sc} \approx 0.7$ is obtained and the SCF decreases to approximately 17, which is lower than that of a single isolated slit of aspect ratio 100 ($SCF \approx 22$). The stress concentrations in the exocuticle most probably are the reason for the increased fiber volume fraction in the vicinity of the slits which is known from the SEM images of the organ HS10 fractured normal to the slits (Fig. 4.31a and a') and organ VS5 that was fractured along its longest slit (Fig. 4.31b and b') (Müllan, 2005). In addition the exocuticle is thickened in regions where stress concentrations are present. For example, in the vicinity of organ VS5 ($SCF \approx 16$) the exocuticle is approximately 25 μm thick at one end of the slits (Fig. 4.31b'') and 13 μm close to the center as seen in a section normal to its longitudinal axis (Fig. 4.31b'''). In a section normal to the longitudinal axis of the organ HS8 ($SCF \approx 26$) close to the location of the dendrite of the smallest slit the exocuticle is approximately 16 μm thick (Fig. 4.31c), whereas its average thickness is about 10 μm . Note that an increase of the stiffness by increasing the fiber volume fraction and/or the thickness of the cuticle in the vicinity of the slits typically decrease the sensitivity of the slits.

4.2.4 On determining the direction of a uni-directional load

In color reception the spectral absorption curves of the short, medium and long wavelength pigments in human cone and rod cells are similar to Gauss curves when the wavelength of monochromatic light is varied. Typically the maximum absorption is ≈ 420 nm for the short, ≈ 534 nm for the medium, and ≈ 564 nm for the long wavelength pigments. The correlation between the amount of absorption of a single photoreceptor cell and the actual wavelength of the light is not unambiguous because of Gaussian shape of curve. To clearly determine the wavelength a number of different cells, e.g. three in mammals, are needed.

In slit sensilla a similar principle may be used for determining the direction of a load. For a better understanding the results for the directional sensitivity to uni-directional loads of a fan-like array depicted in Fig. 4.12c ($R = 0.35 l_0$ and $\alpha = 180^\circ$) and those for a heart

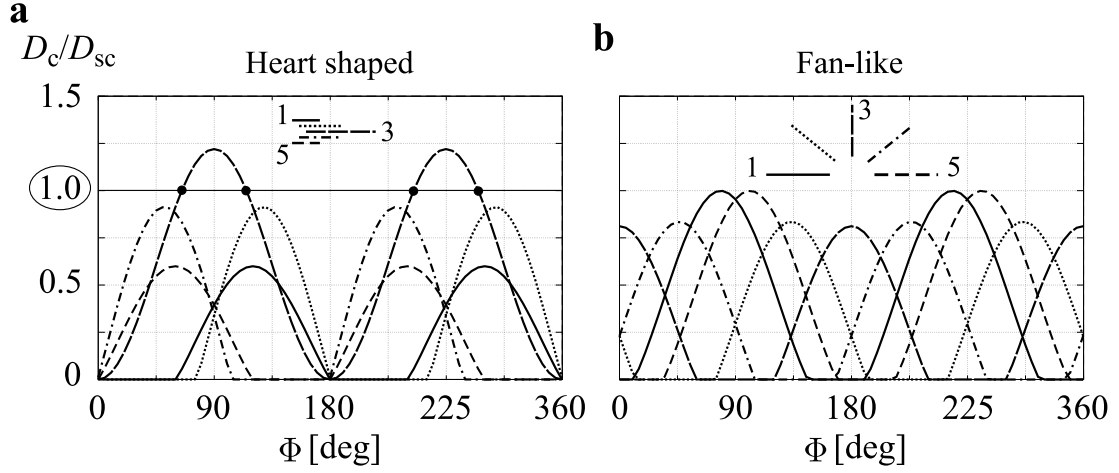


FIGURE 4.32: Plot of the slit face displacements over the load angle Φ of a heart shaped and a fan-like array ($R = 0.35 l_0$ and $\alpha = 180^\circ$), shown in Fig. 4.13c and Fig. 4.12c, respectively. When the signals of several slits sensitive to loads in different directions are available the direction of a load can be determined unambiguously.

shaped arrangement shown in Fig. 4.13c were plotted in terms of slit face displacements over the load angle Φ in Fig. 4.32a and b. If only one slit is considered, e.g. slit3 in the heart shaped arrangement shown in Fig. 4.32a, a given value of the slit face displacement, say $D_c/D_{sc} = 1$, results in two possible load directions, namely 65° and 115° . When the remaining slits of the array are added into the considerations, however the load direction can be uniquely evaluated. The slit face deformations are more evenly distributed in the fan-like arrangement (Fig. 4.32b) which may, accordingly, be better suited to determining the direction of a load.

The sensory signal that must be processed by the spider, of course, also depends on the characteristics of the transduction system consisting of dendritic endings, coupling cylinder, outer and inner membrane, as well as the fluid filling of the slits. Provided the transfer functions of this system are known, the results given in Chapters 4.1.2 and 4.1.3 can be used to predict the physiological signal of planar slit sensilla in the small strain regime. The actual extraction of the load direction and, possibly, of the orientation and principals of the strain tensor, from such signals poses an inverse problem that is more difficult to solve than the “direct” problem of determining the slit face deformations for given far-field

strains.

Sensing the direction of a load may be important, e.g. on the chelicera where a wide range of loads occur during the capturing and manipulation of prey. The fan-like lyriform organs situated close to the fangs may be intended in this manner. A further example where the direction of a load may change is on the leg segments that are strongly rotated during locomotion and where the forces acting on the condyli change their directions accordingly, e.g. the heart shaped lyriform organ HS2 on the trochanter of *C. salei* (Fig. 3.18b).

Chapter 5

3D models

5.1 Results

In the following sections by convention positive values of D , D_c , and D_c/D_{sc} correspond to a reduction of the width, w_0 , of a given slit.

5.1.1 Effect of shape of the membranes of a single slit without filling subjected to normal uni-axial loads

In the models the deformations were evaluated at 5 points on the membrane and the coupling cylinder (see details in Fig. 5.1a to c). Although a geometrically nonlinear analysis was performed all points considered show linear local displacement responses. The curves are similar for the three shapes of the membranes, low curvature, semi-circular, and semi-circular with dimple, considered. The only exceptions with respect to the latter point are the curves describing the displacements in z -direction of the coupling cylinder and the curve describing the deformation of the coupling cylinder at the upper rim proper at point 2 in x -direction the slopes of which depend considerably on the configuration (Fig. 5.1d and d'). They are highest for the membrane of low curvature and lowest for the semi-circular membrane with the dimple. No local geometrically nonlinear

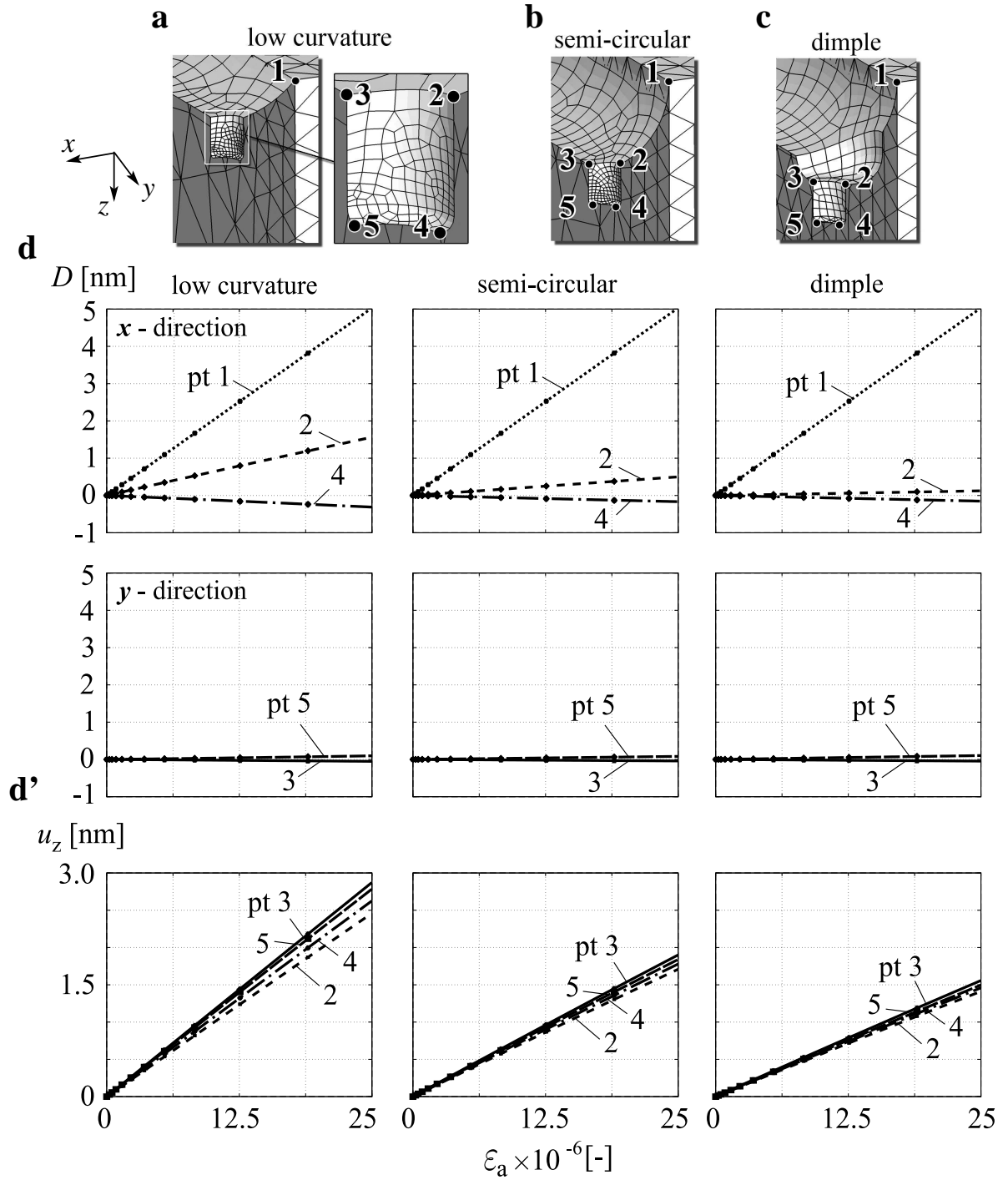


FIGURE 5.1: Different cross sections of the outer membrane of a single slit. **a** low curvature cross section, **b** semi-circular cross section, and **c** a dimple in a semi-circular cross section. The points for which the deformations were evaluated are marked as 1 to 5. **d** Results for the deformations of the slit faces and the coupling cylinder D in x - and y -directions and **d'** for the displacements in z -direction, u_z , evaluated at the points 1 to 5 as functions of the far-field strain ε_a applied in y -direction ($\Phi = 90^\circ$).

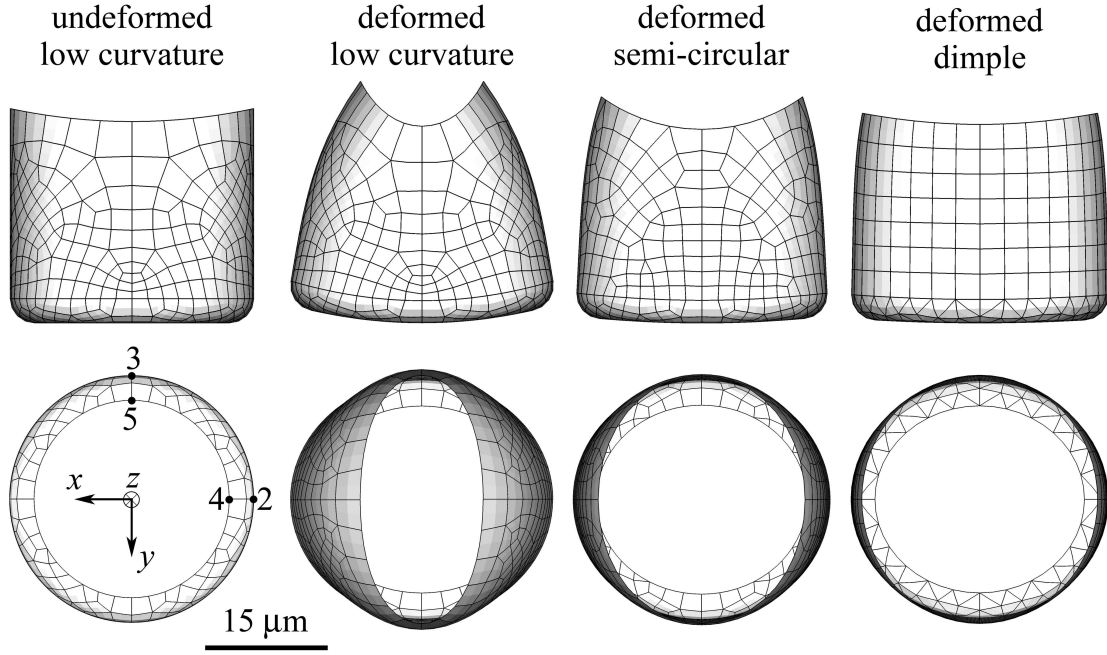


FIGURE 5.2: Undeformed and deformed shapes of the coupling cylinders in membranes with low curvature, semi-circular cross section, and semi-circular cross section with a dimple. The y -direction pertains to the longitudinal axis of the slit, the x -axis is perpendicular to it. The displacements are scaled up by a factor of 15.

effects of the three types of membranes were encountered for the moderate load levels considered.

Under an applied far-field strain in x -direction ($\Phi = 90^\circ$) of $\varepsilon_a = 2.5 \times 10^{-5}$ the change in diameter of the coupling cylinder at point 2 in x -direction is approximately 1.57 nm for the membrane with low curvature, 0.5 nm for the semi-circular membrane, and 0.13 nm for the case where a dimple is incorporated in the semi-circular membrane at the location of the dendrite (Fig. 5.1d). Because we are considering quarter models taking advantage of mirror symmetries with respect to the $x = 0$ and $y = 0$ planes, the y -displacements of points 1, 2, and 4 as well as the x -displacements of points 3 and 5 are zero. The predicted deformed shapes of the coupling cylinders are quite complex (Fig. 5.2; note that displacements are scaled up by a factor of 15). The cross sections of the outer rims change considerably from circular to elliptical. The inner rims show only small deformations. This is in agreement with the results of experiments on polymer models of a semi-circular mem-

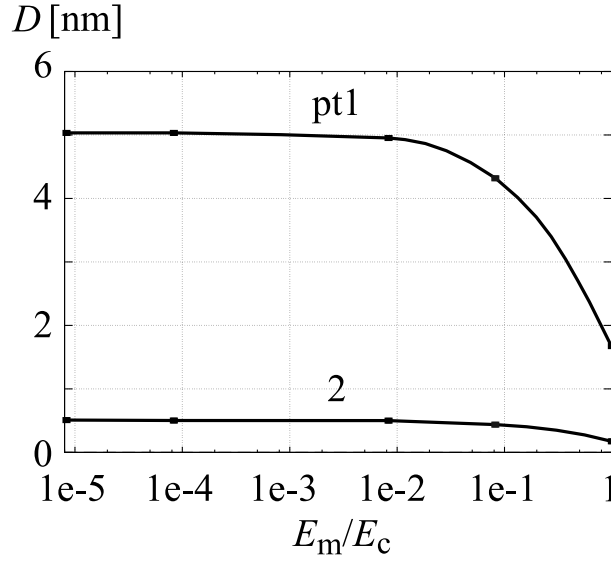


FIGURE 5.3: Influence of the relative Young's modulus E_m/E_c (membranes/cuticle; $E_c = 18$ GPa) on the slit deformation of a single slit (point 1 in Fig. 5.1b) and on the change in diameter of a coupling cylinder incorporated in a semi-circular membrane (point 2 in Fig. 5.1b) loaded perpendicularly to its longitudinal axis (at $\Phi = 90^\circ$).

brane incorporating a coupling cylinder performed by Barth (1972b). Slits with membranes of low curvature lead to stronger local deformations of the coupling cylinders under uni-axial loading at $\Phi = 90^\circ$ compared to slits with membranes of semi-circular cross sections or semi-circular cross sections and dimples at the location of the dendrites. When more compliant (Young's modulus $E_m = 1.5$ kPa) or stiffer ($E_m = 150$ MPa) membranes and coupling cylinders were used similar results were achieved (Fig. 5.3). When the Young's modulus of the membranes is increased to that of the cuticle ($E_c = 18$ GPa) the slit deformation decreases to approximately 1.7 nm and the upper rim deforms by 0.17 nm only. Note that even for $E_m = 150$ MPa the in-plane stiffness of the membrane is approximately 1/5000 that of the cuticle due to its small thickness.

5.1.2 Fluid filled single slit subjected to normal uni-axial loads

Figure 5.5 depicts the results of the geometrically nonlinear simulations of the deformations at points located at the slit faces (point 1) and on the membranes (points 2 and 3). The assumptions made are an inner membrane which is impermeable to the slit's con-

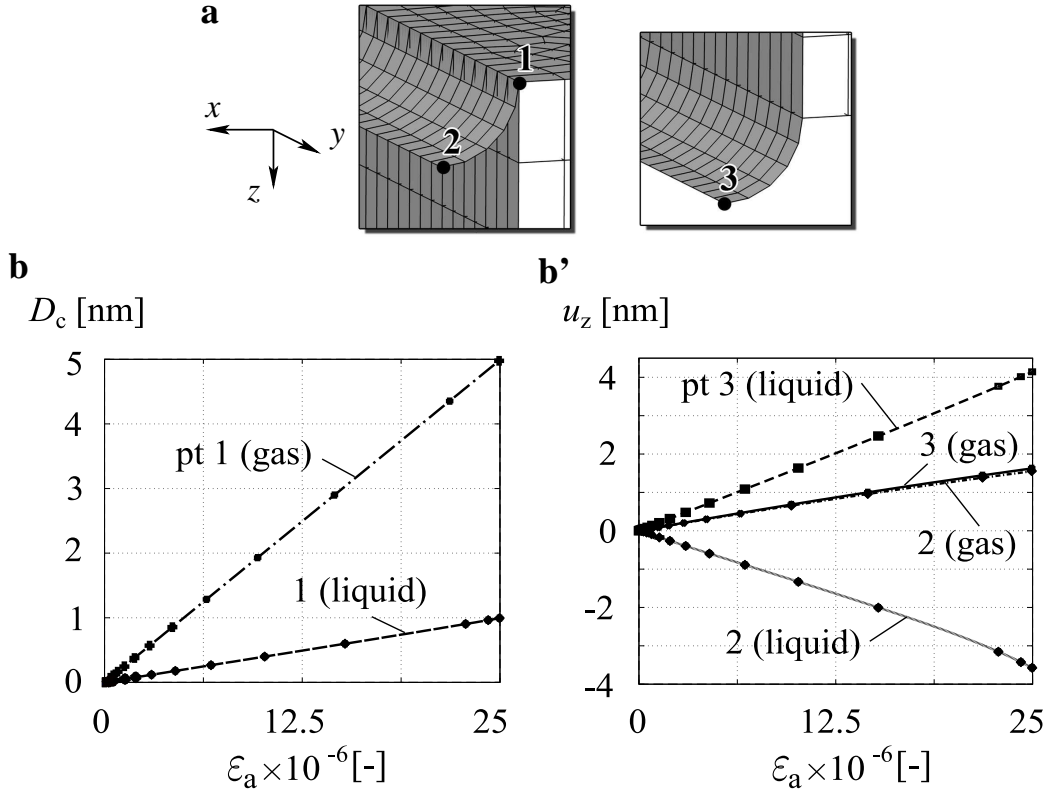


FIGURE 5.4: Model of a single slit used to study the influence of the fluid filling the slit. **a** Quarter model incorporating the points where the deformations u were evaluated (compare Fig. 5.5). **b** Results for the slit face deformations D_c at point 1 and **b'** the displacements u_z at the points 2 and 3 for highly compressible and nearly incompressible fluids present inside the slit as a function of the far-field strain ε_a .

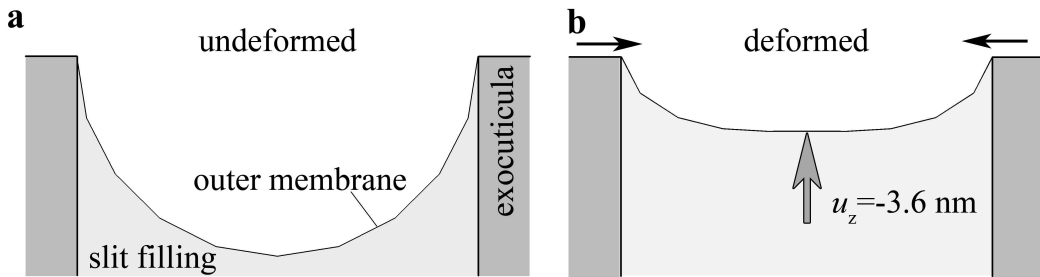


FIGURE 5.5: Deformation of a single isolated slit considering a nearly incompressible slit filling. **a** Undeformed and **b** deformed shape of the outer membrane. The displacements are scaled up by a factor of 30.

tents (filling) and a nearly incompressible (“liquid”) or highly compressible (“gas”) fluid, respectively, filling the slit. When a gas is chosen as filling, point 1 shows a deformation of $D_c \approx 5$ nm under an applied far-field strain of $\varepsilon_a = 2.5 \times 10^{-5}$ in the direction normal to the slit. This value is similar to that predicted for a slit without a filling ($D_{sc} = 5.034$ nm for $l = 100 \mu\text{m}$ and $\varepsilon_a = 2.5 \times 10^{-5}$), and 5 times larger than for a fluid filled slit (left part in Fig. 5.5b). It is also close to corresponding results for an “empty” single slit of length $100 \mu\text{m}$ and width $1 \mu\text{m}$ previously modeled in a planar disk (see Appendix B). Outer and inner membrane (points 2 and 3) bulge inwards ($u_z \approx 1.5$ nm) when a gas filled slit is compressed under a far-field strain of $\varepsilon_a = 2.5 \times 10^{-5}$ (Fig. 5.5b’). In contrast, in the liquid filled slit with an impermeable inner membrane only the inner membrane bulges inwards by $u_z \approx 4.2$ nm (point 2) whereas the center of the outer membrane is pushed towards the outside of the slit by approximately 3.6 nm (point 3) (Fig. 5.4). This means that the outer membrane is still bulged inwards but it is flattened at its center.

5.1.3 Effect of membrane stiffness in a stack of five slits subjected to normal uni-axial loads

We evaluated the slit face deformations D_c of a non-staggered array of five identical and “empty” slits of aspect ratio $l/w_0 = 100$ (Fig. 5.6a) and 20 (smaller l , same w) (Fig. 5.6b) at the centers of the slits in the direction normal to the slit faces and relative to the deformation of single isolated slits D_{sc} of aspect ratio 100 and 20. The left end of the diagram shown in Fig. 5.6a’ (vanishing E_m) corresponds to the results of a similar slit configuration cut into a planar disk presented in Chapter 4.1.2.2, i.e. the inner slits (slit2 to slit4) open up under compressive in-plane stresses. When E_m is increased to more than, say, 10 MPa (compare the Young’s modulus of exocuticle, $E_c = 18$ GPa) all slits approach a similar level of normalized slit face deformation of approximately 0.22. Note that the thickness of the membranes is $0.25 \mu\text{m}$ in contrast to the $\approx 10 \mu\text{m}$ thick exocuticle. When the stiffness of the membranes increases then the slit face deformations D_c of slit1 and 5 decrease but those of slit2 to 4 increase (Fig. 5.6a’). For slits of a reduced aspect ratio of 20 the results of the slit deformation are independent of the stiffness of the membranes in the range between 0 and at least 18 MPa (Fig. 5.6b’). Here the bending of the cuticular material between the slits (“ligaments”) is much less pronounced compared to the configurations

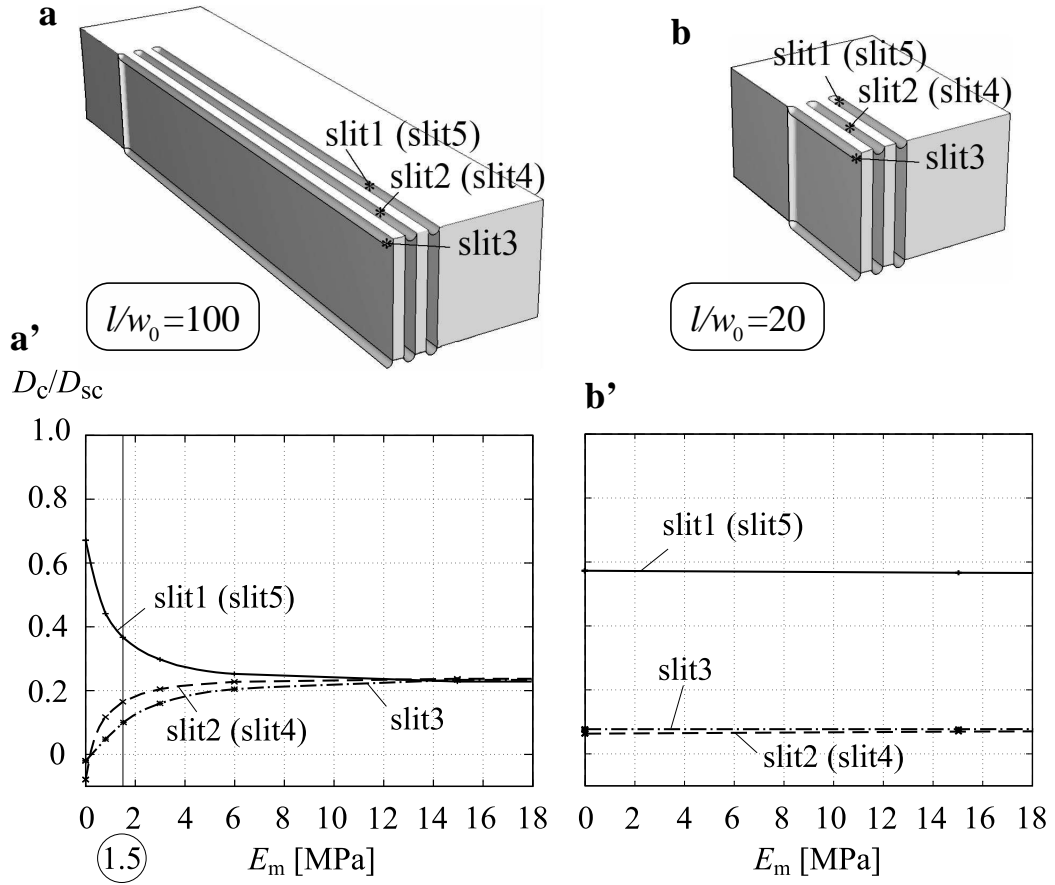


FIGURE 5.6: Influence of the stiffness of the membranes (E_m) of semi-circular cross section on the relative slit deformation in a stack of five similar parallel slits when their width w_0 and their neighboring distances of $S = w_0$ are held constant. Quarter models for slits of aspect ratio $l/w_0 = 100$ (**a**) and 20 (**b**). **a'** and **b'** dependence of the relative center slit face displacement D_c/D_{sc} on E_m .

with $l/w_0 = 100$.

5.1.4 Embedding of slits in disks and cylinders three-dimensionally curved at the site of the slit

Embedding of slits in planar disks. The largest slit face deformation of $D_c = 9.65$ nm is found for a single isolated slit modeled in a transversely isotropic planar disk (type a in

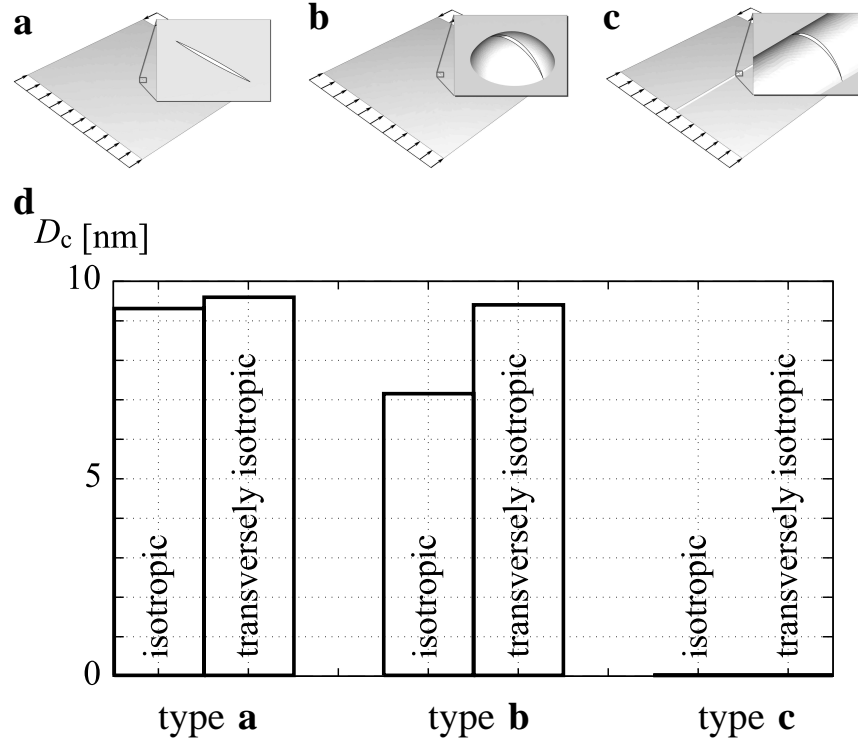


FIGURE 5.7: Comparison of a single isolated slit modeled in **a** a flat disc, **b** a spherical bump, and **c** a ridge-like structure. **d** Results of the slit deformation at the center of the slits, D_c , for isotropic and transverse isotropic material laws.

Fig. 5.7d). When the transversely isotropic material was used in the model of a bump in the planar disk (type b in Fig. 5.7d) the slit is compressed by $D_c = 9.46$ nm which is only 2% less. In contrast, when an isotropic material behavior (see Table 2.3) was used for the model incorporating a bump the difference increased to approximately 2.3 nm. The slits dilated when they were located on a ridge parallel to the loading direction in a planar disk (type c in Fig. 5.7d) because the center region of the disks deformed in positive z -direction under uni-axial in-plane deformations for both material laws due to bending introduced by the slight asymmetry of the configuration (ridge is located on one side of the disk only).

Note that the difference in slit face deformation of a single slit modeled in an isotropic and a transversely isotropic planar disk remains very small at 3%. This is due to the fact that in-plane deformations are mainly determined by the in-plane Young's modulus which is similar in both models.

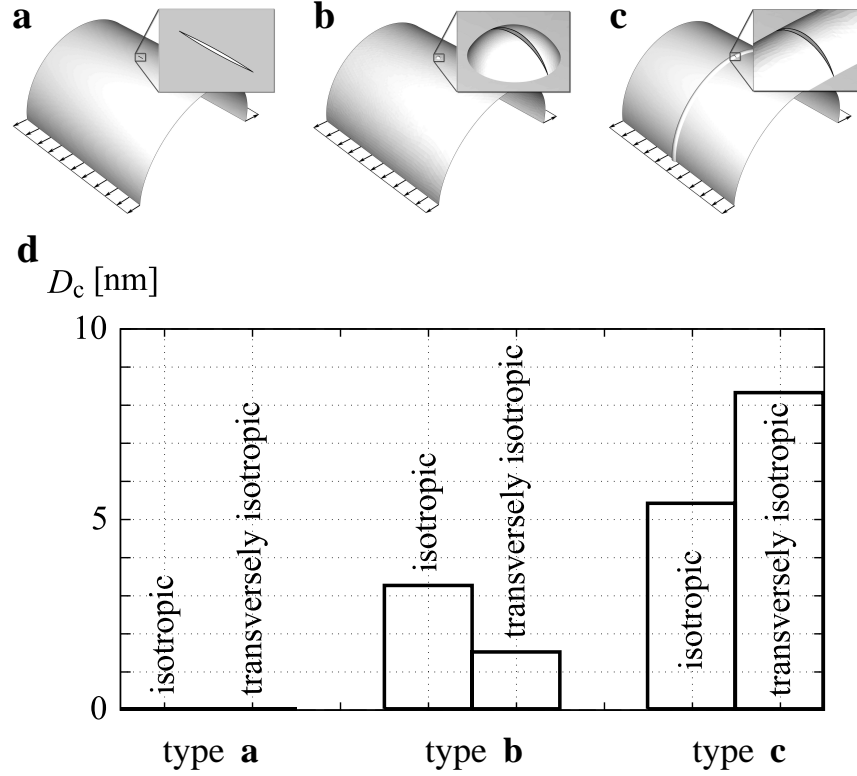


FIGURE 5.8: Dependence of the slit deformation of a single slit incorporated in isotropic and transverse isotropic cylinders. **a** Single slit in a smooth cylinder, **b** single slit in a spherical bump, and **c** single slit in a ring-like structure. **d** Bar diagram of the slit face displacements D_c in nm.

Embedding of slits in ovalizing cylinders. Slits in cylinders without local surface features were not deformed because they were placed in the reference plane where no deformations occur under bending (type a in Fig. 5.8d). Therefore, such configurations are not found on the walking legs of *C. salei*. When the slits are positioned on bumps or ridges the amount of deformation increases as the height and therefore the distances between the reference plane of the shells and the centers of the bumps or the ridges increase. Accordingly, a single slit positioned on a bump of height $45 \mu\text{m}$ deforms by $D_c = 3.2 \text{ nm}$ in a disk with isotropic and by $D_c = 1.4 \text{ nm}$ in disk with transversely isotropic material behavior, respectively (type b in Fig. 5.8d). This is due to combined in-plane and out-of-plane deformations in the disks with transversely isotropic material behavior with an elastic contrast of ≈ 3.7 between the in- and out-of-plane directions (Table 2.3). The largest deformation of a single

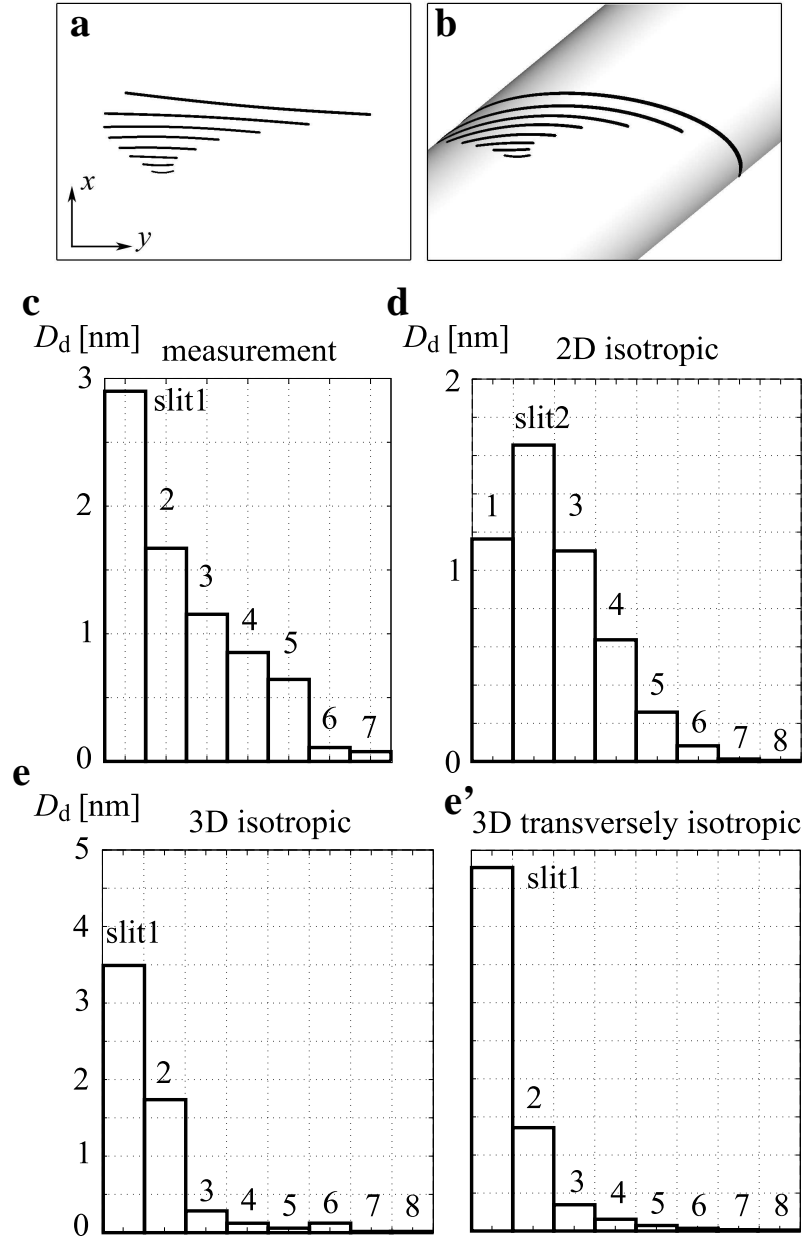


FIGURE 5.9: Bar diagrams of the slit face deformations in a slit arrangement based on lyriform organ HS8 of *C. salei* modeled in **a** a planar disk under planar uni-axial strains ($\varepsilon_a = 2.5 \times 10^{-5}$) and **b** a plate under bending (rotations of the horizontal edges of 0.057°). **c** values measured for organ HS8 in a live spider using white light interferometry as described in Chapter 4.1.3 using a deflection of the metatarsus by $\Theta = 0.01^\circ$ as a stimulus Hößl et al. (2007b), **d** results for a planar slit arrangement in an isotropic disc, and **e** slit face deformations of the slits in a 3D shell for isotropic and in **e'** for a transversely isotropic material behavior.

slit of $D_c = 8.3$ nm occurs when the slit is positioned parallel to the axis of the cylinder (in meridional direction) in a ring-like structure with transversely isotropic material behavior, that is subjected to an ovalizing displacement of $100\text{ }\mu\text{m}$ (type c in Fig. 5.8d). The difference in slit deformation between a slit positioned in a spherical bump and in a ring-like structure is 2.2 nm for the isotropic and 6.8 nm for the transversely isotropic material law. Among the three configurations investigated a slit positioned in a ring-like structure has the highest sensitivity to ovalizing loads for both isotropic and transversely isotropic material laws.

5.1.5 Slit interaction under bending loads

On the posterior side on the tibia of *C. salei* the lyriform organ HS8 is located. Interferometric measurements of the slit deformations in HS8 positioned on a stiffening ring show that the cuticle at the site of HS8 moves towards the center of the tibia (Fig. 4.18c) which indicates that the tibia is ovalized due to the transferred loads at the tibia-metatarsus joint. Therefore bending moments are induced at the site of the organ that is located on a ring-like structure. To show the differences in slit interaction between planar (in-plane loads) and three-dimensional models (bending loads) we compare the slit face deformations of a slit array based on lyriform organ HS8 of *C. salei* (Figs. 5.9 a and b) exposed to uni-axial stresses (Fig. 5.9d) and to bending moments (Figs. 5.9e and e') to the results of the white light interferometric measurements of the slit deformations in HS8 that is stimulated by a lateral deflection of the metatarsus by $\Theta = 0.01^\circ$ (Fig. 5.9c, compare Fig. 4.18b). All results were evaluated at the locations of the dendrites.

In the planar model slit2, the second longest slit in the arrangement, shows the largest deformation (Fig. 5.9d). The load level slit1 is sensitive to is similar to that of slit3 in this case. In contrast, when the slits are located on a ridge, like organ HS8, slit1 deforms most by approximately 3.5 nm if an isotropic material and 4.8 nm if a transversely isotropic material behavior for the disk is used, respectively (Figs. 5.9e and e'). The difference in the slit face deformation of slit1 between isotropic and transversely isotropic material models amounts to 1.3 nm ($= 27\%$). Furthermore, the order of the smaller slits in terms of amount of slit deformation changes when the material law is altered.

5.2 Discussion

In studies of the mechanical behavior of single slits and arrangements of slits in planar regimes we concentrated on the influence of the geometrical parameters describing slits and slit arrangements on the deformation of the slits (Chapter 4.1.1, Chapter 4.1.2, and Chapter 4.1.3). In this chapter we concentrate on the influence of (i) three-dimensional details of the slits such as deformation of the coupling cylinder, deformation of the membranes covering the slits under consideration of the slits' contents, and effects of shape and stiffness of the membranes covering the slits on the slit deformation as well as influences of (ii) the three-dimensional shapes of the cuticle at the site of the slits, i.e. spherical bumps or ridges and rings of circular cross section on the slit face deformations.

It is interesting to note that in the three-dimensional shell models studied in Chapter 5.1 a transversely isotropic material behavior as present in the cuticle increases the sensitivity of the slits located on dimples in planar disks and on rings in cylindrical shells compared to an isotropic one. Accordingly, similar slit face deformations are achieved when a slit is positioned on a ring with height $45\text{ }\mu\text{m}$ and width $160\text{ }\mu\text{m}$ in a cylindrical shell of diameter 5 mm with isotropic material behavior and when it is located on a ring with height $30\text{ }\mu\text{m}$ and width $107\text{ }\mu\text{m}$ in a similar cylindrical shell but with transversely isotropic material behavior.

5.2.1 Details of slits and stimulus transformation

In TEM images of the cross sections of the slits in lyriform organs of *C. salei* flat membranes, as well as membranes of semi-circular cross section and of semi-circular cross section with an additional dimple at the site of the dendrites are frequently seen (Fig.3.13 a to c) (Barth, 1971, 1972b; Müllan, 2005). The lateral deformation of the dendritic tip in the outer membrane is thought to be important in terms of stimulus transformation because the dendrite is free to move normally to the surface of the cuticle (Barth, 1972a). In the simulations the smallest lateral deformation of the coupling cylinder is found for a semi-circular membrane that contains an additional dimple, i.e. in a configuration with high curvature which is in contrast to Barth (1972a) where it is concluded that the bending mo-

ments at the center of the membranes of high curvature are higher compared to flat ones favoring the deformation of the coupling cylinder. In the models the change in diameter of the coupling cylinder is approximately 0.13 nm and $1/38^{\text{th}}$ of the amount of slit deformation at the center of the slit (≈ 5 nm). In contrast, for a flat membrane the deformations of the coupling cylinder are scaled down by a factor of 3.2 only. This indicates that the deformation at the locations of the dendrite in long slits, where semi-circular cross sections with additional dimples are found, is reduced to protect the sensory terminals from mechanical damage by overstimulation as in spider tactile hair (Barth et al., 2004). To adjust the sensitivity of the single slit considered five possibilities seem feasible: (i) changing the length l of the slits, (ii) changing the orientation of the slit relative to a uni-axial loading Φ , (iii) changing the position of the location of the dendritic ends along the slit faces (compare Chapter 4.2.2.1), (iv) changing the Young's modulus of the membranes, and (v) changing the curvature of the membranes. When the cross section of the outer membrane changes from flat to semi-circular with a dimple the deformation at the site of the dendrite is reduced by 1.44 nm. A similar reduction of the slit deformation can also be achieved by decreasing the length of the slit from $100\ \mu\text{m}$ to $71\ \mu\text{m}$, by rotating the slit by $\Phi = 32^\circ$, by shifting the position of the dendrite by $35\ \mu\text{m}$ towards one end of the $100\ \mu\text{m}$ long slit, or by increasing the Young's modulus of the membranes to approximately 18 GPa. Therefore changing the orientation and length of the slit and the curvature of the outer membrane are the most efficient ways to reduce the sensitivity of the slit.

Direct measurements of slit face deformations of organ HS8 in *C. salei* using white light interferometry under biologically relevant loads (Fig. 4.18b) (Schaber and Barth, in prep.) show that when the metatarsus is subjected to a lateral force of approximately 10 mN, some slits were compressed by about 50%. Under these conditions the outer membranes bulge inwards towards the extracellular space. Under the assumption of an impermeable lower membrane such an inward bulging was only found in models with compressible fluid inside the slits. When nearly incompressible liquid was used for the slit's contents the outer membrane was flattened and pushed towards the outside of the slit. In actual lyriform organs no evidence for "gaseous" contents of the slits was found. Therefore, we may conclude that the lower membrane is permeable and the fluid has sufficiently low viscosity to flow rapidly into the extracellular cavity. Note that this combination can also act as a frequency dependent damper of the slit deformation under dynamic loads of the cuticle.

The model of a stack of five equal slits is an idealized configuration with regard to shape of the slits (straight slits of constant width), arrangement of the slits (parallel), cross section of the trough-shaped membranes (semi-circular), material properties of the disk (transversely isotropic, but not accounting for the orientation of the chitin layers close to the slits (Barth, 1971)), and slit contents (no filling). In this model the stiffness of the membranes, which are usually more compliant than the exocuticle according to electronmicroscopical analysis, mainly influences the deformation of the slits when the aspect ratio of the cuticular ligaments between the slits approaches 100 (Figs. 5.6a, a'). When the aspect ratio decreases to 20 the effect of the stiffness of the membranes is negligible (Figs. 5.6b, b'). In actual lyriform organs of *C. salei* the highest aspect ratios of the cuticular ligaments are found in the organ HS6 (Müllan, 2005), viz. 60, which is markedly smaller than 100. In addition, the widths of the cuticular ligaments are not constant along the slits and therefore their effective aspect ratio is less than 60 and the slits' filling may also stabilize cuticular ligaments. This may indicate that bending of the ligaments plays a minor role in actual lyriform organs.

5.2.2 Embedding of the organs and slit deformation

As seen in micrographs single slits are mostly located in planar cuticle in *C. salei*. In contrast in the cylindrical leg segments, e.g. close to the tibia-metatarsus joints on the walking legs of *C. salei*, ring-like structures are interrupted by slits that are oriented parallel to the legs longitudinal axes. FE models assuming a transverse isotropic material behavior show that in planar configurations a single slit modeled in flat disks under uni-axial stresses and in three-dimensional configurations a single slit dividing a stiffening ring of an ovalizing cylindrical shell are the most sensitive configurations in terms of slit face deformation. When a spherical dimple was used then the sensitivity of the slit was approximately 2% in the planar and approximately 35% in the three-dimensional configuration. Although the difference is small in planar configurations this, however, shows that the sensitivity of the slits can be controlled by placing surface features in the cuticle.

According to FE models imitating the embedding and the slit arrangement of lyriform organ HS8 of *C. salei* the interaction effects between neighboring slits differ depending on whether the arrangement is subjected to bending moments as indicated in the tibia or to uni-axial in-plane loads in planar discs. In the planar arrangement slit1 shows lower

sensitivity than slit2 (Fig. 5.9d). In contrast, in the arrangement modeled in a transversely isotropic disk which is subjected to bending moments the order in slit sensitivity is similar to the order in terms of slit length (Fig. 5.9e'). In the latter configuration the order of the slits in terms of their sensitivity changed when the isotropic in contrast to the transversely isotropic material law was used in the FE models (see Fig. 5.9e), due to the different in-plane and out-of-plane material properties (Table 2.3). When the results were compared to measurements on organ HS8 using white light interferometry (Fig. 5.9c) (Höbl et al., 2007b; Schaber and Barth, in prep.) evaluated for a deflection angle of the metatarsus $\Theta = 0.01^\circ$ similarities in the sequence of slit sensitivity and the order of the slits in terms of magnitude of slit face deformations are found only for the model of HS8 located on a ridge and using a transversely isotropic material law typical for spider cuticle (Fig. 5.9e').

The results of the planar FE models imitating actual lyriform organs presented in Chapter 4.1.3 gave an insight to the performance characteristics of lyriform organs but in some cases either the role of the smaller slits in the arrangements remains unclear because they showed very small deformations or the order in terms of slit deformations in the arrangements differed from that of their length. In those cases and especially for organs where ovalizing of leg segments is to be expected, e.g. the tibia of *C. salei*, the three-dimensional shape of the cuticle at the site of the organs has to be considered in the simulations to increase the accuracy of the predictions for the directional sensitivity of the organs.

Note that in the FE model (Fig. 5.9b) slit1 is compressed by approximately 4.8 nm when the plates with transversely isotropic material behavior are loaded by a rotation of 0.018° along the edges in x -direction (Fig. 5.9b). The slit face deformation for slit1 in lyriform organ HS8 of *C. salei* determined at the physiological threshold stimulus amplitude Höbl et al. (2007a) of ≈ 1.7 nm corresponds to a rotational displacement of 0.006° only, which illustrates the high sensitivity of the organ.

Chapter 6

Designing strain sensors based on arachnid slit sensilla

From an engineering point of view some of the possible design goals of strain sensors are:

- Sensitivity to uni-axial and/or multi-axial loads,
- resolution of the strain tensor and of the values and directions of the principal normal strains and their change (proprioceptor),
- measuring of the directions of uni-axial loads and of their changes,
- frequency sensitivity in the case of periodic stimuli, and
- maximizing the signal-to-noise ratio.

Most commonly strains in objects have been measured by strain gauges. Isolated strain gauges are used to measure the value of a direct strain component and rosette arrangements are employed to measure the strain tensor and the direction of the principal normal strains. Invented by Edward E. Simmons in 1938, the most common type of strain gauge consists of an insulating flexible backing which supports a metallic foil pattern. The gauge is attached to the object by a suitable adhesive and as the object is deformed, the foil is deformed, causing its electrical resistance to change. This change is easily measured and related to

the strain. Strain gauges may be damaged because of shock (overloading), heavy surges in current, chemical or moisture ingress, mis-handling, vibration, or internal component malfunctioning. In contrast to strain gauges sensors designed in analogy to lyriform organs have several advantages:

- A single sensor can be tailored in terms of directional sensitivity and redundancy of the measured load level, where in contrast, several strain gauges would be necessary,
- sensors can be downsized to a few microns (the size of the smallest “classical” strain gauges is in the range of mm), and
- the handling of changes in temperature is less critical than in strain gauges.

However, when sensors based on lyriform organs, i.e. consisting of arrangements of slits, are integrated into objects they decrease the local stiffness (in contrast to strain gauges which increase the stiffness) and tend to cause stress concentrations, which may be strength relevant. This has to be taken into account in the design of the structures¹⁾. In arachnid slit sensilla there tends to be some thickening of the cuticle in the vicinity of the organs and some increase of the volume fraction of the fibers, which may be responses to this problem. Such difficulties do not occur when the slits are integrated into bridge-like structures that are attached to the location where the deformations have to be measured (such bridges, however, increase the local stiffness and make the sensor more directional). In addition, sensors with open slits may be subject to contamination by small particles or dirt.

To our knowledge only one attempt of manufacturing biomimetic strain sensors has been reported in the literature (Wicaksono et al., 2005), taking the morphology of campaniform sensilla of insects as a starting point. There the authors fabricated combinations of blind-hole and membrane structural features as membrane-in-recess microstructures from Si-based materials and characterized their strain-sensing properties by optical measurements using interference patterns. They report that the blind-hole structure concentrates the strain on its edge and the membrane further amplifies the strains which can be used for developing a new type of sensor.

¹⁾ Because the sensitivity of a slit and the strength of the stress concentrations at its tips are intimately connected (compare Chapter 4.2.3.5), trade-offs between strength and sensitivity may have to be made, where e.g. increasing the thickness of the substrate decreases the sensitivity of the sensor.

In man-made sensors a number of ways for transducing the stimulus into an electrical signal appear feasible in principle, among them

- Ionic liquid-swollen Nafion (Teflon-based polymer) membranes (Bennett and Leo, 2003) covering the slits that generate electrical charge (ion exchange) between the electrodes attached to their surfaces in response to mechanical strain,
- measurement of the slit face deformations by Microelectromechanical devices that change their capacity when the slit faces are compressed or dilated, or
- optical measurement of the deformations of the slit faces or of a membrane covering the slit.

Note that the slits may actually be filled by a solid material that is considerably softer than the substrate. With decreasing stiffness contrast between substrate and filler the slit face displacements, but also the stress concentrations in the arrangement, decrease. If a particulate or fluid filling is used, obviously membranes are required for covering the slits. Membranes may also be employed in signal transduction (as is the case in arachnids) or as protection against contamination. Such membranes, however, have to be markedly more compliant than the substrate, so that their stiffness does not dominate the deformation of the slits, and they require a high fatigue life (high number of load cycles like the natural case). As is typical for Microelectromechanical Systems (MEMS) small sensors of complex shape like those based on the slit sensilla may be manufactured by modified semiconductor fabrication technology.

In the models described in the preceding sections the displacements are due to uni-axial loads acting in different directions Φ . In contrast, for sensor applications the inverse problem of determining the load direction and level from the slit deformations has to be solved.

For the design of the sensors some principles can be derived according to our findings described in the Chapters 4.1.1, 4.1.2, 4.1.3, and 5.1. The governing parameter for adjusting the slit deformation for a given load level is the length of the slits. The slits' aspect ratios can be changed within a wide range (20 to 100) without markedly influencing the slit deformation. When a single slit is to respond to a load in a given direction its orientation

should be adjusted so that its axis is oriented normal to the load direction rather than using slits of S-shaped centerlines as shown in Chapter 4.1.2.1. In arrangements of parallel slits the slit deformations are most sensitive to a change in the parameters lateral distance (shielding effects) and longitudinal shift (amplification effects) between the slits. In principle, the following slit patterns can be used in dependence on the design goals. (i) Oblique bar arrangements with slits of equal length that are laterally shifted and are sensitive to the same amplitude and directional range of loads and with the potential to increase the signal to noise ratio by convergence of the signals of the individual slits; (ii) triangular patterns with slits of different length with the potential of considerably increasing the amplitude range of a single slit; (iii) heart shaped or fan-like configurations with the potential of sensing the load direction on the basis of varying patterns of the slits active in the array (Barth et al., 1984).

For sensing in-plane strains planar substrates for the sensors are an obvious choice. When bending moments have to be resolved slits positioned on ridges are suggested and in situations of limited space dimples are recommended for increasing the distance between the slits and the neutral axis of the structure (=reference plane in shell-like structures). Provided the sensors are used in the linear elastic regime of the substrate the stress concentration factor at the ends of the slits will remain essentially the same for a wide range of substrates.

Chapter 7

Conclusions

We employed an analytical approach, Kachanov's method, and the Finite Element (FE) method to study some biomechanical aspects of lyriform organs of arachnids. The main goal of the present study lies in elucidating the principal biomechanical features of these organs. In addition, the results may serve as the quantitative basis for designing bio-inspired micro sensors. In planar models the results are presented relative to the deformation of a reference configuration, i.e. a single isolated crack or slit, and can be scaled to any crack or slit size and load amplitude as long as linear behavior can be assumed. The three-dimensional models, on the one hand, describe details of the actual slit geometries and, on the other hand, study the effects of the slits' position in generic spatially curved cuticular regions. There the results are presented in terms of absolute values.

Studies of single isolated slits incorporated into planar FE models show that their face deformations are mainly influenced by their length and their orientation relative to the direction of uni-directional loads, but are insensitive to aspect ratios (slit length/slit width) ranging between 20 and 100. On the basis of similar aspect ratios ellipse-like openings as found in strain sensitive campaniform sensilla in the cuticle of insects produce higher stress concentrations at their ends than capped rectangular slits.

Kachanov's approximations applied to crack-like slits show that interaction effects between the slits, namely shielding and amplification of the slit face deformations, are most prominent in a stack of similar slits which is chosen to assess the accuracy of this approach by the

FE method. Although limited to lateral spacings between the slits of $S/l_0 \geq 0.5$ Kachanov's method shows that interaction effects vanish for $S/l_0 \geq 3$ and strongly increase when the neighbor distances decrease. Accordingly, interactions between loose groups and lyriform organs and between neighboring lyriform organs can be expected when their neighboring distance is less than three times the length of the longest slit in the arrangement. For spacings found in lyriform organs ($S/l_0 \approx 0.02$) FE models of generic planar arrangements of parallel slits, i.e. stack, oblique bar, triangular, and fan-like configurations, show that amplification and shielding effects are strongly influenced by the closest neighbor distance between the slits. Accordingly, skewed triangular lyriform organs are typically found in arachnids in which the shorter slits are longitudinally shifted out of the "shadow" of the longest slit in the organ.

Further studies center on planar FE models of slits based on lyriform organs of the spiders *Cupiennius salei* and the bird spider *Aphonopelma*. For the triangular slit sensillum HS8 on the posterior side of the tibia of *C. salei* comparisons with measurements performed with white light interferometry show good agreement with the simulated slit face displacements. The directional sensitivity of a single isolated slit can be related to a figure-eight shape when the slit face deformation is plotted against load angle in a polar plot. Similar responses are reported for the directional sensitivity of arthropod mechanoreceptive hairs (Dechant et al., 2006). Depending on the geometry of the arrangement different sensitivities of the individual slits with regard to loads acting in different directions can be achieved, which can be used to extract the direction of loads. Arrangements with cascades of widely differing mechanical responses of the individual slits increase the range of load levels that can be detected compared to a single isolated slit. When the responses of the realistic slit arrangements are compared to those of generic arrangements of five slits it is found that lyriform organs are often combinations of the generic formations. We show that even small geometrical variations in the slit arrangement can have a major impact on the interaction effects and, as a consequence, also on the slit deformation. Furthermore, the stress concentrations in the vicinity of the slit arrangements are influenced by the interaction effects between the slits in the arrangements. The locations of the dendrites are investigated and it is found that in the models they are not necessarily positioned at the exact locations of the maximum slit face displacement at a given load angle, but close to it. Provided the transfer functions describing the transduction process are known, the

above results allow the prediction of the sensory output generated by planar arrangements of slits in the small strain regime.

Finally investigations on three-dimensional details of the slits' morphology, i.e. stiffnesses and shapes of the membranes and the fluid filling of the slit, and the embedding of the organs, i.e. sensilla located on elevations in the cuticle, are presented. Unexpected local effects are observed in a stack of five parallel slits with aspect ratio (slit length/slit width) of 100 at $S/l_0 = 0.02$, where the inner slits open up under compressive uni-axial loads, which is the consequence of the bending of the material between the slits. It is shown that the stiffness of the membranes influences the bending of the cuticular ligaments as the aspect ratio of the material between the slits and the amount of the Young's modulus of the membranes increases. When the curvature of the membrane is increased the deformation of the coupling cylinder compressing the dendrite is decreased, which indicates that the deformations at the locations of the dendrites may be reduced to protect the sensory terminals from mechanical damage by overstimulation in analogy to a mechanism observed in spider tactile hairs (Barth et al., 2004). In three-dimensional shell models of the shell-like cuticle that use a transversely isotropic material behavior single slits show the largest face deformations when they are located in meridional orientation on a stiffening ring of an ovalizing cylinder or when they are positioned in flat planar regions under in-plane loading. Detailed three-dimensional FE analyses show – as was also found by interferometric measurements (Schaber and Barth, in prep.) – that the outer membrane bulges towards the inside under compressive loading when the fluid filling of the slit can move across the inner membrane or when this filling is highly compressible.

Promising fields for future studies are refined models of details of the slits' morphology and of realistically shaped cuticular regions containing slit sensilla. Investigations of details of slit morphology may, for example, study the effects of variations of the thickness of the cuticle, of local values of the volume fraction of chitin fibers, and of the orientation of the lamellae (Fig. 2.8) in the vicinity of the slits. Studies of larger cuticular regions with embedded slit sensilla may, for example, target simplified shell models of leg segments. Provided suitable material data can be obtained modeling the nonlinear behavior of slit sensilla also is of considerable interest.

Appendix A

Expressions for calculating the stress field generated by a crack

Plane stress solutions for the normalized, dimensionless, plane stress fields generated by uniform tractions acting on an isolated crack in an infinite 2D medium can be obtained by the complex variable method (Willmore, 1949; Muskhelishvili, 1975; Kachanov, 1994).

The crack is defined to occupy the interval $[-l/2, l/2]$ of the x -axis (see Fig. 3.1).

Components of the stress tensor under normal loading p in y -direction

$$\begin{aligned}\sigma_{xx}/p &= I_2 - 8y^2I_4 + 8y^4I_6 \\ \sigma_{xy}/p &= 2(-yI_3 + xyI_4 + 4y^3I_5 - 4xy^3I_6) \\ \sigma_{yy}/p &= I_2 + 4y^2I_4 - 8y^4I_6\end{aligned}\tag{A.1}$$

Components of the stress tensor under in-plane shear loading τ

$$\begin{aligned}\sigma_{xx}/\tau &= 2(3yI_3 - 3xyI_4 - 4y^3I_5 + 4xy^3I_6) \\ \sigma_{xy}/\tau &= I_2 - 8y^2I_4 + 8y^4I_6 \\ \sigma_{yy}/\tau &= 2(-yI_3 + xyI_4 + 4y^3I_5 - 4xy^3I_6)\end{aligned}\tag{A.2}$$

where the following definitions are used

$$\begin{aligned}
I_1 &= \frac{l^3}{2} \frac{\sqrt{\varrho} - \sqrt{\eta}}{\sqrt{\delta}(\sqrt{\eta} + \sqrt{\varrho} + \sqrt{\delta})^2} \\
I_2 &= l^2 \frac{1}{\sqrt{\delta}(\sqrt{\eta} + \sqrt{\varrho} + \sqrt{\delta})} \\
I_3 &= \frac{l^3}{4} \frac{\sqrt{\varrho} - \sqrt{\eta}}{(\eta\varrho)^{1/2} \delta^{3/2}} \\
I_4 &= \frac{l^2}{2} \frac{\sqrt{\varrho} + \sqrt{\eta}}{(\eta\varrho)^{1/2} \delta^{3/2}} \\
I_5 &= \frac{l^3}{16} \frac{3\sqrt{\eta\varrho}(\sqrt{\eta} + \sqrt{\varrho})^2 (\sqrt{\varrho} - \sqrt{\eta}) + \delta(\varrho^{3/2} - \eta^{3/2})}{(\eta\varrho)^{3/2} \delta^{5/2}} \\
I_6 &= \frac{l^2}{8} \frac{3\sqrt{\eta\varrho}(\sqrt{\eta} + \sqrt{\varrho})^3 + \delta(\varrho^{3/2} + \eta^{3/2})}{(\eta\varrho)^{3/2} \delta^{5/2}} \\
\\
\eta &= (x - l/2)^2 + y^2 \\
\kappa &= 2(x^2 + y^2 - l^2/4) \\
\varrho &= (x + l/2)^2 + y^2 \\
\delta &= \kappa + 2\sqrt{\eta\varrho}
\end{aligned}$$

and p , τ are the applied far field normal and shear stress, respectively.

Appendix B

Example for adapting the normalized results of the planar models

Within the linear regime of the material and assuming small deformations the face displacements at any point along a given slit, $D_{\text{slit}}^*(x)$, can be evaluated as a function of the slit length l_0 and the far-field strain ε_a as

$$D_{\text{slit}}^*(x) = \frac{D(x)}{D_{\text{sc}}} \cdot \frac{D_{\text{sc}}}{l_0} \cdot l_0 \cdot \frac{\varepsilon_a}{\varepsilon_{a,r}} \quad (\text{B.1})$$

The value for $D(x)/D_{\text{sc}}$ depends on the geometrical configuration and is obtained from one of the diagrams in Figs. 4.6, 4.9, 4.11, 4.12, 4.13, and 4.14 for the required aspect ratio l_0/w_0 . The “reference values” for the single slit under normal loading, D_{sc}/l_0 and $\varepsilon_{a,r}$, are taken from Table B.1. In case the far-field stress σ_a is given rather than the far-field strain, the relationship

$$D_{\text{slit}}^*(x) = \frac{D(x)}{D_{\text{sc}}} \cdot \frac{D_{\text{sc}}}{l_0} \cdot l_0 \cdot \frac{E_r}{E} \cdot \frac{\sigma_a}{\sigma_{a,r}} \quad (\text{B.2})$$

must be used, in which the quotient E_r/E accounts for the effects of the Young’s modulus.

For evaluating $D_{\text{crack}}^*(\xi)$ (ξ defined in analogy to Chapter 3.1.3) for cracks Eqs. B.1 and B.2

have to be rewritten; the reference values for a single isolated crack under normal loading are listed in Table B.2

$$D_{\text{crack}}^*(\xi) = \frac{D(\xi)}{D_{\text{cc}}} \cdot \frac{D_{\text{cc}}}{l_0} \cdot l_0 \cdot \frac{\varepsilon_{\text{a}}}{\varepsilon_{\text{a,r}}} \quad (\text{B.3})$$

$$D_{\text{crack}}^*(\xi) = \frac{D(\xi)}{D_{\text{cc}}} \cdot \frac{D_{\text{cc}}}{l_0} \cdot l_0 \cdot \frac{E_{\text{r}}}{E} \cdot \frac{\sigma_{\text{a}}}{\sigma_{\text{a,r}}} \quad (\text{B.4})$$

The opening displacements scale linearly with the crack/slit length in Eqs. B.1 to B.4.

For example at the mid-length position ($D^*(\xi = 1/2 l_0) = D_{\text{c}}$) of the central slit (slit3) in the oblique bar formation (Fig. 4.9f) in a disc with Young's modulus $E = 17$ GPa, with a length of $l_0 = 100 \mu\text{m}$, a width of $w_0 = 1 \mu\text{m}$, a lateral spacing of $S/l_0 = 0.04$, and a longitudinal shift of $\lambda/l_0 = 0.85$, which is loaded by a compressive far-field stress of $\sigma = -500$ kPa, this procedure gives

$$D_{\text{c}} = 4.2 \cdot 5.034 \times 10^{-5} \cdot 100 \times 10^{-6} \cdot \frac{18 \times 10^9}{17 \times 10^9} \cdot \frac{-500 \times 10^3}{-0.45 \times 10^6} \text{ m} = 24.9 \text{ nm}$$

where $D(x)/D_{\text{sc}} = D_{\text{c}}/D_{\text{sc}} \approx 4.2$ is taken from Fig. 4.9b.

TABLE B.1: Reference values for a single slit of aspect ratio $l_0/w_0 = 100$ subjected to a uni-axial normal compressive strain.

$\varepsilon_{\text{a,r}}$	$\sigma_{\text{a,r}}$	E_{r}	D_{sc}/l_0
-2.5×10^{-5}	-0.45 MPa	18 GPa	5.034×10^{-5}

TABLE B.2: Reference values for a single crack subjected to a uni-axial tensile traction.

$\varepsilon_{\text{a,r}}$	$\sigma_{\text{a,r}}$	E_{r}	D_{cc}/l_0
5.56×10^{-5}	1 MPa	18 GPa	11.21×10^{-5}

Bibliography

- Adam, H. and Czihak, G. (1964). *Großes Zoologisches Praktikum, Teil I Arbeitsmethoden*. Stuttgart.
- Alexander, R. M. (1966). Rubber-like properties of the inner hinge-ligament of Pectinidae. *J. Exp. Biol.* **44**, pp. 119–130.
- Atluri, S. N., Kobayashi, A. S. and Nakagaki, M. (1974). An assumed displacement hybrid finite element model for linear fracture mechanics. *Int. J. Fract.* **11**, pp. 257–271.
- Barbakadze, N., Enders, S., Gorb, S. and Arzt, E. (2006). Local mechanical properties of the head articulation cuticle in the beetle *Pachnoda marginata* (Coleoptera, Scarabaeidae). *J. Exp. Biol.* **209**, pp. 722–730.
- Barsoum, R. S. (1977). Triangular quarter-point elements as elastic and perfectly-plastic crack tip elements. *Int. J. Num. Meth. Eng.* **11**(1), pp. 85–98.
- Barth, F. G. (1969). Die Feinstruktur des Spinneninteguments. I. Die Cuticula des Laufbeins adulter häutungsferner Tiere (*Cupiennius salei* Keys.). *Z. Zellforsch.* **97**(1), pp. 137–159.
- Barth, F. G. (1970). Die Feinstruktur des Spinneninteguments. II. Die räumliche Anordnung der Mikrofasern in der lamellierten Cuticula und ihre Beziehung zur Gestalt der Porenkanäle (*Cupiennius salei* Keys., adult, häutungsfern, Tarsus). *Z. Zellforsch.* **104**(1), pp. 87–106.
- Barth, F. G. (1971). Der sensorische Apparat der Spaltsinnesorgane (*Cupiennius salei* Keys. Araneae). *Z. Zellforsch.* **112**, pp. 212–246.

- Barth, F. G. (1972a). Die Physiologie der Spaltsinnesorgane – I. Modellversuche zur Rolle des cuticularen Spaltes beim Reiztransport. *J. Comp. Physiol.* **78**, pp. 315–336.
- Barth, F. G. (1972b). Die Physiologie der Spaltsinnesorgane – II. Funktionelle Morphologie eines Mechanoreceptors. *J. Comp. Physiol.* **81**, pp. 159–186.
- Barth, F. G. (1973). Microfiber reinforcement of an arthropod cuticle; laminated composite material in biology. *Z Zellforsch* **144**(3), pp. 403–433.
- Barth, F. G. (1981). Strain detection in the arthropod exoskeleton – Chapter 8. In: M. S. Laverack and D. J. Cosens (eds.), *Sense Organs*, pp. 112–141. Blackie, Glasgow.
- Barth, F. G. (2002a). *A Spider's World: Senses and Behavior*. Springer-Verlag, Berlin Heidelberg New York.
- Barth, F. G. and Bohnenberger, J. (1978). Lyriform slit sense organ: Thresholds and stimulus amplitude ranges in a multi-unit mechanoreceptor. *J. Comp. Physiol.* **125**, pp. 37–43.
- Barth, F. G., Ficker, E. and Federle, H.-U. (1984). Model studies on the mechanical significance of grouping in compound spider slit sensilla. *Zoomorphology* **104**, pp. 204–215.
- Barth, F. G. and Höller, A. (1999). Dynamics of arthropod filiform hairs. V. The response of spider trichobothria to natural stimuli. *Phil. Trans. R. Soc. Lond. B* **354**, pp. 183–192.
- Barth, F. G. and Libera, W. (1970). Ein Atlas der Spaltsinnesorgane von *Cupiennius salei* Keys., Chelizerata (Araneae). *Z. Morph. Tiere* **68**, pp. 343–369.
- Barth, F. G., Nemeth, S. S. and Friedrich, O. C. (2004). Arthropod touch reception: structure and mechanics of the basal part of a spider tactile hair. *J. Comp. Physiol. A* **190**, pp. 523–530.
- Barth, F. G. and Stagl, J. (1976). The slit sense organs of arachnids; a comparative study of their topography on the walking legs (chelicerata, arachnida). *Zoomorphology* **86**, pp. 1–23.
- Barth, F. G. and Wadepuhl, M. (1975). Slit sense organs on the scorpion leg (*Androctonus australis* l., *Buthidae*). *J. Morph.* **145**(2), pp. 209–228.

- Bennett, M. D. and Leo, D. J. (2003). Manufacture and characterization of ionic polymer transducers employing non-precious metal electrodes. *Smart Mat. Struct.* **12**, pp. 424–436.
- Benveniste, Y., Dvorak, G. J. and Wung, E. C. J. (1989). On interacting cracks and complex crack configurations in linear elastic media. *Int. J. Solids Struct.* **25**(11), pp. 1279–1293.
- Benzley, S. F. (1974). Representation of singularities with isoparametric finite elements. *Int. J. Num. Meth. Eng.* **8**(3), pp. 537–545.
- Blickhan, R. (1983). *Dehnungen im Außenskelett von Spinnen*. Ph.D. thesis, University of Frankfurt.
- Blickhan, R. (1986). Stiffness of an arthropod leg joint. *J. Biomechanics* **19**(5), pp. 375–384.
- Blickhan, R. and Barth, F. G. (1985). Strains in the exoskeleton of spiders. *J. Comp. Physiol. A* **157**, pp. 115–147.
- Böhm, H. J. (2004). A short introduction to basic aspects of continuum micromechanics. In: H. J. Böhm (ed.), *Mechanics of Microstructured Materials*, pp. 1–40. Springer, Wien-New York.
- Bruet, B. J. F., Qi, H. J., Boyce, M. C., Panas, R., Tai, L., Frick, L. and Ortiz, C. (2005). Nanoscale morphology and indentation of individual nacre tablets from the gastropod mollusc *Trochus niloticus*. *J. Mater. Res.* **20**(9), pp. 2400–2419.
- Brüssel, A. (1987). *Belastungen und Dehnungen im Spinnenskelett unter natürlichen Verhaltensbedingungen*. Ph.D. thesis, University of Frankfurt.
- Byskov, E. (1970). The calculation of stress intensity factors using the finite element method with cracked elements. *Int. J. Fracture* **6**, pp. 159–167.
- Chapman, R. F. (1999). *The Insects: Structure and Function*. Cambridge University Press, Cambridge.
- Chen, B. and Fan, J. (2004). Microstructures of chafer cuticle and biomimetic design. *J. Comput. Aided Mater. Des.* **11**, pp. 201–210.

- Chen, B., Peng, X., Wang, W., Zhang, J. and Zhang, R. (2002). Research on the microstructure of insect cuticle and the strength of a biomimetic preformed hole composite. *Micron* **33**, pp. 571–574.
- Cocatre-Zilgen, J. H. and Delcomyn, F. (1999). Modeling stress and strain in an insect leg for simulation of campaniform sensilla responses to external forces. *Biol. Cybern.* **81**, pp. 149–160.
- Combes, S. A. and Daniel, T. L. (2003). Flexural stiffness in insect wings II. Spatial distribution and dynamic wing bending. *J. Exp. Biol.* **206**, pp. 2989–2997.
- Currey, J. D. (1970). *Animal Skeletons*. Hodder Arnold H&S.
- Currey, J. D., Nash, A. and Bonfield, W. (1982). Calcified cuticle in the stomatopod smashing limb. *J. Mat. Sci.* **17**(7), pp. 1939–1944.
- Dechant, H. E., Höbl, B., Rammerstorfer, F. G. and Barth, F. G. (2006). Arthropod mechanoreceptive hairs: modeling the directionality of the joint. *J. Comp. Physiol. A* **192**, pp. 1271–1278.
- Dechant, H. E., Rammerstorfer, F. G. and Barth, F. G. (2001). Arthropod touch reception: Stimulus transformation and finite element model of spider tactile hairs. *J. Comp. Physiol. A* **187**, pp. 313–322; see also erratum p. 851.
- Filshie, B. K. (1982). Fine structure of the cuticle of insects and other arthropods. In: R. C. King and H. Akai (eds.), *Insect Ultrastructure*, pp. 281–312. Plenum Press, New York and London.
- Flannigan, W. C. (1998). *Finite Element Modeling of Arthropod Exoskeleton*. Master's thesis, Case Western Reserve University.
- French, A. S., Torkkeli, P. H. and Seyfarth, E.-A. (2002). From stress and strain to spikes: mechanotransduction in spider slit sensilla. *J. Comp. Physiol. A* **188**, pp. 739–752.
- Gindl, W. and Gupta, H. S. (2002). Cell-wall hardness and Young's modulus of melamine-modified spruce wood by nano-indentation. *Composites: Part A* **33**, pp. 1141–1145.
- Gingl, E., Burger, A.-M. and Barth, F. G. (2006). Intracellular recording from a spider vibration receptor. *J. Comp. Physiol. A* **192**, pp. 551–558.

- Gnatzy, W. and Tautz, J. (1980). Ultrastructure and mechanical properties of an insect mechanoreceptor: Stimulus transmitting structures and sensory apparatus of the cercal filiform hairs of *Gryllus*. *Cell Tissue Res.* **213**, pp. 441–463.
- Gorbatikh, L. and Kachanov, M. (2000). A simple technique for constructing the full stress and displacement fields in elastic plates with multiple cracks. *Eng. Fract. Mech.* **66**, pp. 51–63.
- Gosline, J. M. (1980). The elastic properties of rubbery-like proteins and highly extensible tissue. In: J. F. V. Vincent and J. D. Currey (eds.), *The Mechanical Properties of Biological Materials*, pp. 331–358. Cambridge University Press, Cambridge.
- Gross, D. (1982). Spannungsintensitätsfaktoren von Rißsystemen. *Ing.-Archiv* **51**, pp. 301–310.
- Hahn, H. G. (1976). *Bruchmechanik*. Teubner, Stuttgart.
- Hengsberger, S., Enstroem, J., Peyrin, F. and Zysset, P. (2003). How is the indentation modulus of bone tissue related to its macroscopic elastic response? A validation study. *J. Biomech.* **36**, pp. 1503–1509.
- Henshell, R. D. and Shaw, K. G. (1975). Crack tip finite elements are unnecessary. *Int. J. Num. Meth. Eng.* **9**(3), pp. 495–507.
- Hepburn, H. R. (1975). Mechanical properties of a crab shell. *Comp. Biochem. Physiol.* **50A**, pp. 551–554.
- Hepburn, H. R. (1976). *Insect Integument*. Elsevier, Amsterdam.
- Hepburn, H. R. and Ball, A. (1973). On the structure and mechanical properties of beetle shells. *J. Mater. Sci.* **8**, pp. 618–623.
- Hepburn, H. R. and Levy, H. (1975). Mechanical properties of some larval cuticles. *J. ent. Soc. sth. Afr.* **38**, pp. 131–140.
- Hepburn, H. R. and Roberts, D. C. (1975). Stiffness and tanning of sclerites. *J. Insect Physiol.* **21**, pp. 1741–1746.

- Herzog, R. O. (1926). Fortschritte in der Erkenntnis der Faserstoffe. *Z. angew. Chem.* pp. 297–302.
- Hillerton, J. E. (1979). Changes in the mechanical properties of the extensible cuticle of *rhodnius* through the fifth larval instar. *J. Insect Physiol.* **25**(1), pp. 73–77.
- Hillerton, J. E. (1980). Electron microscopy of fibril-matrix interactions in a natural composite insect cuticle. *J. Mat. Sci.* **15**, pp. 3109–3112.
- Hillerton, J. E. and Purslow, P. P. (1981). An investigation of some matrix protein components critical to the extensible properties of insect cuticle. *J. Mat. Sci.* **16**, pp. 1673–1679.
- Hillerton, J. E., Reynolds, S. E. and Vincent, J. F. V. (1982). On the indentation hardness of insect cuticle. *J. Exp. Biol.* **96**, pp. 45–52.
- Horii, H. and Nemat-Nasser, S. (2000). Elastic fields of interacting inhomogeneities. *Int. J. Solids Struct.* **66**, pp. 731–745.
- Höbl, B., Böhm, H. J., Rammerstorfer, F. G. and Barth, F. G. (2005). Mechanoreception in the exoskeleton of arachnids: engineering meets biology. In: *Proc 3rd IASTED Conf Biomech*, pp. 44–48. Benidorm.
- Höbl, B., Böhm, H. J., Rammerstorfer, F. G. and Barth, F. G. (2007a). Finite element modeling of arachnid slit sensilla — I. The mechanical significance of different slit arrays. *J. Comp. Physiol. A* **193**, pp. 445–459.
- Höbl, B., Böhm, H. J., Rammerstorfer, F. G. and Barth, F. G. (2007c). Finite element modeling of arachnid slit sensilla — III. 3D morphology and embedding. *in prep* .
- Höbl, B., Böhm, H. J., Rammerstorfer, F. G., Müllan, R. and Barth, F. G. (2006). Studying the deformation of arachnid slit sensilla with a fracture mechanical approach. *J. Biomech.* **39**, pp. 1761–1768.
- Höbl, B., Böhm, H. J., Schaber, C., Rammerstorfer, F. G. and Barth, F. G. (2007b). Finite element modeling of arachnid slit sensilla — II. Deformation of slit arrays imitating actual lyriform organs. *in prep* .
- Huang, J. H. (2001). Some closed-form solutions for effective moduli of composites containing randomly orientated short fibers. *Mater. Sci. Engng. A* **315**, pp. 11–20.

- Humphrey, J. A. C., Barth, F. G., Reed, M. and Spak, A. (2003). The physics of arthropod medium-flow sensitive hairs: Biological models for artificial sensors. In: F. G. Barth, J. A. C. Humphrey and T. W. Secomb (eds.), *Sensors and sensing in biology and engineering*, pp. 129–144. Springer, Wien.
- Jensen, M. and Weis-Fogh, T. (1962). Biology and physics of locust flight – V. Strength and elasticity of locust cuticle. *Phil. Trans. R. Soc. B.* **245**, pp. 137–169.
- Joffe, I. and Hepburn, H. R. (1973). Observations on regenerated chitin films. *J. Mat. Sci.* **8**, pp. 1751–1754.
- Joffe, I., Hepburn, H. R. and Andersen, S. O. (1975). On the mechanical properties of *Limulus* solid cuticle. *J. Comp. Physiol.* **101**, pp. 147–160.
- Jones, R. M. (1999). *Mechanics of Composite Materials*. Taylor & Francis Inc., Philadelphia, PA, USA.
- Kachanov, M. (1987). Elastic solids with many cracks: A simple method of analysis. *Int. J. Solids Struct.* **23**, pp. 23–45.
- Kachanov, M. (1994). Elastic solids with many cracks and related problems. In: J. Hutchinson and T. Wu (eds.), *Advances in Applied Mechanics, Volume 30*, pp. 259–426. Academic Press, San Diego, CA, USA.
- Kaliyamoorthy, S., Quinn, R. and Zill, S. (2005). Force sensors in hexapod locomotion. *The Int. J. Rob. Res.* **24**, pp. 563–574.
- Kaliyamoorthy, S., Zill, S., Quinn, R., Ritzmann, R. and Jongung, C. (2001). Finite element analysis of strains in a *blaberus* cockroach leg during climbing. In: *Proc. 2001 IEEE/RSJ Int. Conf. on Intell. Robots and Systems*, pp. 833–838. Maui, Hawaii.
- Katz, S. L. and Gosline, J. M. (1994). Scaling modulus as a degree of freedom in the design of locust legs. *J. Exp. Biol.* **187**, pp. 207–223.
- Ker, R. F. (1977). *Some Structural and Mechanical Properties of Locust and Beetle Cuticle*. Ph.D. thesis, University of Oxford.
- Kesel, A. B., Philippi, U. and Nachtigall, W. (1998). Biomechanical aspects of the insect wing: an analysis using the finite element method. *Comput. Biol. Med.* **28**, pp. 423–437.

- Kohane, M., Daugela, A., Kutomi, H., Charlson, L., Wyrobek, A. and Wyrobek, J. (2002). Nanoscale *in vivo* evaluation of the stiffness of *Drosophila melanogaster* integument during development. *J. of Biomed. Mater. Research* **66**(3), pp. 633–642.
- Kreuz, P., Kempf, M., Kesel, A. B., Göken, M., Vehoff, H. and Nachtigall, W. (1998). Mechanical characteristics of biological materials - measurements on a dragonfly wing (Anisoptera). In: *Zoology 101: 40 (Supplement 1; DZG 91.1; Annual Meeting of the Deutsche Zoologische Gesellschaft, Leipzig)*.
- Krzelj, S. (1969). Structure anatomique comparée des élytres de Coléoptères. *Ann. Soc. roy. zool. Belg.* **99**, pp. 495–507.
- Lachmuth, U., Grasshoff, M. and Barth, F. G. (1985). Taxonomische Revision der Gattung *Cupiennius* SIMON 1891 (Arachnida: Araneae). *Senckenbergiana biologica* **65**, pp. 329–372.
- Li, Y. P., Tham, L. G., Wang, Y. H. and Tsui, Y. (2003). Modified Kachanov's method for analysis of solids with multiple cracks. *Eng. Fract. Mech.* **70**, pp. 1115–1129.
- Mori, T. and Tanaka, K. (1973). Average stress in matrix and average elastic energy of materials with misfitting inclusions. *Acta Met.* **21**, pp. 571–574.
- Müllan, R. (2005). *Feinbau und Rekonstruktion der Cuticulastrukturen lyraförmiger Sinnesorgane der Spinne Cupiennius salei*. Master's thesis, University of Vienna.
- Muskhelishvili, N. (1975). *Some Basic Problems of the Mathematical Theory of Elasticity*. Noordhoff International, Leyden, Netherlands.
- Neville, A. C. (1975). *Biology of the Arthropod Cuticle*. Springer-Verlag, Berlin Heidelberg New York.
- Neville, A. C. (1998). The significance of insect cuticle. In: F. W. Harrison and M. Locke (eds.), *Microscopic Anatomy of Invertebrates. 11A (Insecta)*, pp. 151–176. Wiley-Liss, New York.
- Neville, A. C., Parry, D. A. D. and Woodhead-Galloway, J. (1976). The chitin crystallite in arthropod cuticle. *J. Cell Sci.* **21**, pp. 73–82.

- Nishioka, T., Kato, T. and Itoh, N. (1997). Three-dimensional problems of strongly interacting arbitrarily located micro-elliptical cracks. In: I. Jordaan (ed.), *Inelasticity and Damage in Solids Subject to Microstructural Change*, pp. 256–426. Memorial University of Newfoundland, St. John's, Canada.
- Noah, J. A., Quimby, L., Frazier, S. and Zill, S. (2004). Sensing the effect of body load in legs: response of tibial campaniform sensilla to forces applied to the thorax in freely standing cockroaches. *J. Comp. Physiol. A* **190**, pp. 201–215.
- Papaioannou, S. G., Hilton, P. D. and Lucas, R. A. (1974). A finite element method for calculating stress intensity factors and its application to composites. *Eng. Fract. Mech.* **6**, pp. 807–823.
- Peterson, R. E. (1974). *Stress concentration factors*. John Wiley & Sons, New York, NY, USA.
- Rammerstorfer, F. G. (2003). *Grundlagen der Finite Elemente Methoden. Lecture Notes*. ILSB, Vienna University of Technology.
- Reynolds, S. E. (1975). The mechanics of plasticization of the abdominal cuticle in *Rhodinus*. *J. Exp. Biology* **62**, pp. 81–98.
- Rick, R., Barth, F. G. and Pawel, A. (1976). X-ray microanalysis of receptor lymph in a cuticular arthropod sensillum. *J Comp Physiol* **110**, pp. 89–95.
- Romeis, B. (1968). *Mikroskopische Technik*. Oldenburg, München-Wien.
- Schaber, C. and Barth, F. G. (in prep.). White light interferometric measurements of the deformations of a lyriform organ. *in preparation* .
- Skordos, A., Chan, C., Jeronimidis, G. and Vincent, J. F. V. (2002). A novel strain sensor based on the campaniform sensillum of insects. *Phil. Trans. R. Soc. Lond. A* **360**, pp. 239–254.
- Smith, C. W., Herbert, R., Wootton, R. J. and Evans, K. E. (2000). The hind wing of the desert locust (*Schistocerca gregaria* forskal): II. Mechanical properties and functioning of the membrane. *J. Exp. Biol.* **203**, pp. 2933–2943.

- Song, F., Lee, K. L., Soh, A. K., Zhu, F. and Bai, Y. L. (2004). Experimental studies of the material properties of the forewing of *cicada* (homoptera, cicadidae). *J. Exp. Biol.* **207**, pp. 3035–3042.
- Stevenson, J. R. (1985). Dynamics of the integument. In: D. E. Bliss and L. H. Mantel (eds.), *The Biology of Crustacea Vol. 9: Integument, Pigments, and Hormonal Processes*, pp. 2–43. Academic Press, New York.
- Thurm, U. (1982). Grundzüge der Transduktionsmechanismen in Sinneszellen. Mechano-elektrische Transduktion. In: W. Hoppe, W. Lohmann, H. Markl and H. Ziegler (eds.), *Biophysik*, pp. 681–696. Springer, Berlin.
- Tong, P., Pian, T. H. H. and Lasry, S. J. (1973). A hybrid-element approach to crack problems in plane elasticity. *Int. J. Num. Meth. Eng.* **7**, pp. 1031–1036.
- Tracey, D. M. (1971). Finite elements for determination of crack tip elastic stress intensity factors. *Eng. Fract. Mech.* **3**, pp. 255–265.
- Tychsen, P. H. and Vincent, J. F. V. (1976). Correlated changes in the mechanical properties of the intersegmental membrane and bonding between the proteins in the female adult locust. *J. Insect Physiol.* **22**, pp. 115–125.
- Vincent, J. F. V. (1980). Insect cuticle: a paradigm for natural composites. In: J. F. V. Vincent and J. D. Currey (eds.), *The Mechanical Properties of Biological Materials*, volume XXXIV, pp. 183–210. Soc. Exp. Biol. Symp.
- Vincent, J. F. V. (1982). *Structural Biomaterials*. The MacMillan Press Ltd., London.
- Vincent, J. F. V. (1998). The cuticle as an exoskeleton. In: W. H. Frederick and L. Michael (eds.), *Microscopic Anatomy of Invertebrates: Insecta: 11A*, pp. 139–149. John Wiley & Sons Inc.
- Vincent, J. F. V. (2002a). Arthropod cuticle: a natural composite shell system. *Composites Part A* **33**, pp. 1311–1315.
- Vincent, J. F. V. (2002b). Survival of the cheapest. *Materials Today* **12**, pp. 28–41.
- Vincent, J. F. V. and Hillerton, J. E. (1979). The tanning of insect cuticle - a critical review and a revised mechanism. *J. Insect Physiol.* **25**, pp. 653–658.

- Vincent, J. F. V. and Wegst, U. G. K. (2004). Design and mechanical properties of insect cuticle. *Arthropod Struct. Dev.* **33**, pp. 187–199.
- Vogel, S. (2003). *Comparative Biomechanics: Life's Physical World*. Princeton University Press, Princeton and Oxford.
- Wainwright, S. A., Biggs, W. D., Currey, J. D. and Gosline, J. M. (1982). *Mechanical Design in Organisms*. Princeton University Press, Princeton, New Jersey.
- Weis-Fogh, T. (1961). Molecular interpretation of the elasticity of resilin, a rubbery-like protein. *J. Mol. Biol.* **3**, pp. 648–667.
- Wicaksono, D. H. B., Pandraud, G., Vincent, J. F. V. and French, P. J. (2005). Early stages fabrication and optical characterisation of new micromachined silicon strain-sensing structures inspired from the campaniform sensillum of insects. *J. Micromech. Microeng.* **15**, pp. 72–81.
- Wigglesworth, V. B. (1988). The source of lipids and polyphenols for the insect cuticle. The role of the fat body, *oenocytes* and *oenocytoids*. *Tissue Cell* **20**, pp. 919–932.
- Willmore, T. J. (1949). The distribution of stress in the neighbourhood of a crack. *Quart. J. Mech. Appl. Math.* **2**(1), pp. 53–63.
- Zill, S. and Moran, D. T. (1981). The exoskeleton and insect proprioception. I. Responses of tibial campaniform sensilla to external and muscle-generated forces in the american cockroach, *Periplaneta americana*. *J. Exp. Biol.* **91**(1), pp. 1–24.

Curriculum Vitae

Name : Bernhard Hößl
Date of birth : October 31, 1975
Place of birth : Wiener Neustadt, Austria
Nationality : Austrian

Education

since Aug. 2003	Doctoral student at the Institute of Lightweight Design and Structural-Biomechanics, University of Technology, Vienna, Austria. Working title of thesis: “Mechanical simulation of slit sensors of arachnids”.
Oct. 01 – May 02	Compulsory military service.
Sept. 2001	Graduated with the degree of Diplomingenieur.
1995 – 2001	Studies of mechanical engineering at the University of Technology, Vienna, Austria. Diploma thesis: “Simulationen zur elektromechanischen Lenkung” at BMW AG, Munich, Germany.
1990 – 1995	Graduation at “Höhere Technische Bundeslehranstalt”, Eisenstadt, Austria.
1999	Exchange student at University of North Carolina at Charlotte, NC, USA.

Professional Development

Sept. 02 – June 03	Engineer at the department of vehicle dynamics at Audi AG, Ingolstadt, Germany.
--------------------	---